

23

Investigation of High Linearity DFB Lasers for Analog Communications

by

Ravindra Vinod Dalal

Submitted to the Department of Electrical Engineering and Computer Science and the Department of Physics in partial fulfillment of the requirements for the degrees of

Master of Engineering in Electrical Engineering and the Bachelors of Physics

at the

MASSACHUSETTS INSTITUTE OF TECHNOLOGY

February, 1998

© Massachusetts Institute of Technology, 1998. All Rights Reserved.

Author .. Department of Electrical Engineering and Computer Science
February 2, 1998

Certified by
Professor Rajeev J. Ram
Department of Electrical Engineering and Computer Science
Thesis Supervisor

Accepted by
Arthur C. Smith
Chairman, EECS Department Committee on Graduate Theses

Accepted by
June L. Matthews
Senior thesis coordinator, Department of Physics

MASSACHUSETTS INSTITUTE OF TECHNOLOGY

JUL 14 1998

Eng.

Investigation of High Linearity DFB Lasers for Analog Communications

by

Ravindra Vinod Dalal

Submitted to the Department of Physics and the
Department of Electrical Engineering and Computer Science
on February 2, 1998, in partial fulfillment of the requirements for
the degrees of Master of Engineering in Electrical Engineering and
Computer Science and the degree of Bachelors in Physics

Abstract

High-linearity, low-noise DFB lasers are necessary for analog optical communications, including subcarrier multiplexed systems, wireless personal communication systems (PCS) service and phased array radar. In this thesis, we examine the dynamic range and distortion for a Fujitsu DFB laser. We extract parameters from the device and use these parameters to simulate the distortion characteristics. We measure the spurious free dynamic range (SFDR) and find that it peaks at a certain current bias; we hypothesize that this maximum is related to a cancellation effect between the gain compression and the spatial hole burning nonlinearities in the laser. We also measure the SFDR versus frequency and find that the dynamic range is relatively insensitive to temperature changes between 300 and 700 MHz. Based on these findings, we make suggestions for ways to improve the laser performance and reduce the packaging cost.

Thesis Supervisor: Professor Rajeev Ram

Title: Assistant Professor of Electrical Engineering and Computer Science

Acknowledgements

First of all, I would like to thank my thesis advisor, Rajeev Ram. His endless patience, enthusiasm, curiosity, understanding, and willingness to teach have been incredibly inspiring and rewarding. I have learned a great deal about lasers and life from Rajeev, and in the process I have had a lot of fun.

From Lincoln Labs, I would like to thank Roger Helkey, Harold Rousell, Mike Taylor, and Mike Corcoran. They were all very helpful, and they were also a fun bunch to hang out with.

I gratefully acknowledge the support of DARPA through Lincoln Labs under the Advanced Photonics Program. I also gratefully acknowledge the support of Anacom corporation under the small business initiative for research (SBIR) program.

I would like to thank Richard Schatz of the Royal Institute of Technology in Stockholm, Sweden for use of the program LaserMatrix, which has been an invaluable tool in learning about lasers and in completing this thesis.

From the group, I would like to thank Jianyao Chen for his great help in explaining many aspects of DFB lasers to me, and also for helping me get my program to work properly. Thanks also to Farhan Rana, Joonah Yoon, Erwin Lau, Dieter Graef, and Steve Patterson for encouragement, help, and laughs.

I want to thank all of my friends, with whom I shared my happiest and saddest moments at MIT. It is their companionship that has made life so enjoyable. I especially want to thank Charu Puri, Malay Kundu, Ted Miguel, Suma Dutta, Pappudu Sriram, Doug Wyatt, Amit Goyal, Manish Goyal, Pratip Banerji, Surya Ganguli, Elaine Haberer, John

Rodriguez, Kofi Aidoo, and Rishi Shah, who were all extra supportive during the last few months.

And last, but most importantly, I would like to thank my parents for their love and support. Thanks to my father for all that he has taught me and the strong values he has instilled in me. Special thanks to my mother, who was always available to give constant love, encouragement and advice. I also want to thank my grandmother, *Motiba*, for all of her love she gave me while growing up. My love and gratitude to these three people cannot be expressed in words alone. Thank you.

TABLE OF CONTENTS

1	Introduction	19
1.1	What is a semiconductor laser?	21
1.2	Performance limitations	25
1.3	Previous work done in this field	27
1.4	Research presented in this thesis	28
1.5	Outline of this report	29
2	Laser distortion theory	31
2.1	Laser rate equation analysis in steady state	32
2.1.1	Phenomenological description	32
2.1.2	Lasing, loss, and gain	36
2.1.3	Light output	42
2.1.4	Temperature effects	44
2.2	Modulation response	46
2.3	Performance limitations	51
2.3.1	Distortion	52
2.3.2	Noise	56
2.3.3	Spurious Free Dynamic Range	58
2.4	Parameter extraction	62

2.5	Distortion simulation	67
2.6	Summary	72
3	Distributed feedback (DFB) lasers	73
3.1	Differences between Fabry-Perot and DFB lasers	74
3.2	DFB Theory	75
3.2.1	Coupled wave theory	75
3.2.2	Spatial hole burning in DFB lasers	80
3.2.3	Minimizing spatial hole burning effects in DFB lasers	85
3.2.4	Mode selection	87
3.2.5	Mode Spectrum.....	90
3.3	Fujitsu DFB Structure	92
3.4	Parameter extraction	93
3.4.1	Extraction procedure	94
3.4.2	Measurements for parameter extraction	96
3.5	Conclusion	98
4	High speed measurements	99
4.1	Equipment and setup	100
4.2	High speed measurement procedure	101
4.2.1	Procedure	101
4.2.2	Noise calibration	104
4.2.3	Equipment Calibration	105
4.2.4	Comparison of hand measurements with program measurements.	105

4.3	Experimental data	107
4.3.1	Dynamic range versus current bias	107
4.3.2	Dynamic range versus frequency	112
4.4	Discussion and summary	116
4.4.1	Spatial hole burning related cancellation effects	116
4.4.2	Spatial hole burning related mode selection	119
4.4.3	Temperature related effects	121
5	Conclusion	123
5.1	Summary of work	123
5.2	Maximizing Dynamic Range (SFDR)	126
5.3	Temperature insensitivity	128
5.4	Future work.....	128
	Appendix A: Procedure for high speed measurement	131
A.1	Calibration.....	131
A.2	Measurement routine	133
	References	135

LIST OF FIGURES

1.1	(a) Subcarrier multiplexed systems (SCM). Multiple channels are fed into a single laser which transmits a signal over fiber optic cable to a detector, which can select the desired channel. [27] (b) Personal communications system (PCS). A central station keeps a phone in constant contact with a transmitting station by switching between different “cells”, which are linked fiber optically to the central station.[34]	20
1.2	Generic DFB or Fabry-Perot laser structure.	22
1.3	Distortion products for broad-band and narrow-band applications. The dashed line shows that for narrow-band, performance will be limited by IMD3.	26
2.1	Analogy between steady state laser and water flow. Based on Coldren and Corzine.[9]	33
2.2	Four types of recombinations. (a) Stimulated emission, (b) Spontaneous emission, (c) Nonradiative recombination due to trap, and (d) Auger recombination.	34
2.3	Simulated LI curves with gain compression, for four values of ϵ . The case of $\epsilon=0$ and $\epsilon=3 \times 10^{-17}$ are indistinguishable for this current range.	38
2.4	(a) Photon density, (b) carrier density, (c) photon gain, (d) and refractive index in 300 mm Fabry-Perot laser at $I=5I_{th}$. Simulations performed using LaserMatrix (Royal Institute of Technology, Sweden). Simulations indicate the effect of spatial hole burning on the carrier density at the facets of the device, leading to a decrease	

	in the gain and an increase in the refractive index.	41
2.5	Closely spaced modes in a Fabry-Perot structure. The broad solid line is the gain curve, and the dashed line is the threshold gain curve. The mode that falls under the gain curve and has the lowest threshold gain will reach stimulated emission first. Other modes could also possibly begin to lase if they reach threshold.	44
2.6	Modulation response, (a) no gain compression. (b) with gain compression. ($\epsilon=3 \times 10^{-17}$).	50
2.7	Distortion products for broad-band and narrow-band applications. The dashed line shows that for narrow-band, performance will be limited by IMD3.	53
2.8	Definitions for Spurious free dynamic range (SFDR).	58
2.9	RIN vs frequency for Fujitsu laser. The peaks correspond to ω_R	64
2.10	Peak resonance and peak laser RIN vs bias current, for Fujitsu laser.	64
2.11	LI curve for Fujitsu laser, measured at different temperatures.	65
2.12	Threshold current versus temperature.	65
2.13	Third order intermodulation distortion (IMD3), for four different values of gain compression.	67
2.14	Distortion for (a) no gain compression, (b) $\epsilon=3 \times 10^{-17}$	70
2.15	(a) IMD3 relative to carrier vs. bias for two gain compression values. (b) IMD3 relative to carrier divided by the modulation depth cubed.	71
3.1	Modal threshold gain (αL) versus mode detuning (δL) for index coupled AR/AR coated DFB laser. From Kogelnik and Shank.[21]	79
3.2	The plot of wavelength vs $\text{Re}[\kappa L]$ shows the widening of the stop band as κL is in-	

creased. The modes near the stop band are also pushed away as κL increases. Simulation performed using LaserMatrix (Royal Institute of Technology, Sweden). 79

3.3 (a) Photon density, (b) carrier density, (c) photon gain, (d) and refractive index in an AR/AR coated DFB laser with a large coupling coefficient ($\kappa L=3.0$) at $I=5I_{th}$. Simulations performed using LaserMatrix (Royal Institute of Technology, Sweden). Simulations clearly indicate the effect of spatial hole burning on the carrier density, leading to a decrease in the gain and an increase in the refractive index. All of the distributions are symmetric due to the symmetry of the structure.83

3.4 (a) Photon density, (b) carrier density, (c) photon gain, (d) and refractive index in HR/AR coated DFB laser with $\kappa L=0.8$ at $I=5I_{th}$. Simulations performed using LaserMatrix (Royal Institute of Technology, Sweden). Simulations clearly indicate the effect of spatial hole burning on the carrier density, leading to a decrease in the gain and an increase in the refractive index. Due to the asymmetry of the facet coatings, the distributions are all shifted. If, however, the length were doubled while the κ remains constant, the distributions would again resemble those in Figure Figure 3.3:. The distributions in these figures roughly correspond to what is expected for the Fujitsu laser.84

3.5 Refractive index shape due to spatial hole burning in AR/AR DFB laser.88

3.6 Refractive index due to spatial hole burning in AR/HR coated DFB laser.88

3.7 Reflection spectrum of index coated AR/AR coated DFB laser. Plot shows power reflection spectrum of grating for four different κL values versus modal detuning, δL90

3.8 Multiple wavelength windows occur, but only one falls under the gain curve. Based on [24].81

3.9	Schematic of Fujitsu DFB laser. Drawing courtesy Jianyao Chen.	93
3.10	Width of bandstop versus length of device for different kL's for AR/HR coated DFB laser similar to Fujitsu laser. Plot is for conditions: facet reflectivities 80% / 1%, $n_g = 4.0$, $n_{eff} = 3.285$, $I = (0.8)I_{th}$. Simulations performed using LaserMatrix.	95
3.11	Experimental set up for measurement of optical spectra.	96
3.12	Optical spectrum for Fujitsu DFB laser, measured at three values: below threshold (10.0 mA), at threshold (13.2 mA), and above threshold (14.0 mA).	97
4.1	Test system block diagram.	100
4.2	Measurement block diagrams for the three noise calibration steps.	103
4.3	Comparison of program measurements (solid lines) and hand measurements (dashed lines).	106
4.4	SFDR and noise figure versus current, Fujitsu laser, $T = 24^\circ\text{C}$, 100MHz.	109
4.5	SFDR and intermodulation distortion at two different attenuations, conditions as above.	109
4.6	SFDR versus current, at three different temperatures, at (a) 10 MHz, (b) 100 MHz, (c) 450 MHz, and (d) 900 MHz.	110
4.7	SFDR versus current, at four different frequencies, at (a) 0°C , (b) 15°C , and (c) 24°C	111
4.8	SFDR versus Frequency, for three different temperatures.	114
4.9	Noise figure versus frequency, for three different temperatures.	114
4.10	Fundamental versus frequency, for three different temperatures.	115
4.11	IMD3 at 5 dB attenuation versus frequency, for three different temperatures.	115

4.12	Measured (dashed) and calculated (solid) distortion relative to carrier. rescaled by modulation depth.	117
4.13	Plot of current that maximizes SFDR (minus the threshold current) vs temperature for four different frequencies.	120
4.14	Current at which SFDR is maximized, plotted on LI curves. (a) At lower temperatures, heating effects are present. (b) At higher frequencies, these points are roughly constant as temperature is changed.....	120
5.1	Three possible ways to improve SFDR.	124

LIST OF TABLES

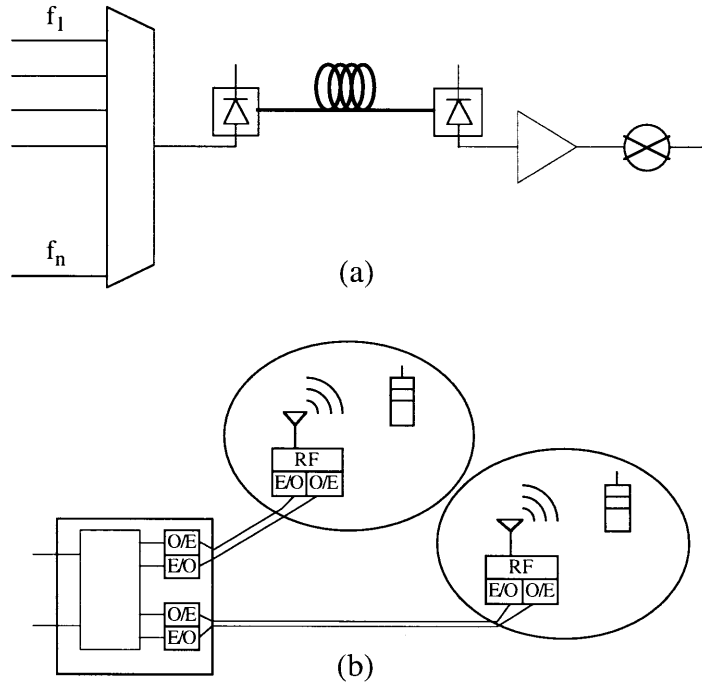
1.1	Three common semiconductor laser structures.	24
2.1	Driving terms for higher order distortion products	55
2.2	Parameters used in simulations	66

Chapter 1

INTRODUCTION

Increasing demand for communications over the last twenty years has fueled the need to find reliable transmission sources that can keep up with constantly changing requirements in broad band and narrow band communications. Cable television providers and telecommunications companies are competing to create broad-band subscriber networks that are upgradeable, flexible, and able to carry large bandwidths of various types of data. The wide bandwidths of semiconductor lasers and the accompanying fiber optic components are cost-competitive and compatible with existing coaxial cable system, thus making them attractive to cable providers as well as telecommunications companies. Through subcarrier multiplexing (SCM) a single network can handle multiple digital and analog formats, including voice, data, video, digital audio, high definition video, and any combination of these services.[28] There has also been great interest in narrow band analog optical applications, which include phase array radar and wireless broadcast communications. As their name implies, these applications require a relatively narrow bandwidth of channels. In wireless or personal communications systems (PCS), a central station switches between base stations in different “cells” as a mobile phone changes location.[35] The base stations are connected to the central station via fiber optic lines. More base stations can be added as demand for the service grows. Figure 1.1 illustrates both SCM and PCS systems.

Figure 1.1: (a) Subcarrier multiplexed systems (SCM). Multiple channels are fed into a single laser which transmits a signal over fiber optic cable to a detector, which can select the desired channel. [28] (b) Personal communications system (PCS). A central station keeps a phone in constant contact with a transmitting station by switching between different “cells”, which are linked fiber optically to the central station.[35]



Semiconductor laser devices have already proven themselves to be appropriate transmission sources; however, growing demands in both analog and digital communications continue to push the envelope of laser performance. In order to meet the requirements of the optical networks, lasers are required to deliver a low noise, low distortion, high-power output over a range of operation parameters, preferably with lower current bias. Furthermore, the necessity to couple light into fiber and propagate signals for long distances along the fiber requires that the lasers be dynamic single-mode (DSM) devices, which means that they must have a large side mode suppression ratio (>30dB) and they must be single mode throughout operation. In designing lasers that will meet the needs of both analog and digital communications, the distributed feedback (DFB) laser has emerged thus far as the best structure. Increasing demands of communications systems, however, will require improved performance of the DFB laser.

1.1 What is a semiconductor laser?

All lasers, whether they are gas, liquid, solid-state, or semiconductor devices, ideally emit light with the following three properties:

1. the light is monochromatic (of a single wavelength),
2. the light is coherent (the photons are all in phase with each other), and
3. the light is minimally divergent.

A laser typically has four main parts to it: (a) a gain section, (b) an optical pumping or electrical injection section, (c) a feedback or mirror section, and (d) an output coupler. Through optical pumping or electrical injection, electrons are raised to a higher energy state. Photons that are passing through the gain section cause the excited electrons to fall back down to the lower state and in the process emit photons of the same wavelength and in phase with the original photons. This process is known as stimulated emission. Most of the photons are then reflected and pass through the gain section again; a certain fraction of photons leave the cavity through an output coupler.

Semiconductor diode lasers operate on the same general principles as all other types of lasers, but they differ greatly in detail. Diode lasers have been useful in the communications industry because they have been shown to be reliable, they can be placed in a small package, and they can be directly pumped by an electrical current. This last feature makes it possible to realize high power conversion efficiencies as compared to gas and solid-state lasers.[9]

Semiconductor lasers are usually grown with material from column III and V of the periodic table, although lasers have been demonstrated that were grown using materials from columns II and VI. The laser is typically formed by creating a p-i-n diode structure. Electrons are injected through the n-doped side and holes are injected through the p-doped

side. The electrons and holes recombine in the intrinsic section, thus emitting light. The n- and p-type regions have a higher energy bandgap than the intrinsic region and thus they confine the carriers to the active region. Furthermore, the lower index of refraction of the n and p-type regions creates a waveguide which confines the light in the structure. These diode lasers operate through the stimulated emission of light from the active region.

The choice of wavelengths for laser operation in communications applications has been determined by the characteristics of the glass fiber. Fiber has a minimum loss at 1.55 μm and a minimum dispersion, or frequency-dependent broadening of pulses, at 1.32 μm . These two wavelengths are the primary choices for communications lasers. The bandgap of the material is related to the wavelength by the relation $E_g = \frac{hc}{\lambda}$. Thus, the desired wavelengths limit the types of materials from which the lasers can be grown. The most popular material system for lasers used in long-distance fiber optics has been InGaAsP active region grown on an InP substrate.[9] The choice of material systems as well as the actual growth process determine many other material parameters which can affect performance. Some of these parameters will be discussed in later chapters.

While the basic framework described above is common to most semiconductor lasers, the specific internal structure of the semiconductor lasers vary greatly. There are multiple

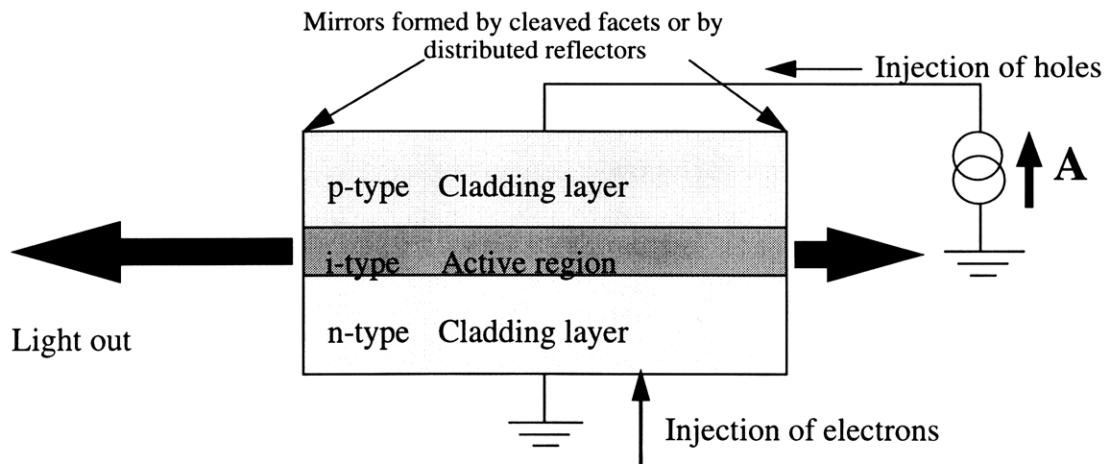


Figure 1.2: Generic DFB or Fabry-Perot laser structure.

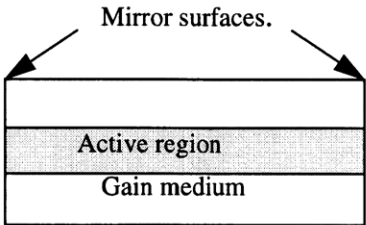
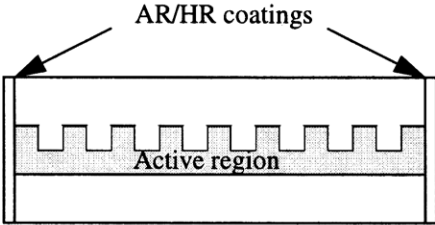
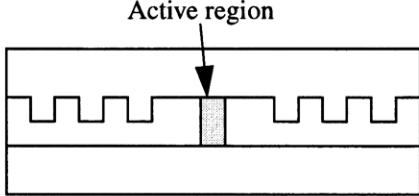
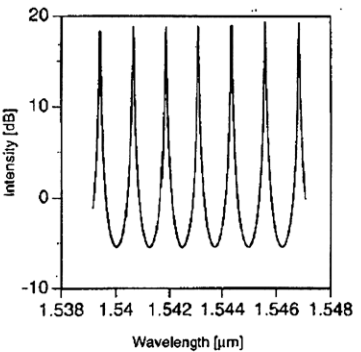
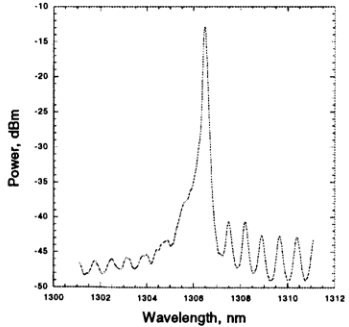
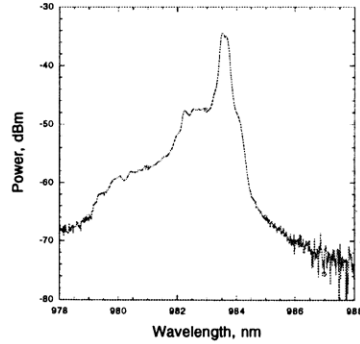
ways to reflect light back into cavities and there are many materials that can serve as appropriate gain mediums and light confining regions. Table 1.1 illustrates three common types of semiconductor laser structures and lists some of their basic properties. As is apparent from this short list, the properties of the different lasers vary greatly and different lasers may be better suited for certain applications.

Fabry-Perot lasers, which have been around since the early 1960's, are the simplest type of semiconductor lasers. The structure is formed by epitaxially growing the cladding and active layers, and the mirrors are formed by cleaving the semiconductor. While Fabry-Perot lasers are easy to make and can yield high output powers, they have low static and dynamic side mode suppression ratios (SMSR). Thus, they do not satisfy the requirements for dynamic single-mode transmission.

Vertical cavity surface emitting lasers (VCSELs) are formed by growing a distributed Bragg-reflector section, followed by an active layer with multiple quantum wells, and then followed by another passive distributed Bragg reflector section. VCSELs show promise for analog communications, but as of yet they have not demonstrated high enough output power and are complicated to grow.[13]

Distributed feedback lasers were first proposed by Kogelnik and Shank in 1971.[22] A DFB laser is fabricated by first epitaxially growing the p-i-n structure, followed by successive steps of etching and regrowth. A periodic grating is formed by holographic exposure or by electron beam lithography.[25] The periodic grating leads to coupling of forward and backwards going waves in the structure. The feedback is highly wavelength dependent, and thus the DFB laser leads to much better mode selectivity than the Fabry-Perot laser. In addition, DFB lasers have shown high output powers, low distortion, single mode operation, relatively low noise, and low current requirements. DFB lasers have been modified in many ways to improve particular aspects of performance. DFB lasers

Table 1.1: Three common semiconductor laser structures.

Property	Fabry-Perot	Distributed Feedback (DFB)	Vertical cavity surface emitting laser (VCSEL)
Profile			
Mirror surfaces	Mirrors formed by cleaved ends.	Forward going wave coupled to backwards going wave by periodic index or gain variation, causing feedback of waves.	Mirrors formed by passive Bragg reflectors (BR) on both ends of structure. Periodic index variation causes forward and backwards going waves to couple together. BR has high mode selectivity.
Output spectrum	<p>Spectrum below threshold</p> 	<p>Spectrum above threshold</p> 	<p>Spectrum above threshold</p> 
Number of modes	Multiple modes possible.	Single mode.	Single mode.
Fabrication	Simplest process.	More complicated, lower yield due to uncontrollable grating phase at facets.	Most complicated structure.
Disadvantages for fiber optic communications	Does not satisfy dynamic single mode (DSM) criteria.		Not enough power output yet. Low yield. Strong heating effects.

are already being used successfully in communications systems; however, in building the next generation optical communications systems, the performance in all of these area will have to be improved.

1.2 Performance limitations

The performance of laser diodes for optical communications is limited by application bandwidth, distortion, and noise. Distortion can be caused by many factors. Static distortion occurs when the nonlinearities of the light-versus current (LI) curve are present. These nonlinearities are caused by spatial hole burning, gain compression, finite carrier transport times, and leakage currents. Dynamic distortion occurs when the nonlinearities of the device cause different frequency components to mix together through the interaction of photons and electrons in the laser cavity. As a result of these nonlinearities in the device, it is possible for multiple frequencies from separate channels to interfere and mix with each other to produce new frequency components.

The application bandwidth determines the type of distortion that will affect the system. As is shown in Figure 1.3, a narrow band system will be primarily affected by third order intermodulation distortion (IMD3). The key figure of merit for such narrow band applications is the spurious free dynamic range (SFDR), which is the range of inputs over which the output signal is unaffected by either noise or distortion. In contrast, a broad band system can be affected by IMD3 as well as by second order harmonic and intermodulation distortion. The key figures of merit for broad band systems are the composite second order (CSO) distortion and the composite triple beat (CTB) distortion. In this report,

we focus on narrow band systems, i.e., systems that are limited by the third order inter-modulation distortion.

Performance is also limited by the noise in a laser device, which is characterized by the relative intensity noise (RIN) and the linewidth. Both types of noise are related to random carrier and photon fluctuations within the laser cavity. The linewidth is related to the phase noise and the RIN is related to the amplitude noise due to these random fluctuations.

Analog applications have stricter demands than digital applications for noise and distortion. Digital applications are merely required to be able to discern between a high bit value and a low bit value. The actual data is made up of a series of these high or low bits. Noise and distortion can be tolerated as long as they do not change the value of the transmitted information. Requirements for digital systems are given in terms of bit error rates, or the number of errors that can be tolerated per number of bits transmitted.

Nonetheless, analog communications are still of interest because a majority of phone and voice communications still transmit using analog signals. In analog systems, the data value is chosen from a continuous range of values. Analog systems operate by converting a current modulation into the laser to a light output modulation which is transmitted across fiber, received at the other end and then reconverted into a current modulation. Proper operation requires that the laser and detector both be as linear as possible and have mini-

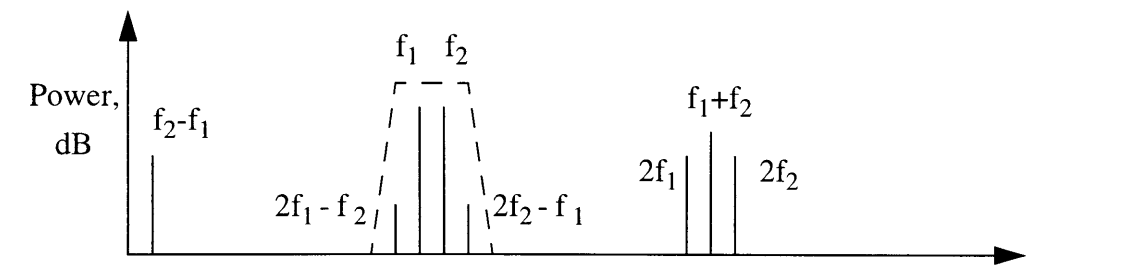


Figure 1.3: Distortion products for broad-band and narrow-band applications. The dashed line shows that for narrow-band, performance will be limited by IMD3.

mal noise and distortion. Low distortion, high-bandwidth detectors are already available, and usually the lasers are the limiting elements in optical links. Even a little bit of noise or distortion in the laser can significantly limit the quality of the transmitted signal. Thus DFB lasers for analog applications must be designed with very low distortion and noise.

1.3 Previous work done in this field

There has been much research done in designing high-linearity DFB lasers for analog applications with low distortion. We only present a brief outline here of investigations relating to high-linearity index coupled DFB lasers for analog transmission links.

Intermodulation distortion in semiconductor lasers was first examined in 1984 by Yariv and Lau [23]. Subsequent to this, many others have measured the intermodulation distortion for different types of applications. Many of these other investigations have focused on relating the distortion to the device structure. Watanabe *et al.* [35] study the effects of strain and multiple quantum wells on distortion and report third order intermodulation distortion of -88 dBc in a 1.3- μm strained multiple quantum well DFB laser for analog transmission at 1.9 GHz. Haisch *et al.* [16] report a low-chirp, highly-linear 1.5- μm strained layer multiple quantum well DFB laser for analog TV systems. Yonetani *et al.* [37] report a Fujitsu DFB laser that is optimized for second order intermodulation distortion by varying the coupling coefficient and the mesa width.

While there have been many investigations into relating the structure to the distortion, there have been fewer studies comparing the relative effects of the different laser nonlinearities to the distortion. Okuda *et al.* [26] report an internal distortion cancellation mechanism due to the cancellation of relaxation oscillation and longitudinal spatial hole

burning. Understanding the relative effects of the nonlinearities may help in designing new lasers which optimize the different nonlinearities and thus reduce the distortion.

Another area where DFB lasers may improved is through reducing temperature sensitivity of the laser. This may eliminate the need for a peltier cooling module and thus help bring the packaging costs down. Watanabe *et al.* [36] report an uncooled DFB laser with low distortion for CATV applications; this laser is made with a current blocking layer to reduce the effects of leakage current, another nonlinearity which can lead to increased distortion.

1.4 Research presented in this thesis

In this thesis, we analyze the performance of DFB lasers for analog applications, including distortion, noise, and spurious free dynamic range. In order to understand what factors may be limiting performance and how to overcome these issues, we explore the following:

- We present simulations of steady state, modulation, and third order intermodulation distortion for a Fabry-Perot laser. This gives an understanding of how similar processes affect a DFB laser.
- We give a complete characterization of a highly-linear Fujitsu DFB laser (model FLD 130F3ACH-AL/180), which is designed for CATV analog communications. These measurements include optical spectrum below, at, and above threshold, LI curves at several temperatures, third order intermodulation distortion, spurious free dynamic range, and relative intensity noise.
- We will present a short algorithms for extraction of length and coupling coefficient

from a subthreshold spontaneous emission spectrum of a DFB laser.

- We observe the effects of temperature changes on dynamic range and we calculate a characteristic temperature for threshold current.
- We observe and measure a peak in the dynamic range versus current. This maximum in the dynamic range is believed to occur from cancellation of spatial hole burning and gain compression in a DFB laser.
- We present the outline for several LabVIEW data acquisition programs that were written to measure spurious free dynamic range over either a frequency range or over a range of current biases. Appendix A documents the steps taken in the program in greater detail.

1.5 Outline of this report

We start our analysis in Chapter 2 by presenting the laser rate equations for Fabry-Perot lasers. We also present the modulation response of the lasers and the laser performance limitations due to distortion and noise. We introduce the system measurement for spurious free dynamic range (SFDR). We present our measurements of RIN and power-current (LI) curves for a Fujitsu DFB laser, from which we extract many of the key modeling parameters for the laser. We then present simulations which were done in MATLAB using these parameters. These simulations were based on the simple rate equation analysis with gain compression.

In Chapter 3, we present the distributed feedback (DFB) laser analysis, using coupled mode theory. From coupled mode theory and perturbation analysis, we determine the expected mode profiles, and the impact of spatial hole burning on DFB lasers. We

present a short algorithm for parameter extraction from a subthreshold spontaneous emission spectrum for a DFB laser.

In Chapter 4, we present the high speed measurements. We present the experimental setup and data. We discuss the results and compare with previous results from other groups. Based on these analyses, in Chapter 5 we summarize our results and we propose a direction to follow for further research in this area.

Chapter 2

LASER DISTORTION THEORY

In this chapter we examine the steady state, modulation, and distortion characteristics of a Fabry-Perot laser using rate equations. A Fabry-Perot laser is the simplest type of semiconductor laser, consisting of a gain medium and two mirrors which are formed when the semiconductor is cleaved along the crystal planes, leading to a very clean cut mirror surface. A Fabry-Perot laser has many natural cavity modes which compete with each other to reach threshold. One down side of the Fabry-Perot is that there is not enough mode selectivity, and the laser may end up with multimode stimulated emission. Nonetheless, the simplicity of the Fabry-Perot laser makes analysis of its properties a good place to start. We will extract many key parameters from a laser and use these parameters in simulations of static and dynamic characteristics of the laser. In the next chapter, we will look at a distributed feedback (DFB) laser, which has the advantage of single mode emission and is thus better suited for fiber optic communications. We will be able to apply many of the results that we find in this section to the DFB laser in the next section.

2.1 Laser rate equation analysis in steady state

2.1.1 Phenomenological description

We will start with the analysis of a Fabry-Perot laser in the steady state, based on the notation found in Coldren and Corzine [9]. The analysis for lasers is typically done using rate equations to model the population changes of carriers and photons. In the present analysis, the Fabry-Perot lasers are modeled by two rate equations, one for the electron carrier density, N , and one for the photon density, S . The rate equations have the form:

$$\frac{dN}{dt} = \text{Injection rate} - \text{Carrier decay rate} - \text{Net stimulated emission rate}$$

$$\frac{dS}{dt} = \text{Net stimulated emission rate} + \text{Spontaneous emission rate} - \text{Photon decay rate}$$

The exact form of the rate equations that we will use is given by [9]:

$$\frac{dN}{dt} = \frac{\eta_i I}{qV} - \frac{N}{\tau} - v_g g S \quad (2.1)$$

$$\frac{dS}{dt} = \Gamma v_g g S + \Gamma \beta B N^2 - \frac{S}{\tau_p}, \quad (2.2)$$

where η_i is the internal quantum efficiency, $q=1.6 \times 10^{-19}$ J/Coul, V is the volume of the active region, τ is the carrier lifetime, v_g is the group velocity, g is the gain function, Γ is the carrier confinement factor, β is the spontaneous emission factor, τ_p is the photon lifetime, and B is the bimolecular recombination coefficient. Equation 2.1 shows that the rate of change of the carrier density, N , is equal to the rate of generation of carriers, which are injected as a result of the current I , minus the rate of recombination due to decay, and minus the recombination due to stimulated emission. Equation 2.2 shows that the rate of change of the photon density, S , is equal to the rate of generation of photons by stimulated

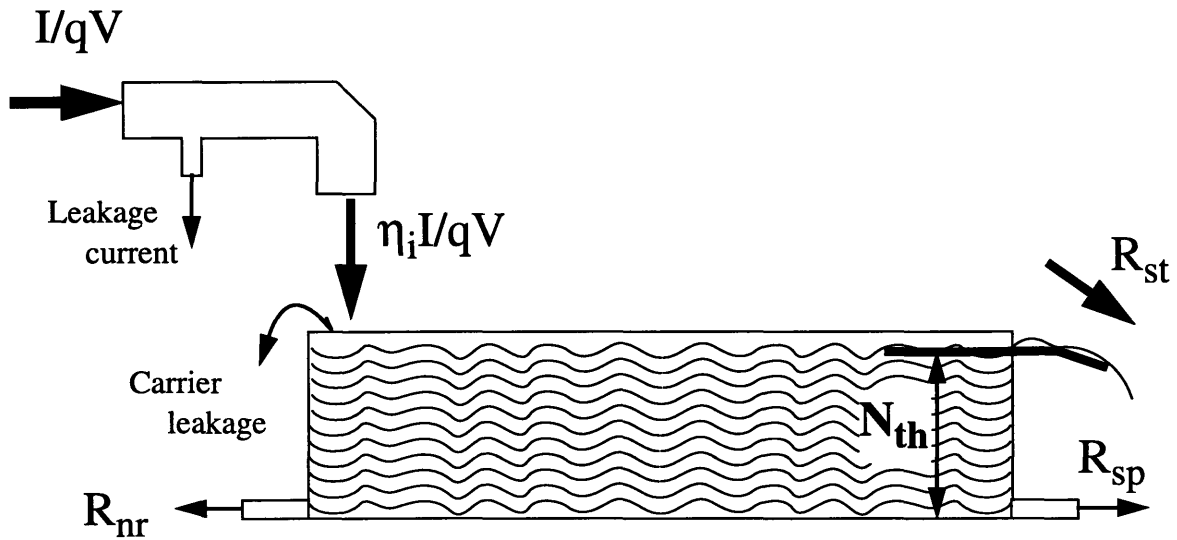


Figure 2.1: Analogy between steady state laser and water flow. Based on Coldren and Corzine.[9]

emission minus the rate of spontaneous emission into undesired modes and minus the decay of photons due to generation of carriers or loss out of the cavity.

Coldren and Corzine make an analogy between the laser and the rate of water flow out of a faucet into a container. In this analogy, the rate of water flow out of the faucet represents the current injected into the laser, and the height of the water represents the number of excited carriers. As seen in Figure 2.1, water is flowing in the faucet at the rate of I/qV , but only a fraction η_i makes its way into the container of water. In the laser, this loss corresponds to the injection losses caused by carrier leakage and leakage currents. The water can fill the container up to a threshold level of N_{th} , after which point all additional water that is added will spill directly out of the container. This spillage of water out of the top corresponds to reaching lasing in the laser, and the rate of water spillage corresponds to the rate of stimulated emission (R_{st}). The height of the water is essentially clamped - any additional water added to the container will not raise this level.

The water can also escape from two openings in the bottom of the container; these openings allow undesired losses of carriers due to spontaneous emission into different modes (R_{sp}) and due to nonradiative recombination (R_{nr}). These losses are represented in the carrier rate equation (2.1) by the second term on the right side, N/τ :

$$\frac{N}{\tau} = R_{sp} + R_{nr} = (BN^2) + (AN + CN^3). \quad (2.3)$$

The rate of spontaneous emission is dependent upon the bimolecular recombination coefficient B , which is typically on the order of $10^{-10} \text{ cm}^3/\text{s}$. Spontaneous emission occurs when an electron in an excited state spontaneously falls to a lower state and emits a photon. Unlike the case of stimulated emission, this spontaneously emitted photon has a random phase and is not necessarily correlated with any other photon. Because spontaneous emission requires the presence of both an electron and a vacancy, the emission rate is proportional to the carrier density squared. Spontaneous recombination occurs into all of the natural modes that are supported by the cavity size and that fall within the bandwidth of the spontaneous emission spectrum. Larger cavities will have spontaneous recombination into more modes. The spontaneous emission term also shows up in the photon density rate equation because a certain fraction of the spontaneous emission will end up in the desired lasing mode. The fraction of light that ends up in this desired mode is given by β

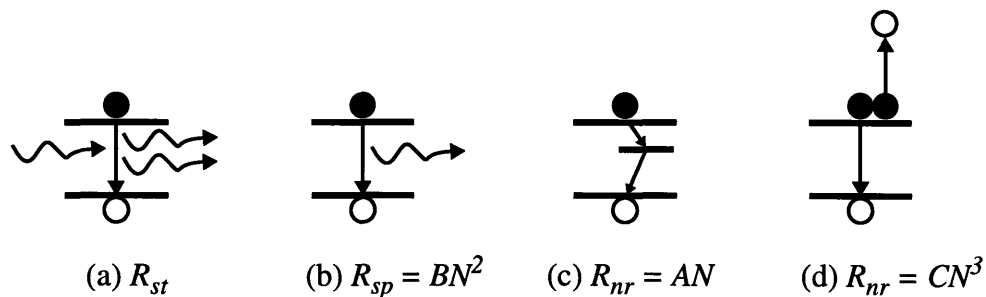


Figure 2.2: Four types of recombinations. (a) Stimulated emission, (b) Spontaneous emission, (c) Nonradiative recombination due to trap, and (d) Auger recombination.

and is inversely proportional to the number of modes supported by the cavity. Thus, β is a measure of the probability that a photon created by spontaneous emission will randomly end up in the desired mode that is lasing and thus contribute to the total light output at that frequency. The more modes there are, the less likely it is that the photon will randomly end up in the desired mode.

Nonradiative recombination occurs in two forms. One form is due to nonradiative centers in the active region of the laser, including point defects, surfaces, and interfaces. This process only requires the existence of a single particle, as opposed to spontaneous emission which both depend on the existence of two particles. Thus the recombination rate due to this first process is proportional to the carrier density, N . This form of recombination is less important for InP materials and is usually ignored.[9]

The other form of nonradiative recombination form is the Auger process, in which the electron-hole recombination energy is transferred to another particle. Figure 2.2(d) depicts one of the four possible forms of Auger recombination in which the third particle is excited to a higher level in the conduction band. This process requires the existence of three particles and is thus proportional to carrier density cubed, N^3 . The associated Auger coefficient, C , is on the order of $10^{-29} \text{ cm}^6/\text{s}$.[9] As its name implies, nonradiative recombination does not result in photon emission and thus does not show up in the photon density rate equation.

2.1.2 Lasing, loss, and gain

Now that we have given a basic description of the way a laser works, we now look at lasing, loss, and gain in greater detail. First we will examine what lasing is and when it occurs. In order for lasing to occur, the roundtrip gain must compensate for the roundtrip loss. This means that the system is supplying energy to the one mode of interest at the same rate that energy is being lost from that mode. The energy is lost in two ways: internal loss and loss at mirrors. The internal losses are due to waveguide loss and scattering in the material. While the internal losses can be decreased slightly depending on how the material is grown, the internal loss parameter $\langle\alpha_i\rangle$ that characterizes the loss for materials is typically 10 to 20 cm^{-1} . The other type of loss occurs at the facets due to the transmission of light out of the cavity. At the mirror or facet interface, some of the light is reflected back into the cavity while the rest of the light leaves the cavity. The mirror loss parameter, α_m , is dependent upon the length of the cavity, L , and the power reflectivity of the mirrors, $r_1 r_2 = r^2 = R$:

$$\alpha_m = \frac{1}{L} \ln\left(\frac{1}{R}\right). \quad (2.4)$$

When light passes through a material with gain in a resonant cavity, lasing will start occurring if the gain compensates for the internal loss and the mirror loss in the cavity. At threshold when lasing just starts to occur, this can be expressed mathematically in the form:

$$\Gamma g_{th} = \langle\alpha_i\rangle + \alpha_m, \quad (2.5)$$

where g_{th} is the gain at threshold when stimulated emission starts to beat out spontaneous emission of light into other modes. Γ is a confinement factor that represents the fraction of mode energy within the active layer that can interact with the confined carriers. For a

Fabry-Perot laser, Γ simply equals the ratio of the volume of the active region to the volume of the entire cavity where photons are confined.

There are several expressions that can be used to model the gain. For an initial approximation in a bulk material, it is often satisfactory to utilize a linear gain model. This model is appropriate when the carrier density is near transparency. The carrier density clamps, or more accurately asymptotically approaches a threshold carrier density value N_{th} because the total number of carriers is physically limited. Above N_{th} , the gain asymptotically approaches a threshold value g_{th} . The model for the gain is given by:

$$g = a(N - N_{tr}) \quad (2.6)$$

where a is known as the differential gain. N_{tr} is the transparency carrier density, the density at which the rate of stimulated emission equals the rate of stimulated absorption. For quantum well active regions, the gain is best modeled by a logarithmic function:

$$g = g_0 \ln\left(\frac{N + N_s}{N_{tr} + N_s}\right), \quad (2.7)$$

where g_0 is a constant and N_s is a shift used for fitting the gain curve.

Gain compression

An even better model of the gain will take into account gain compression, which is the decrease of the effective gain at high currents caused by carrier depletion. Gain compression can be caused in several different ways: spectral hole burning, spatial hole burning, carrier transport related phenomenon, or carrier heating. The large photon densities reduce the number of carriers available. When this happens as a function of position in the laser cavity, this is known as spatial hole burning (discussed in greater detail in the next section). When carrier depletion occurs as a function of the wavevector in momen-

tum space, it is known as spectral hole burning. A model that takes gain compression into account has the form

$$g = \frac{1}{1 + \epsilon S} a(N - N_{tr}), \quad (2.8)$$

where ϵ is known as the gain compression factor. As the photon density, S , increases at large current biases, the denominator will become large and the effective gain will decrease, or compress. Gain compression will lead to sublinear nonlinearities in the LI curve, which means that the LI curve rolls over for high current biases, as shown in Figure 2.3 for three different values of the gain compression factor. This nonlinearity will contribute to harmonic and intermodulation distortion in the laser, even for small values of ϵ . Thus the nonlinearity in the LI curve due to gain compression will lead to increased distortion and will limit the laser performance. Gain compression is important at currents far above threshold.

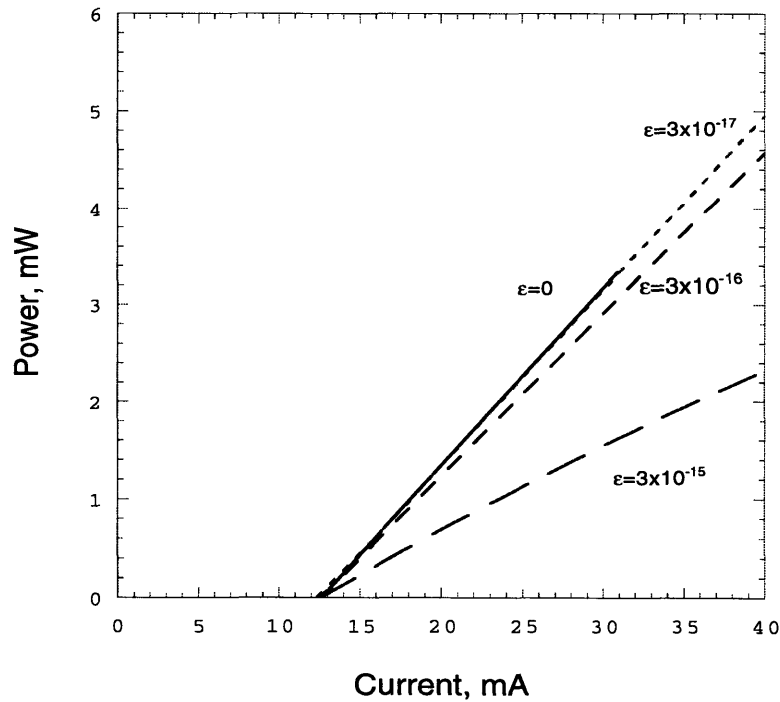


Figure 2.3: Simulated LI curves with gain compression, for four values of ϵ . The case of $\epsilon=0$ and $\epsilon=3 \times 10^{-17}$ are indistinguishable for this current range.

Spatial hole burning

The optical field distribution in a laser above threshold is usually not uniform. Spatial hole burning occurs when an area of strong optical field intensity leads to a lower carrier distribution in that area. For a Fabry-Perot laser, the optical field distribution is maximum at the facets of the device. For a DFB laser the field distribution is dependent upon the coupling coefficient, as discussed in Chapter 3.

Spatial hole burning is more important at lower frequencies (owing to finite carrier lifetimes). It is possible to calculate a cutoff frequency above which spatial hole burning is no longer an important effect. Morthier [25] calculates the expression for the spatial hole burning cutoff frequency ($\Omega_{SHB}/2\pi$) from the spatially dependent carrier and photon densities:

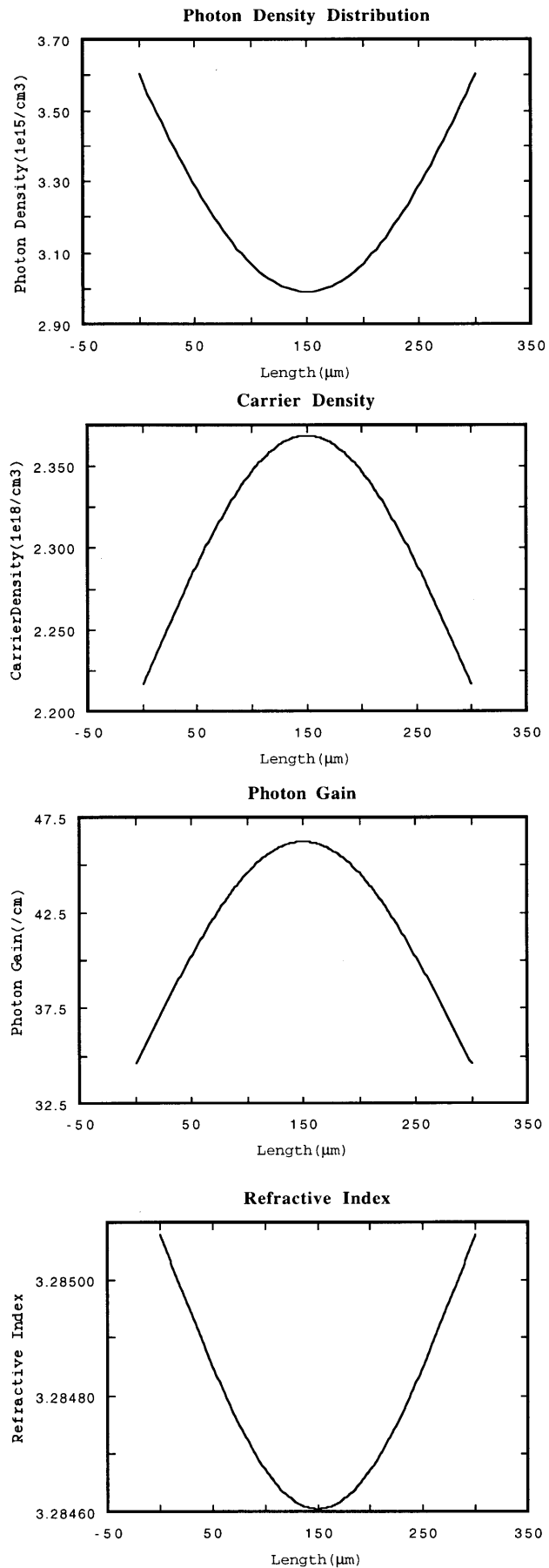
$$\Omega_{SHB} \approx A + 2BN_{av,0} + 3CN_{av,0}^2 + v_g \frac{\partial g}{\partial N} S_0, \quad (2.9)$$

where N_{av} is the average carrier density integrated over the cavity length, and the subscript 0 indicates that the values are the bias values. The cutoff frequency increases with increasing bias levels. Calculations indicate that the cutoff frequency is on the order of a few gigahertz and is generally smaller than the resonance frequency. Thus, spatial hole burning does not affect the damping of the relaxation oscillations.

It was initially thought that spatial hole burning could be simply included as a lumped element in the gain compression; however, SHB is dependent upon longitudinal position and may in fact have an opposite sign as the gain compression under certain conditions. The functional form of spatial hole burning requires a more complicated set of rate equations than used here. In order to incorporate spatial hole burning, the rate equations would have to be written to include a spatial dependence to account for the fact that the photon and carrier distributions are not longitudinally uniform in most devices. Using such a spa-

tially dependent rate equation model, it has been determined that spatial hole burning can lead to either a sublinear LI curve (leading to additional roll over) or to a superlinear LI curve. In this latter case, gain compression and spatial hole burning can have opposite effects on the LI curve of a laser. At a certain point, the two effects may actually cancel out, leading to a cancellation of the nonlinearities caused by these two effects. This is a point of great interest as it may help to find the optimum point at which to operate a laser if we want to minimize distortion caused by nonlinearities. This topic will be addressed again in Chapter 4. In both the sublinear and superlinear cases, spatial hole burning is important at smaller currents right above threshold; at larger currents, the SHB effect saturates.

Figure 2.4: (a) Photon density, (b) carrier density, (c) photon gain, (d) and refractive index in 300 μm Fabry-Perot laser at 5 times threshold current. Simulations performed using LaserMatrix (Royal Institute of Technology, Sweden). Simulations indicate the effect of spatial hole burning on the carrier density at the facets of the device, leading to a decrease in the gain and an increase in the refractive index.



2.1.3 Light output

Ultimately, we are interested in knowing the power output from the laser. The power is most commonly displayed on an LI curve which plots the power output into the single lasing mode versus the current input. The power is determined from the expression:

$$P_o = F_1 v_g \alpha_m h \nu S V_p, \quad (2.10)$$

where h is Planck's constant, ν is the frequency of the output light, and V_p is the volume of the cavity that confines the photons. F_1 is a structure related term that determines how much of the light comes out of a particular facet. While there are expressions to determine F_1 based on transmission and reflection coefficients of the facets, these expressions do not account for the facet phase dependence at the edge of DFB lasers. For DFB lasers, F_1 must be determined empirically. Nonetheless, all of the terms on the right hand side of equation 2.10 are independent of input current except for the photon density, S . Thus, the power output is directly proportional to the photon carrier density. An LI curve for the Fujitsu DFB laser is shown in Figure 2.11. Measurements were taken at six different temperatures.

We can get an approximate expression for the photon density, S , above threshold using the rate equations. Ignoring the carrier decay time in equation 2.1, we find:

$$S = \frac{\eta_i (I - I_{th})}{q V v_g g_{th}}. \quad (2.11)$$

To get a more accurate expression for the photon density, we must parameterize equations 2.1 and 2.2 and solve them numerically. It is necessary to solve these equations parametrically because we need to keep track of the carrier density and make sure it does not exceed the threshold limit. Furthermore, when gain compression is included, the analyti-

cal solutions become difficult to handle because they are highly nonlinear. Thus, it turns out that it is necessary to numerically simulate the rate equations for realistic parameters of the laser in order to get a better understanding of how changing the parameters affects the output of the laser. Once we have gotten a steady state response for the laser, we will be ready to look at the modulation response for the system.

Mode spectrum

Although the laser will typically have stimulated emission into one mode, there are several modes that will have spontaneous emission. In a Fabry-Perot device the modes are spaced very close to each other. The separation is given approximately by

$$\Delta\lambda_{FP} = \frac{\lambda^2}{2n_g L}, \quad (2.12)$$

where λ is the wavelength of the mode, L is the length of the device, and n_g is the group index of refraction. The gain curve on the other hand is typically very broad and overlaps many Fabry-Perot modes. The mode with the lowest threshold gain is the mode that will begin lasing. Figure 2.5 shows a typical output optical spectrum for a Fabry-Perot device, both below and above threshold. Many modes have spontaneous emission below threshold, but not all modes reach the threshold gain condition. Ideally for communications lasers there is only one mode that reaches threshold; however, multimode stimulated emission may occur in poorly designed lasers or in lasers at high output powers where spatial hole burning reduces the loss of the side mode. Fabry-Perot lasers are particularly sensitive to this effect, while DFB lasers are less sensitive to this effect.

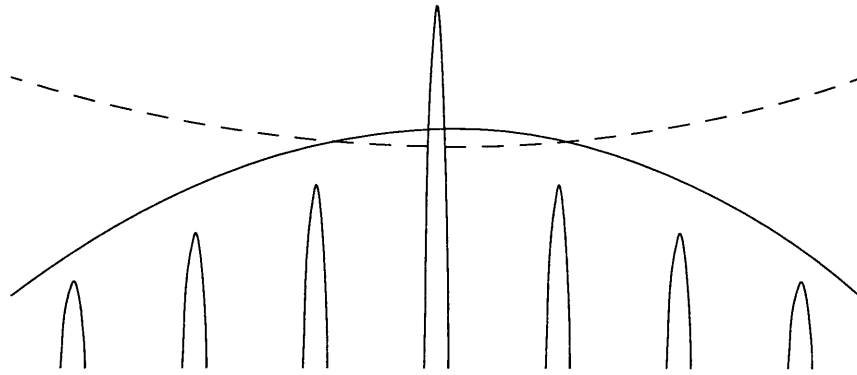


Figure 2.5: Closely spaced modes in a Fabry-Perot structure. The broad solid line is the gain curve, and the dashed line is the threshold gain curve. The mode that falls under the gain curve and has the lowest threshold gain will reach stimulated emission first. Other modes could also possibly begin to lase if they reach threshold.

2.1.4 Temperature effects

Temperature changes result in a modification of the steady state characteristics of a laser [9, 25]. For Fabry-Perot and DFB lasers in the 1.3 - 1.55 μm wavelength range, there are four primary effects that occur as a result of a change in temperature. One effect is a change in the Auger recombination: increasing the temperature results in an increase of the Auger recombination rate. As described in section 2.1.1, Auger recombination requires the presence of three carriers or holes, depending upon the type of Auger recombination. The probability of finding these states occupied or empty increases exponentially with temperature. Thus as the temperature is increased, the Auger process will become more important, resulting in higher nonradiative losses.[9]

Another change is a decrease in the injection efficiency with a rise in temperature. At higher temperatures, electrons have a higher average energy and are more easily excited out of the confining region. When this occurs, more electrons must be supplied in order to maintain a desired output level and thus the injection efficiency is decreased.

Another effect in the device is the temperature dependence of the gain. Increasing temperature reduces the bandgap and results in a broadened Fermi-Dirac distribution of the electrons and holes over larger energy ranges. The decreased bandgap results in a temperature shift of the gain peak towards longer wavelengths. In a Fabry-Perot device, the shifting gain peak may result in mode-hopping as the gain peak begins to overlap longer wavelength modes. DFB lasers are less affected by the gain peak shift. The broadening of the Fermi-Dirac distribution results in a flattening of the gain curve, which means that more carriers must be injected to achieve the same level of gain.[25]

Another temperature related effect is leakage current. Leakage currents are formed by current paths that do not properly make their way into the active region.[25] They form an undesirable leakage diode in parallel with the laser diode. The currents flowing through the leakage diodes are temperature sensitive due to the temperature sensitivity of the resistance of the material.

All of the above effects can influence the performance of a laser. The effect can be empirically expressed through a characteristic temperature, T_0 . The threshold current is roughly related to temperature exponentially:

$$I_{th} = I_0 e^{T/T_0}. \quad (2.13)$$

By fitting data to an exponential, we can extract the characteristic temperature T_0 . Small values of the characteristic temperature indicate that the laser is more sensitive to temperature changes.

Temperature effects generally are important at lower frequencies. This is because the thermal effects can only propagate at a finite speed, and at higher modulation frequencies there is not enough time for the thermal transients to make a large difference. The exact cutoff frequency for temperature related effects is difficult to determine as it depends on

the structure of the device and the type of heat conduction and heat sinking provided leading to heat removal from the main laser cavity. Thermal time constants are typically as low as a few hundred kilohertz.[9]

The results of this section apply both to Fabry-Perot lasers as well as DFB lasers. In the last section of this chapter, we extract the characteristic time constant for a DFB laser.

2.2 Modulation response

In section 2.1, we presented the characteristics of the laser equations for the steady state case, i.e. when both $\frac{dN}{dt} = 0$ and $\frac{dS}{dt} = 0$. We now present the modulation response properties of the lasers. This will form the basis for subcarrier multiplexed systems, with multiple channels or signals that are separated by a small spacing in the frequency domain. Thus, we would like to examine the modulation response of our laser to determine how to improve the laser. After we have examined the modulation response of the laser, we can then discuss what are the causes of distortion in the laser systems.

This derivation is based on Coldren and Corzine [9]. In order to undertake an analysis of the modulation response of the laser system, we must first assume a small signal analysis, i.e. assume that the dynamic changes are small and so we can take the differentials of I , N , S , and g . This allows us to linearize the system and eliminate all higher order terms that will be very close to zero. To find the small signal response of $dN(t)$ and $dS(t)$ to a sinusoidal current response, we assume solutions of the form:

$$I(t) = I_0 + I_1 e^{j\omega t}, \quad (2.14)$$

$$N(t) = N_0 + N_1 e^{j\omega t}, \quad (2.15)$$

$$S(t) = S_0 + S_1 e^{j\omega t}. \quad (2.16)$$

We expand the gain:

$$g = g|_{N=N_0} + a_N(N - N_0) - a_P(S - S_0) \quad (2.17)$$

For a linear gain model with gain compression as given by equation 2.8, we have:

$$a_N = \left. \frac{\partial g}{\partial N} \right|_{N=N_0} = \frac{a}{1 + \epsilon S_0} \text{ and} \quad (2.18)$$

$$a_P = - \left. \frac{\partial g}{\partial S} \right|_{S=S_0} = \frac{\epsilon a}{(1 + \epsilon S_0)^2} (N - N_{tr}) = \frac{\epsilon (g|_{N=N_0})}{1 + \epsilon S_0}. \quad (2.19)$$

Both the differential gain (a_N) and a_P become smaller at higher photon densities.

We now insert 2.14-2.16 into 2.1 and 2.2 and isolate all of the terms that have an $e^{j\omega t}$ phase factor. Reorganizing the terms into a matrix yields:

$$\begin{bmatrix} \frac{1}{\tau_{\Delta N}} + S_0 v_g a_N + j\omega & v_g g[N_0] + S_0 v_g a_P \\ -2\Gamma\beta B N_0 - \Gamma S_0 v_g a_N & \frac{1}{\tau_p} - \Gamma v_g g[N_0] - \Gamma S_0 v_g a_P + j\omega \end{bmatrix} \begin{bmatrix} N_1 \\ S_1 \end{bmatrix} = \begin{bmatrix} \eta_i I_1 \\ \frac{qV}{qV} \\ 0 \end{bmatrix}. \quad (2.20)$$

We define matrix elements as follows:

$$\begin{bmatrix} M_{11} & M_{12} \\ M_{21} & M_{22} \end{bmatrix} = \begin{bmatrix} \frac{1}{\tau_{\Delta N}} + S_0 v_g a_N & v_g g[N_0] + S_0 v_g a_P \\ -2\Gamma\beta B N_0 - \Gamma S_0 v_g a_N & \frac{1}{\tau_p} - \Gamma v_g g[N_0] - \Gamma S_0 v_g a_P \end{bmatrix}.$$

We would like to solve for N_1 and S_1 , the first order modulation responses in terms of the modulation current I_1 , the frequency ω , and the matrix elements M_{11} , M_{12} , M_{21} , and M_{22} .

We invert the matrix to get:

$$\begin{bmatrix} N_1 \\ S_1 \end{bmatrix} = \frac{H(\omega)}{\omega_R^2} \begin{bmatrix} M_{22} + j\omega & -M_{12} \\ -M_{21} & M_{11} + j\omega \end{bmatrix} \begin{bmatrix} \eta_i I_1 \\ \frac{qV}{0} \end{bmatrix} = \frac{\eta_i I_1 H(\omega)}{qV \omega_R^2} \begin{bmatrix} M_{22} + j\omega \\ -M_{21} \end{bmatrix}. \quad (2.21)$$

$H(\omega)$ is a constant divided by the determinant of the matrix on the left side of 2.20:

$$H(\omega) = \frac{\omega_R^2}{\omega_R^2 - \omega^2 + j\omega\gamma}, \quad (2.22)$$

where ω_R^2 is known as the relaxation resonance frequency; γ is known as the damping factor and is proportional to ω_R^2 . The relaxation resonance frequency is equal to $\omega_R^2 = M_{11}M_{22} - M_{12}M_{21}$; above threshold the relaxation resonance frequency can be approximated by:

$$\omega_R^2 = (2\pi f_R)^2 = \frac{v_g a_n S}{\tau_p} = \frac{v_g a_n \eta_i (I - I_{th})}{qV_p}. \quad (2.23)$$

The damping factor is $\gamma = M_{11} + M_{22}$, which equals:

$$\gamma = v_g a_n S \left[1 + \frac{\Gamma a_p}{a_n} \right] + \frac{1}{\tau_{\Delta N}} + \frac{\Gamma R'_{sp}}{s} = K f_R^2 + \gamma_0, \quad (2.24)$$

where $K = 4\pi^2 \tau_p \left[1 + \frac{\Gamma a_p}{a_n} \right]$ and $\gamma_0 = \frac{1}{\tau_{\Delta N}} + \frac{\Gamma R'_{sp}}{s}$. K describes the damping of the response for large resonance frequencies, and γ_0 is the damping factor offset which is important at low powers and low resonant frequencies.

The amount of modulation applied to a laser is often reported in terms of the optical modulation depth or modulation index. This term is sometimes defined as:

$$m = \left| \frac{\eta_i I_1 \tau_p}{qV_p \langle S \rangle} \right| = \frac{I_1}{(I - I_{th})}, \quad (2.25)$$

where we have replaced the photon density with equation 2.11. Distortion scales linearly with the modulation depth, and is often reported in terms of it.

The output power modulation is proportional to the photon density modulation amplitude S_I , and is also directly proportional to $H(\omega)$; thus plotting $H(\omega)$ gives us the same frequency dependence as the output power frequency response. Figure 2.6 shows the simulated modulation response for the case of without gain compression and with gain compression, respectively. Figure 2.6 (a), the case without gain compression, shows that there is damping at high and low output powers. This is because the imaginary term in the frequency response depends on both ω_R and $1/\omega_R$, which can be seen by combining equations 2.22 and 2.24. For low currents, the relaxation resonance frequency, ω_R , coincides with the peak, ω_P . As the current continues to increase, however, the relaxation resonance frequency moves to higher frequencies and passes the peak frequency. The damping increases and causes the peaks to flatten and broaden out. The height of the peak is given approximately by $(\omega_R/\gamma)^2$. The peak frequency is given by:

$$\omega_P^2 = \omega_R^2 \left[1 - \frac{1}{2} \left(\frac{\gamma}{\omega_R} \right)^2 \right], \quad (2.26)$$

and the 3 dB frequency, the frequency at which the modulation response drops to half of its DC value, is given by $\omega_{3dB}^2 = \omega_P^2 + \sqrt{\omega_P^4 + \omega_R^4}$. Increasing the current bias will increase the power output and the photon density, which will in turn increase the relaxation resonance frequency ω_R according to equation 2.23. This will cause the resonance peaks to shift to higher frequencies. The damping is proportional to ω_R^2 , and thus increasing the current bias will cause the peaks to flatten and broaden out. Figure 2.6 (b) shows that the damping is significantly greater with gain compression taken into account. The parameters used in the simulations are given in Table 2.2.

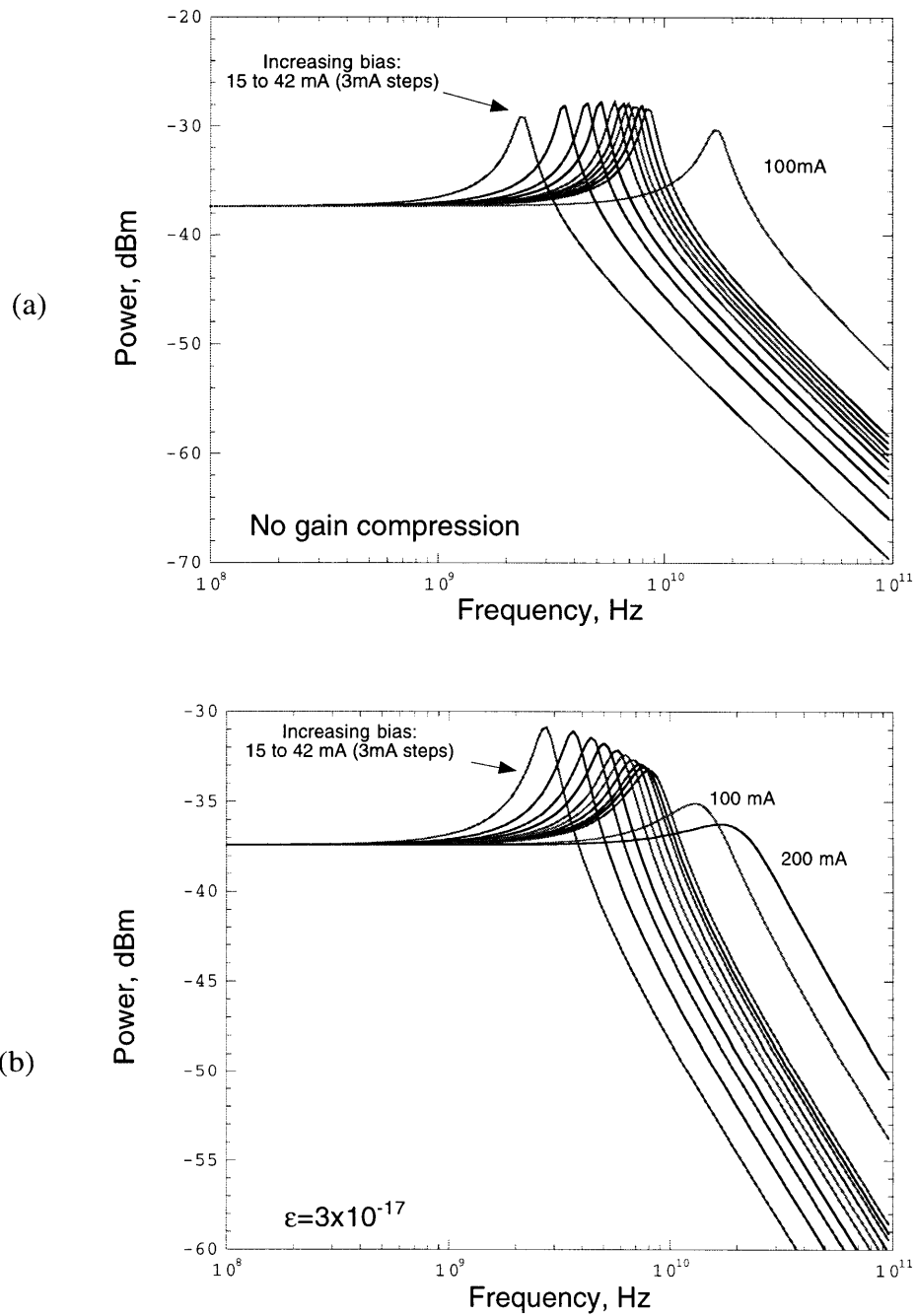


Figure 2.6: Modulation response, (a) no gain compression. (b) with gain compression. ($\epsilon=3 \times 10^{-17}$).

2.3 Performance limitations

The limitation on performance of a device is dependent upon the distortion of the device due to internal nonlinearities, the noise of a device due to poor design or fundamental noise limits, and the system bandwidth requirements. Distortion occurs when nonlinearities in the device or system cause frequency components to add in an undesirable way and reappear at different frequencies. The system performance will be limited by distortion products that reappear within the frequencies occupied by the application. One of the primary factors in determining the laser performance limitation is the system bandwidth. System applications fall into two categories: narrow band and broad band applications. Broad band applications, such as cable television (CATV) systems, occupy a wide range of frequencies. Broad band applications are influenced by second order intermodulation and harmonic distortion, as well as third order intermodulation distortion. In general, a single fiber may carry on the order of one hundred channels which could potentially interfere with each other. The interference of these channels for broad band applications is quantified by the composite second order (CSO) distortion for second order distortion and by the composite triple beat (CTB) for third order distortion. While most system requirements are reported in terms of CSO or CTB, it is difficult to derive an expression relating the CTB or CSO to the rate equation description of lasers.

Narrow band applications, such as personal cellular communications (PCS) systems and radar systems, occupy a narrow range of frequencies. Narrow band applications are performance limited by third order intermodulation distortion and noise. From a systems performance point of view, the most important quantity that describes a laser device for narrow band applications is the spurious free dynamic range (SFDR), or the range of input powers over which the signal is unaffected by either noise or distortion.

2.3.1 Distortion

Distortion occurs when a signal has multiple channels which mix with each other because of nonlinearities in the device. The nonlinearities appear in two different ways. Static distortion occurs when the nonlinearities of the light-versus current (LI) curve are present. These nonlinearities are caused by spatial hole burning, gain compression, finite carrier transport times, optical feedback, and leakage currents. Dynamic distortion occurs when the intrinsic nonlinearities of the device cause different frequency components to mix together through the interaction of photons and electrons in the laser cavity. As a result of these nonlinearities in the device, it is possible for multiple frequencies from separate channels to mix with each other and produce new distortion signals.[19] These new signals appear at frequencies that are at the sum or difference of two or more channels, as shown in Figure 2.7.[29]

We initially restrict ourselves to the case of only two channels and determine the distortion that will arise from their interference. When carried out experimentally, such a test is referred to as a two-tone test. There are two types of distortion that we are interested in for SCM communications: harmonic distortion and intermodulation distortion.

Harmonic distortion is the production of an integer harmonic of one or more of the input signals.[29] Thus, if we have two input signals, f_1 and f_2 , the harmonic distortion products are $2f_1$, $3f_1$, $4f_1, \dots, nf_1$, where n is the order of the distortion and is determined by the number of input signals that are combined into the new output signal; $2f_1$ would be called second order harmonic distortion. In narrow band applications, the frequency range is often sufficiently limited such that taking twice the lowest frequency in the range would be well beyond the range allocated for the application; thus harmonic distortion is less of a consideration for narrow band applications. Harmonic distortion is important, however,

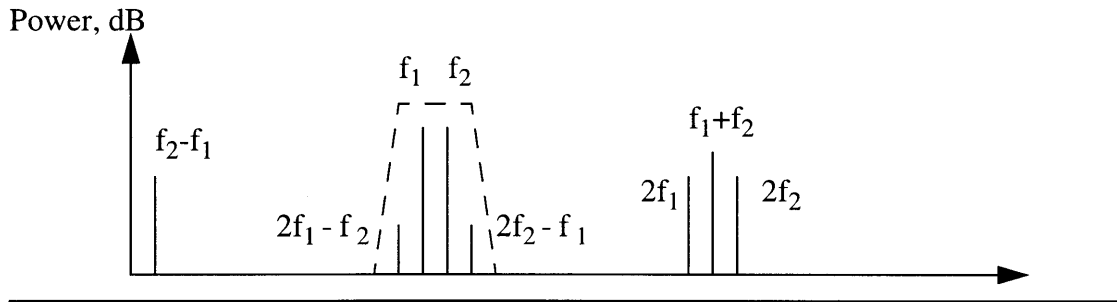


Figure 2.7: Distortion products for broad-band and narrow-band applications. The dashed line shows that for narrow-band, performance will be limited by IMD3.

for broad band applications such as cable television where the frequency range is wide enough that twice the lowest frequency would still be well within the range for the application. Thus, we would have to consider second order harmonics ($2f_1$, $2f_2$), and higher order harmonic products if necessary.

Intermodulation distortion is the production of new signals at frequencies that are the linear combinations of the input frequencies. If we have two input signals f_1 and f_2 , then the second order intermodulation distortion products are $f_1 + f_2$, $f_1 - f_2$, $f_2 - f_1$ and the third order intermodulation products are $2f_1 + f_2$, $f_1 + 2f_2$, $2f_1 - f_2$, $2f_2 - f_1$. For an arbitrary intermodulation product, $mf_1 + nf_2$, $m+n$ gives the order of the product. The $(m+n)^{\text{th}}$ order product scales with the modulation depth to that same power. If f_1 and f_2 are relatively closely spaced, then the second order intermodulation distortion products will all be either higher or lower in frequency than the two fundamental signals. This will not cause a problem for narrow band applications, where the second order products will fall well outside the frequency range, but this can be a problem for broad band applications. Third order intermodulation distortion (IMD3) products, however, can fall in the range of both narrow band and broad band applications. In particular, the products $2f_1 - f_2$ and $2f_2 - f_1$ will fall very close to f_1 and f_2 and may significantly affect the output signal. Thus, reduction and elimination of IMD3 is of great interest for both broad band and narrow band applications. Because IMD3 involves three frequencies, it scales cubically with the modulation depth.

Distortion formalism

The matrix method used in section 2.2 to derive the modulation response can be generalized to obtain the higher order distortion products:

$$\begin{bmatrix} N_{ab} \\ S_{ab} \end{bmatrix} = \frac{H(\omega)}{\omega_R^2} \begin{bmatrix} M_{22} + j\omega & -M_{12} \\ -M_{21} & M_{11} + j\omega \end{bmatrix} \begin{bmatrix} Q_{abN} \\ Q_{abS} \end{bmatrix}. \quad (2.27)$$

where the matrix elements are the same as before, and the \mathbf{Q} matrix on the right hand side represents the driving terms for all of the different distortion products. To obtain the driving terms, begin with a small signal sinusoidal current input with two frequency components, and assume a form for the carrier density:

$$\begin{aligned} I(t) &= I_0 + I_1 e^{\pm j\omega_1 t} + I_2 e^{\pm j\omega_2 t}, \\ N(t) &= N_0 + N_{11} e^{j\omega_1 t} + N_{12} e^{j\omega_2 t} + N_{21} e^{j2\omega_1 t} + N_{22} e^{j2\omega_2 t} + \\ &\quad N_{23} e^{j(\omega_1 + \omega_2)t} + N_{24} e^{j(\omega_2 - \omega_1)t} + N_{31} e^{j(2\omega_2 - \omega_1)t}. \end{aligned} \quad (2.28)$$

The photon density will have a same form as the carrier density. After plugging the photon and carrier density terms into the rate equation, we group the terms with the same frequency dependence together. Table 2.1 summarizes the driving terms for the distortion products that are relevant for calculation of the third order intermodulation distortion. We note that the second order intermodulation distortion and harmonic distortion are contributing factors to the third order intermodulation distortion. The IMD3 is reported relative to the fundamental in terms of dB:

$$IMD3 = \left| \frac{S_{31}}{S_{11}} \right|. \quad (2.29)$$

In the last section of this chapter, we use this distortion formulation to simulate IMD3.

Table 2.1: Driving terms for higher order distortion products

Order	Term	Driving terms
First (a=1)	Modulation response	$Q_{1bN} = \frac{\eta_i I_1}{qV}$ $Q_{1bS} = 0$
Second (a=2)	General term	$Q_{2bN} = -2(B + CN_0)\xi - v_g \Psi$ $Q_{2bS} = \Gamma\beta B\xi + \Gamma v_g \Psi$ <p>where Ψ, ξ given below</p>
	Harmonic distortion	$\xi = N_{1b}^2, \quad b=1,2$ $\Psi = \{a_n S_{1b} N_{1b} - a_p S_{1b}^2\}$
	Intermod. distortion	$\xi = 2N_{11}N_{12}, \quad b=4.$ $\Psi = \{a_n S_{14} N_{14} - 2a_p S_{11} S_{12}\}$
Third (a=3)	Intermod. distortion	$Q_{3bN} = -2(B + CN_0)(2N_{24}N_{11} + N_{21}N_{12}) - 3CN_{11}^2 N_{12} - v_g \chi$ $Q_{3bS} = 2\Gamma\beta B(2N_{24}N_{11} + N_{21}N_{12}) + \Gamma v_g \chi$ $\chi = a_n(2S_{24}N_{11} + 2S_{11}N_{24} + S_{21}N_{12} + S_{12}N_{21}) - 2a_p(2S_{24}S_{11} + S_{21}S_{12})$
		$N_{11} = H(j\omega_1) \left[(M_{22} + j\omega_1) \frac{\eta_i I_1}{qV} \right]$ $N_{12} = H(j\omega_2) \left[(M_{22} + j\omega_2) \frac{\eta_i I_2}{qV} \right]$ $N_{21} = H(j2\omega_1) [(M_{22} + j2\omega_1)Q_{21N} + M_{12}Q_{21S}]$ $N_{24} = H(j(\omega_1 - \omega_2)) [(M_{22} + j(\omega_1 - \omega_2))Q_{24N} + M_{12}Q_{24S}]$ $S_{11} = -H(j\omega_1) M_{21} \frac{\eta_i I_1}{qV}$ $S_{12} = -H(j\omega_2) M_{21} \frac{\eta_i I_2}{qV}$ $S_{21} = H(j2\omega_1) [-M_{21}Q_{21N} + (M_{11} + j2\omega_1)Q_{21S}]$ $S_{24} = H(j(\omega_1 + \omega_2)) [-M_{21}Q_{24N} + (M_{11} + j(\omega_1 - \omega_2))Q_{24S}]$

2.3.2 Noise

Random fluctuations in the carrier and photon population cause the laser to exhibit intensity noise and phase noise. The phase noise determines the linewidth of the laser. The intensity noise is characterized by the relative intensity noise (RIN), which is defined as the ratio of the variance of the noise divided by the average output power squared, $P_0^2 / \langle \delta P(t)^2 \rangle$. In practice, the RIN is reported in decibels, or $10 \log_{10}$ RIN.

The RIN can be derived using the Langevin functions, which represent stochastic processes with zero averages. The Langevin noise functions appear in the rate equations in the place of the driving terms in equation (2.27). Even in the absence of a modulation current, the noise fluctuations drive the system and result in a frequency dependent response. The RIN is found by expressing the output power spectral density in terms of the solutions to the rate equations driven by the Langevin functions and in terms of the second order noise correlations.[9] The frequency dependence of the RIN is found to be:

$$\frac{RIN}{\Delta f} = \frac{2h\nu}{P_0} \left[\frac{a_1 + a_2 \omega^2}{\omega_R^4} |H(\omega)|^2 + 1 \right] \quad (2.30)$$

where Δf is the filter bandwidth of the measurement apparatus and $H(\omega)$ is the same frequency response from equation (2.22). The second term in the brackets of equation (2.30) inherent quantum noise, or shot noise, of the laser. This is only applies in the case where the emitted fields are in a perfectly coherent state. In the limit of high powers the photon statistics inside a laser cavity do, in fact, converge toward a Poisson distribution, which is indicative of a coherent state.[9] Thus, for low powers or for a shot noise limited current source at high powers, equation (2.30) can be approximated by

$$\frac{RIN}{\Delta f} = 16\pi(\Delta v)_{ST} \frac{1/\tau_{\Delta N}^2 + \omega^2}{\omega_R^4} |H(\omega)|^2 + \frac{2h\nu}{P_0}, \quad (2.31)$$

above threshold. The frequency dependence of the RIN is dominated by the term $\omega^2 |H(\omega)|^2$, and thus the peak of the RIN occurs at ω_R , rather than at $\omega_P = \omega_R \sqrt{1 - \frac{1}{2} \left(\frac{\gamma}{\omega_R} \right)^2}$, as given by equation (2.26) for the modulation response.[9] Thus, the resonance frequency can be extracted more simply by looking at the RIN versus frequency plot than from the modulation response. At the resonance frequency, the RIN is given by:

$$\frac{RIN}{\Delta f} = \frac{16\pi(\Delta v)_{ST}}{\gamma^2}, \quad \omega = \omega_R. \quad (2.32)$$

When the RIN is plotted as a function of the current bias, the noise will be very high near the laser threshold, and will fall rapidly. At a certain point, the RIN will start to rise again as it becomes dominated by the shot noise limited term. Thus, the noise will always have a certain bias point above threshold at which the noise is minimized.

2.3.3 Spurious Free Dynamic Range

Until now all of the performance limitations that we have presented are inherent characteristics of the laser device and are independent of the system in which the laser will be used. We will now look at a quantity that is dependent upon the bandwidth of the system that for which the laser is being used. This quantity is the spurious free dynamic range (SFDR) and it measures the range of powers from where the desired signal becomes discernable above the noise floor to where the intermodulation distortion begins to give spurious signals that may be confused as a desired signal.[5]

For system designers, the SFDR is an extremely important property of a communications system as it allows them to directly predict how a device will perform in their applications. Dynamic range requirements for cable television systems are under $120 \text{ dB Hz}^{2/3}$

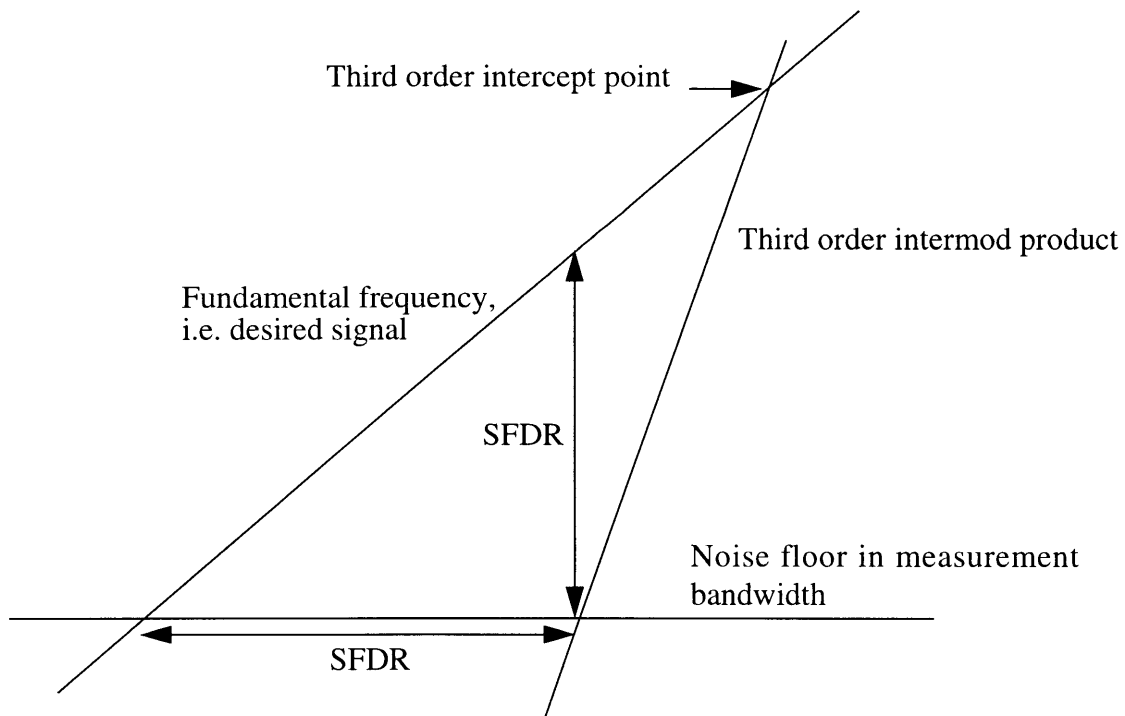


Figure 2.8: Definitions for Spurious free dynamic range (SFDR).

and are often achieved using predistortion circuits and external modulators.[10] Typical requirements for radar systems fall between 105 to 125 dB Hz^{2/3}. Typical SFDR requirements for analog personal communications systems using a single microcell base station are in the neighborhood of 90 dB Hz^{2/3}. [12] This corresponds to a blocked call probability (i.e., the probability that the call does not have enough power at the receiving end) of 0.5% using a single antenna micro cell. Using multiple micro cells, this same blocked call probability can easily be achieved with less than 80 dB Hz^{2/3}. Cutrer et al [12] find through simulations that increasing the SFDR by as little as 4 dB can double the number of phone calls that can be transmitted by a link while ensuring a certain call blocking probability.

The SFDR is determined by the fundamental signal and by the strength of the distortion signal. For narrow band applications, the distortion term of interest is the third order intermodulation product. As explained in section 2.3.1, the IMD3 products will fall inside the desired frequency range, but the other distortion products will fall outside of the range of interest.

For a given system, the system will require a certain bandwidth to transmit its own signal. This bandwidth is called the measurement bandwidth. The noise floor of the system is dependent upon the measurement bandwidth. The plot used to determine the SFDR is shown in Figure 2.8 on a log-log scale. The horizontal axis is input power and the vertical scale is output power. Changing the input power corresponds to changing the modulation depth of the input signal. The line corresponding to the fundamental signal has a slope of 1 because the fundamental scales linearly with the modulation depth. The line corresponding to IMD3 has a slope of three because the third order intermod distortion scales cubically with the modulation depth. The SFDR is measured from the point where the

IMD3 crosses the noise floor to the point where the fundamental crosses the noise floor; the SFDR is measured in units of dB Hz^{2/3}.

The noise floor N_B in the measured bandwidth B , is given by:

$$N_B = N_{\text{meas}} - G_{\text{LNA}} + 10 \log (B). \quad (2.33)$$

where G_{LNA} is the gain of the low noise amplifier. The measurement bandwidth is typically on the order of 1 MHz.

The thermal noise (N_T) at room temperature sets the measurement noise floor at a 1 Hz measurement bandwidth: $N_T = 10 \log(k_B T)$, where k_B is Boltzmann's constant, 1.38×10^{-23} J/K. For room temperature, $T=300$ K, the thermal noise is $N_T = 174$ dBm. The excess noise measures the amount of noise out of the device above the thermal noise floor. The excess noise is given by the formula:

$$N_{\text{ex}} = N_{\text{meas}} - G_{\text{LNA}} + N_T. \quad (2.34)$$

The noise figure is the ratio of the input SNR to the output SNR. It was calculated by the formula:

$$F = (N_{\text{meas}} - G_{\text{LNA}} + N_T) - G_{\text{link}} = N_{\text{ex}} - G_{\text{link}}. \quad (2.35)$$

Maximizing SFDR

There are three quantities that determine the SFDR: the power in the fundamental, the noise floor, and the power in the intermodulation distortion term. Increasing the fundamental by 1 dB will have the effect of increasing the SFDR also by 1 dB. The power in the fundamental frequency component (f_1, f_2) can be found from equations 2.10 and 2.21. Thus, increasing the ratio of mirror loss to total loss, the differential gain, or the injection efficiency (η_i) are all ways that the power in the fundamental could be increased.

Decreasing the noise floor by 1 dB will have the effect of increasing the SFDR by $2/3$ dB because of the slope of the IMD3. The noise floor is determined by the application bandwidth, the measured noise and the amplifier gain in the system, as seen in equation 2.33. The application bandwidth is determined by system requirements, and the amplifier gain is determined by the system itself. The measured noise is determined by the current bias of the laser. Directly above threshold, the noise will be large but will be decreasing. Far above threshold, the measured noise is typically shot noise limited. Thus, it might be possible to increase the SFDR by properly choosing the bias current such that the laser is biased close to the noise minimum..

Decreasing the IMD3 by 1 dB will cause the SFDR to increase by only $1/3$ dB, because of the slope of the IMD3. Furthermore, it is difficult to determine what parameters will affect the IMD3 just by looking at the equations. In the last section of this chapter, we will explore how the distortion changes as different system parameters are changed. By examining this, we can start to understand how we may be able to increase the SFDR by decreasing the distortion. In chapter 4, we will examine the measurements of distortion from the Fujitsu DFB, and we will find that there is also a minimum in the distortion, which we believe is caused by a cancellation effect between the gain compression and the spatial hole burning. This effect will also provide a way to optimize the SFDR.

2.4 Parameter extraction

The laser device is an AR/HR coated Fujitsu DFB laser designed to minimize second order intermodulation distortion for analog applications. The structure is described in section 3.3. The dimensions of the device were obtained from [37] and are given in Figure 3.9. From these dimensions, we determined that the confinement factor, Γ , is approximately 0.110. The facet reflectivities are 1% and 80%.

For the Fujitsu DFB laser diode, we have plotted the LI curves at six temperatures in Figure 2.11 and the threshold currents vs. temperature in Figure 2.12. Using Figure 2.11, we determine that the laser slope efficiency is 0.197 W/A at $T=24^\circ\text{C}$. The characteristic temperature, T_0 was found to be 45°K , which is reasonable for InP in-plane lasers. Coldren and Corzine [9] report that the normal range for T_0 in an InGaAsP/InP laser is between $50\text{-}100^\circ\text{K}$, so that the value found for this Fujitsu laser is reasonably close to accepted values.

The RIN versus frequency for the Fujitsu DFB laser is plotted in Figure 2.9, for a range of different bias currents. The temperature is fixed at $T=24^\circ\text{C}$. Figure 2.10 shows the RIN peak level and the frequency of the peak versus bias current. Using the frequency of the peak versus bias current along with equation 2.23, we can fit a curve with a square root dependence on the threshold bias current and extract the product of the extra factors. The group index of refraction for InGaAsP devices is usually between 3.6-4, thus we can get an estimate of the group velocity with 10% error. We estimate the volume of the photon confining region of the laser to be $(Ldw)/\Gamma = 3.54 \times 10^{-10} \text{ cm}^3$. The threshold current at 24°C is approximately 13.2 mA. Using these values, we find the product of the injection efficiency and the differential gain is approximately $\eta_i a = 8 \times 10^{-16}$ with a 10% uncertainty. The injection efficiency for InGaAsP devices with quantum wells is typically

in the neighborhood of 0.6 because not all of the carriers make it in to the wells and stay there. For an InGaAsP bulk device, the injection efficiency can be higher because a larger proportion of the carriers stay within the active region. We choose our injection efficiency to be $\eta_i = 0.95$ and our differential gain to be $a = 7.5 \times 10^{-16}$. The constraint extracted from the RIN measurements indicates that we should have picked a differential gain of at least 8×10^{-16} , but we have chosen a differential gain slightly lower than this because published values for differential gain in bulk active materials tend to be below 2×10^{-16} . [35]

Using LaserMatrix, we ran several different simulations with structure parameters similar to the Fujitsu DFB ones. The optical spectrum was reproduced best by a structure that had a π phase shift upon reflection on the left and 0° phase shift on the right. In the simulations, approximately 90% of the light left the structure on the AR coated side. Based on this, we chose F_1 equal to 0.90.

Another parameter associated with the measurements is the detector efficiency. The detector efficiency describes what percentage of the laser output power is being collected by the detector. We found that the collector efficiency was approximately 0.45. This was accomplished by matching the slope of the calculated LI curves with the slope of the measured LI curves for the Fujitsu laser.

In Chapter 3, we present a short algorithm used for extracting parameters from DFB lasers. Using this algorithm, we were able to verify that the length of the device was 300 μm and we were able to determine that the device had a coupling coefficient of $\kappa L = 0.75 \pm 0.05$. The complete list of extracted parameter values is given in Table 2.2.

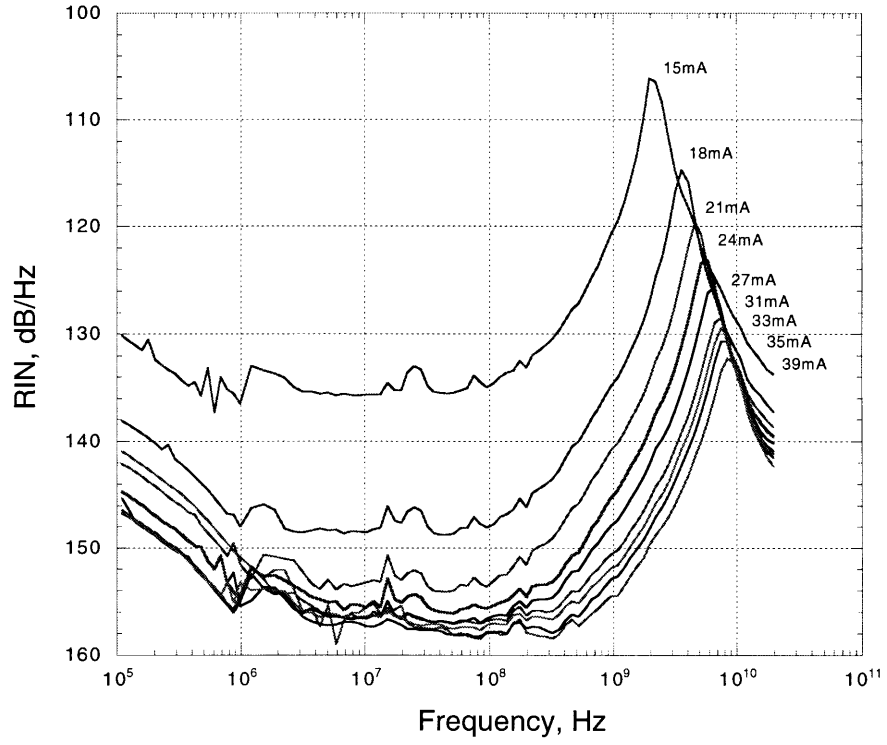


Figure 2.9: RIN vs frequency for Fujitsu laser. The peaks correspond to ω_R .

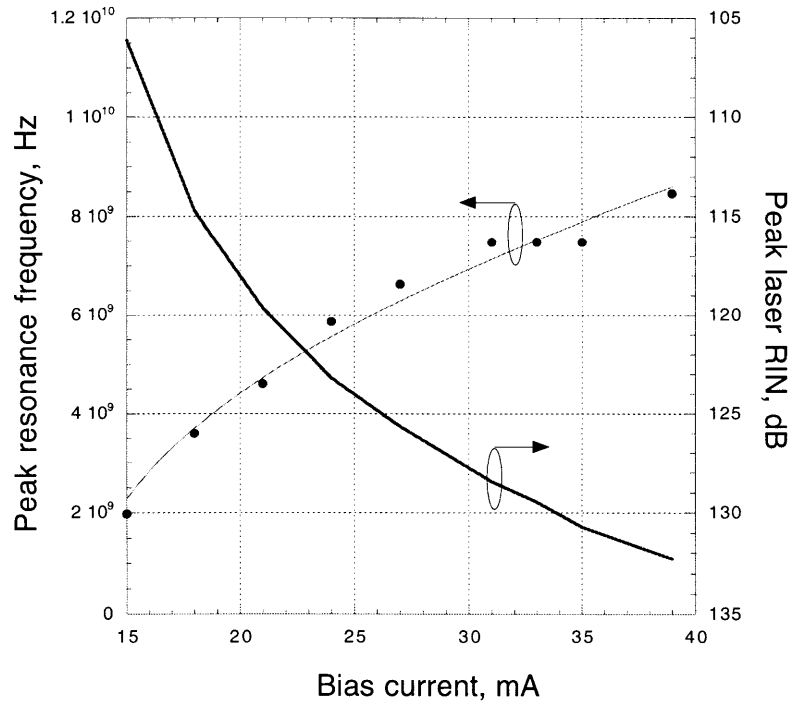


Figure 2.10: Peak resonance and peak laser RIN vs bias current, for Fujitsu laser.

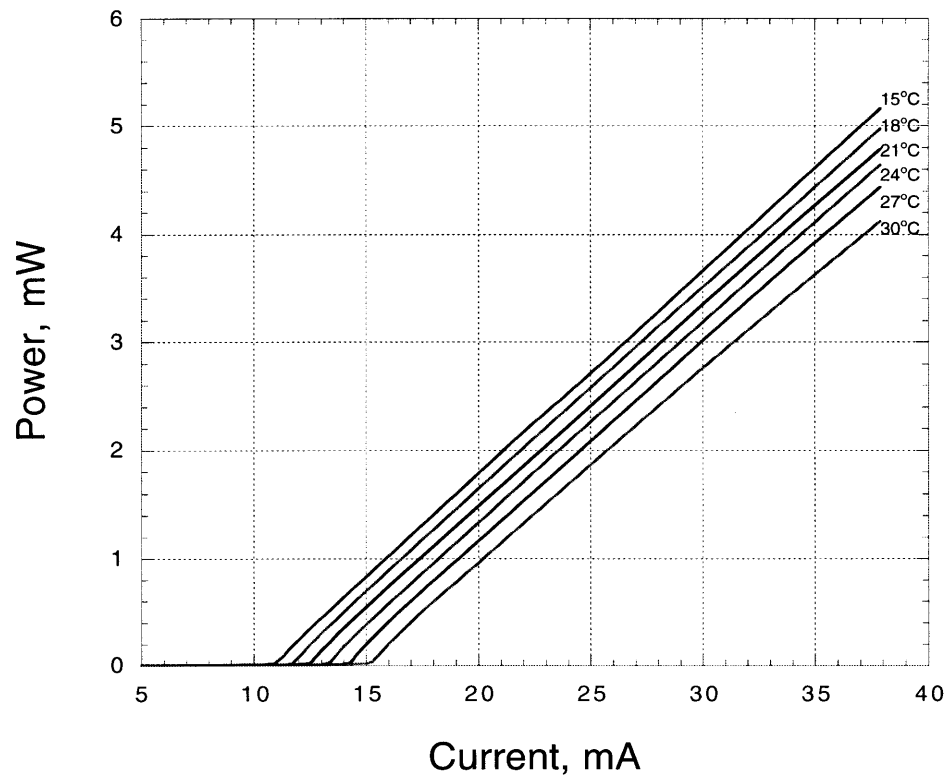


Figure 2.11: LI curve for Fujitsu laser, measured at different temperatures.

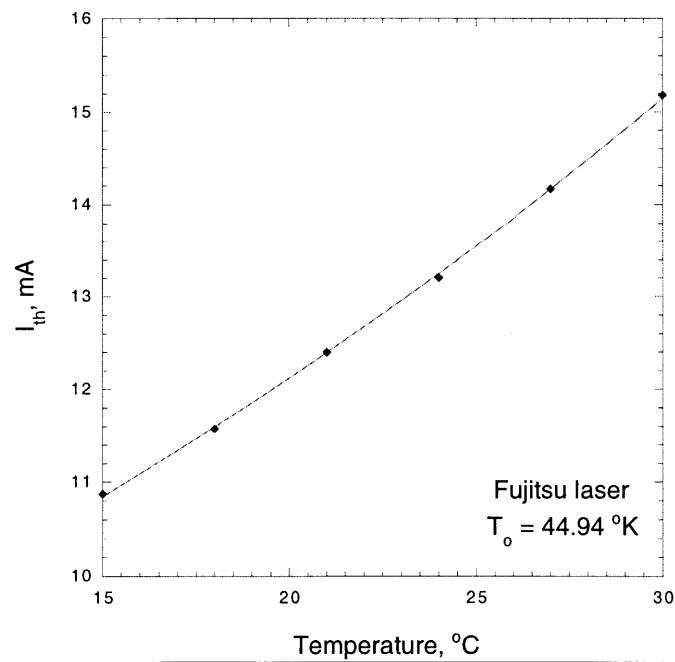


Figure 2.12: Threshold current versus temperature.

Table 2.2: Parameters used in simulations

			range
Bragg wavelength	λ_B	1.308 μm	
cavity length	L	300 μm	
active cavity thickness	d	0.13 μm	
active cavity width	w	1 μm	
cavity width	w_c	7 μm	
confinement factor	Γ	0.110	
group index of refraction	n_g	4.0	3.5-4.0
effective index of refraction	n_{eff}	3.285	
waveguide loss	α_{in}	40 cm^{-1}	
estimated mirror and distributed loss	α	40 cm^{-1}	
differential gain	a_N	$7.5 \times 10^{-16} \text{ cm}^2$	
carrier density at transparency	N_{tr}	$2 \times 10^{18} \text{ cm}^{-3}$	
nonradiative recombination coefficient	A	0	
bimolecular recombination coefficient	B	$1 \times 10^{-10} \text{ cm}^3/\text{s}$	
Auger recombination coefficient	C	$4 \times 10^{-29} \text{ cm}^6/\text{s}$	
gain compression factor	ϵ	$3 \times 10^{-17} \text{ cm}^3$	
linewidth enhancement factor	α	4	
injection efficiency	η_i	0.95	0.8-1
spontaneous emission factor	β_{sp}	0.869×10^{-4}	10^{-4}
back facet reflectivity	R_r	80%	
front facet reflectivity	R_f	1%	
fractional power out of front facet	F_1	0.90	
collector efficiency	n_2	0.45	

2.5 Distortion simulation

In this section, we will use the discussions from sections 2.1, 2.2, and 2.3, along with the parameters determined in the previous section to simulate the Fujitsu DFB device. We also use some parameters that are derived in Chapter 3 to help here. We wish to explore the parameter space to see the effects of changing the different parameters in small ways. These simulations are performed in MATLAB. The final extracted parameters used in the simulations are listed in Table 2.2.

Using the distortion formalism from section 2.3.1, we simulated third order intermodulation. Figure 2.13 shows the third order intermodulation distortion versus frequency, for four different values of the gain compression coefficient, ϵ . With $\epsilon=0$ (no gain compression), the IMD3 is increasing from low frequencies at 20dB per decade. The DC

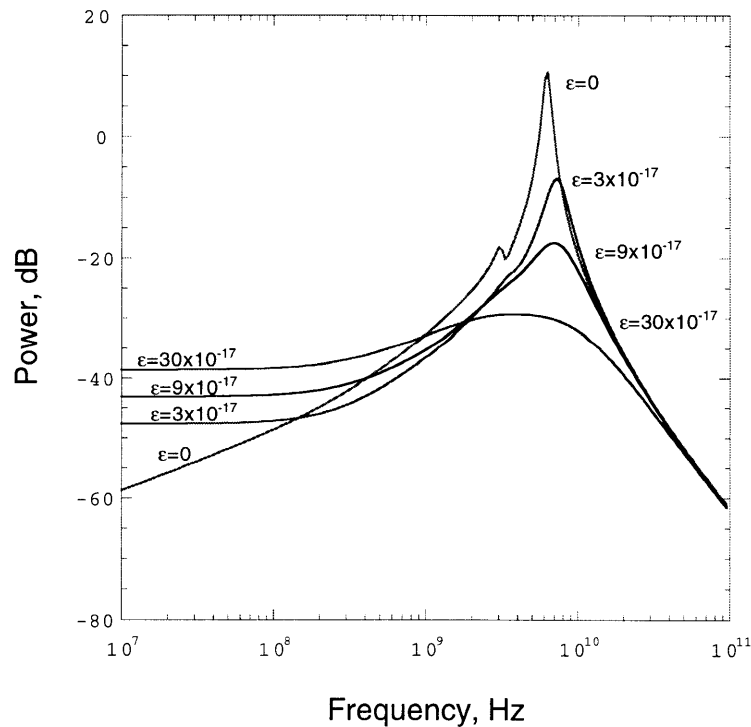


Figure 2.13: Third order intermodulation distortion (IMD3), for four different values of gain compression.

intermodulation distortion is very low because the only nonlinearity is due to the intrinsic resonance response which is negligible far from the relaxation oscillation frequency. The distortion peaks above 0 dB near 6 GHz, indicating that the distortion is actually higher than the modulation response. There is a bump in the curve around 3 GHz, which represents a resonance in the device at half the resonance frequency. After reaching its peak value, the distortion falls off at 40dB per decade.

With gain compression $\epsilon=3 \times 10^{-17}$, Figure 2.13 shows that the distortion has a constant value at DC which is higher than the case for no gain compression. This can be understood because there is now an additional nonlinearity at low frequencies and at DC. The distortion again falls off at 40dB per decade after reaching its peak value. As the gain compression is increased (larger ϵ) the DC value of the distortion increases while the peak in the distortion and the bump at 3 GHz both decrease due to increased damping. The LI curves for different values of gain compression are given in Figure 2.3.

Figure 2.14 shows the third order intermodulation distortion for a range of bias currents for (a) no gain compression and (b) with a gain compression coefficient $\epsilon=3 \times 10^{-17}$. We have used a modulation amplitude $i=1\text{mA}$. In the simulations, the LI curve has a threshold of 12.7 mA. These figures correspond to the Figures 2.6 for the modulation response.

Figure 2.15(a) shows the results of simulations for the intermodulation distortion relative to the carrier versus bias current at 100 MHz, with a fixed amplitude modulation. The results are shown for no gain compression ($\epsilon=0$) and for typical gain compression ($\epsilon=3 \times 10^{-17}$). The distortion without gain compression is lower because the only nonlinearity is due to the intrinsic relaxation resonance frequency. With gain compression, the distortion increases. In both cases, as the current bias increases, the distortion decreases because the modulation depth ($m = \frac{I_1}{(I_{bias} - I_{th})}$) decreases. As was mentioned in sec-

tion 2.3.1, the scales as the modulation depth cubed. In Figure 2.15(b), we have divided the results of the distortion simulation by the modulation depth cubed. By doing this, we remove the effect of decreasing distortion which is due solely to decreasing modulation depth. In the case of no gain compression, we obtain an almost flat line which indicates that there are almost no other nonlinearities present at this low frequency (100 MHz is much less than the relaxation oscillation frequency; see RIN peaks, Figure 2.9). For the case of gain compression ($\epsilon=3 \times 10^{-17}$), the rescaled plot is increasing which indicates that there is a nonlinear effect which increases with the current bias, and hence with the optical power. This nonlinear effect is due to the gain compression.

It should be pointed out that these simulations are performed assuming a small signal modulation. Thus the simulations are not expected to be accurate near threshold, where the modulation may actually be forcing the laser below threshold.

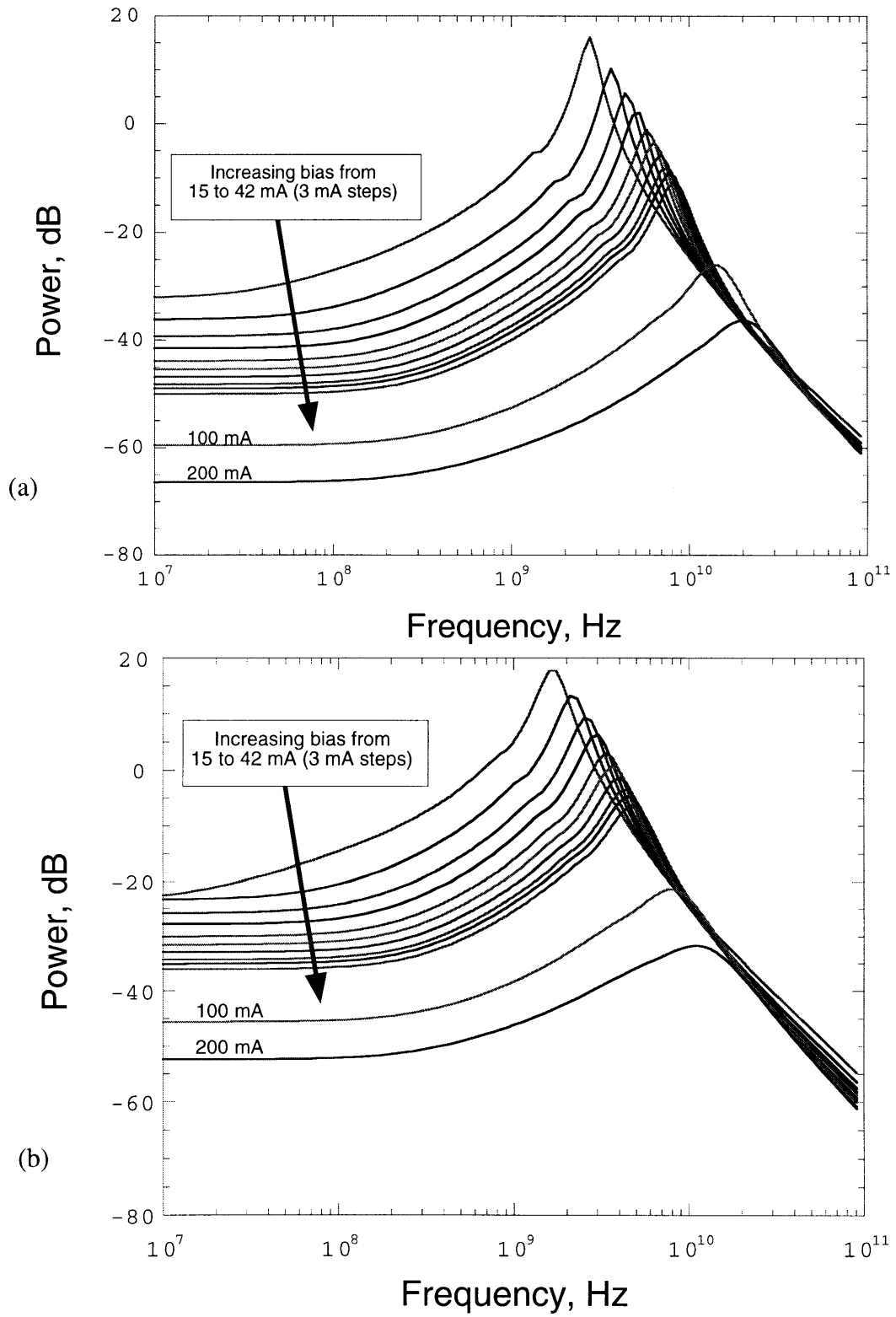


Figure 2.14: Distortion for (a) no gain compression, (b) $\epsilon=3 \times 10^{-17}$.

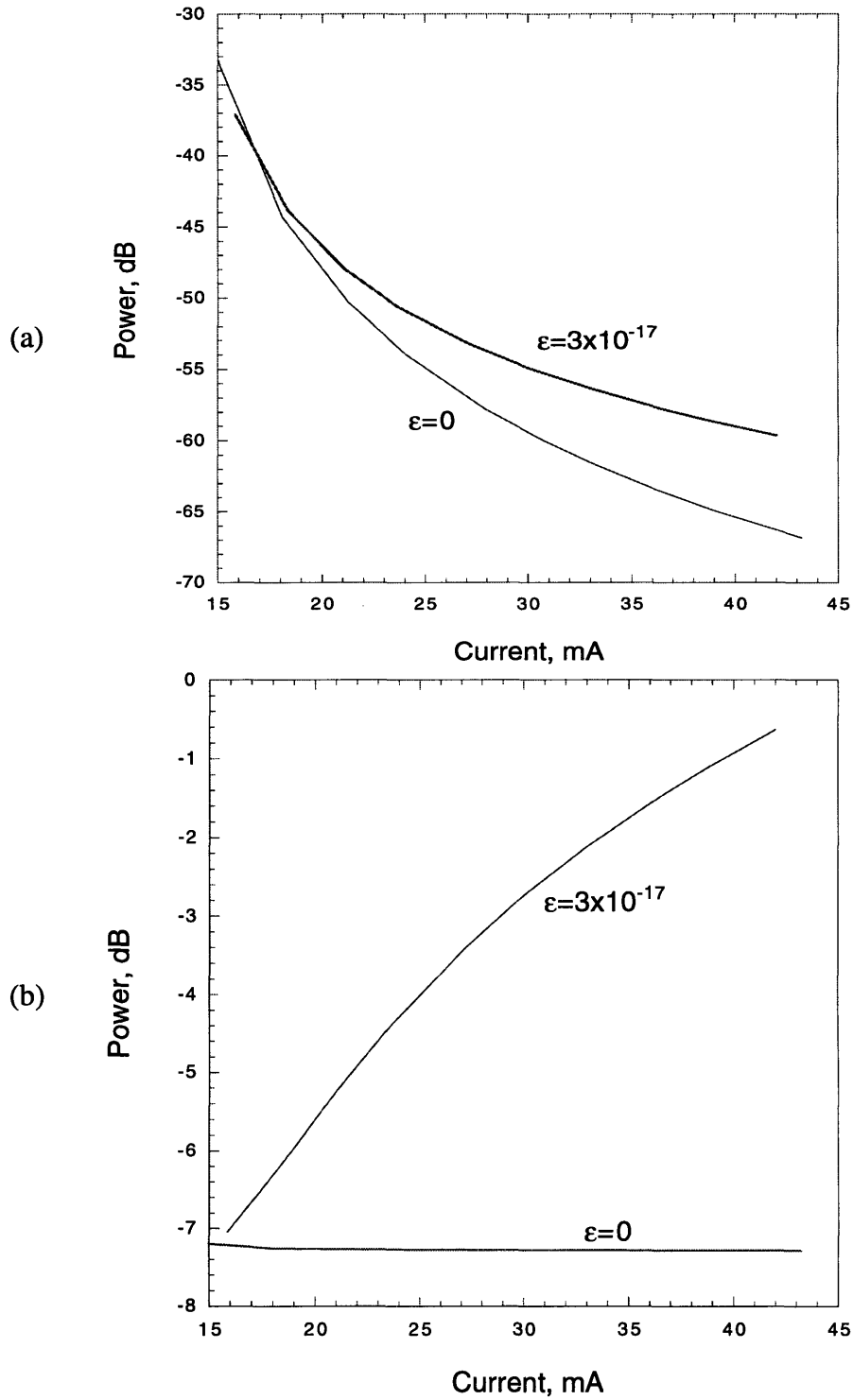


Figure 2.15: (a) IMD3 relative to carrier vs. bias for two gain compression values. (b) IMD3 relative to carrier divided by the modulation depth cubed.

2.6 Summary

In this section we introduced the steady state and dynamic analysis of the laser rate equations. We briefly discussed some of the internal physics that leads to lasing, as well as some of the internal causes of static nonlinearities, such as gain compression and spatial hole burning. We introduced the concept of distortion and spurious free dynamic range. We explained that for a narrow band analog optical communications system, performance will be limited by the third order intermodulation distortion and by the noise at the application bandwidth.

We extracted some of the key parameters for the Fujitsu DFB laser and used these parameters in simulations of steady state, modulation, and distortion characteristics. Our simulations included gain compression but not spatial hole burning. We plotted the simulated distortion divided by the modulation depth cubed versus bias current with and without gain compression. At 100 MHz, the case without gain compression is almost flat, whereas the case with gain compression is rising due to the increasing nonlinearity. Therefore, we have an idea of what to expect from our measurements if these are the only two nonlinearities present in the structure. In the next chapter, we will introduce the distributed feedback (DFB) laser structure and examine how this structure affects the mode spectrum. Many of the results that we obtained in this section will still be valid for the DFB laser.

Chapter 3

DISTRIBUTED FEEDBACK (DFB) LASERS

In the previous section we derived the steady state, modulation, noise, and distortion characteristics for a Fabry-Perot laser. We started with a Fabry-Perot laser because the analysis is relatively simple. Under direct modulation, however, Fabry-Perot lasers become multimode, even for significant steady state mode suppression ratios.[2] The Fabry-Perot laser, therefore, is not a good choice for fiber optic communications. For transmission in communications systems, we turn to the distributed feedback (DFB) laser. A distributed feedback laser is a device that uses a periodic variation of either index or gain to couple forward going light waves to backwards going waves. The coupling of the light in the two directions serves the same purpose as the cleaved facets in Fabry-Perot lasers; effectively, the coupling is a distributed reflector. Only those frequencies which properly couple in the forward and backwards going directions via the periodic grating will experience significant feedback to reach lasing. The periodicity of the grating determines which frequencies of light experience strong enough reflections to reach threshold. Thus, the DFB only yields stimulated emission of cavity modes that satisfy a certain condition for the periodic index or gain variation. It turns out that in the most typical case, lasing only occurs for one of two modes on either side of a stopband in the frequency. This is a significant improvement over the Fabry-Perot laser. Further improvements in the design make it possible to break the degeneracy and select one of the two lasing modes.

In this section, we will derive several key results for a DFB laser using coupled mode analysis. We will briefly discuss the relevant type of DFB structure used in this work. We will then discuss results obtained using LaserMatrix, a laser simulation software package. In the final section, we will explain a procedure used to extract key design parameters from a prepackaged DFB laser, and we will present the parameters for the laser that we used in subsequent high speed measurements.

3.1 Differences between Fabry-Perot and DFB lasers

The approach used in Chapter 2 for the Fabry-Perot lasers can be partially extended to DFB lasers. It turns out that the modulation, distortion, and noise analyses carried out in Chapter 2 are still relevant for DFB lasers. There are some important differences, however. Because the mechanism of reflection is different for DFB lasers, the effective reflectivities become wavelength dependent, the threshold lasing condition changes, the light output spectrum is different, and the mode selectivities are different. Using coupled mode analysis, it is possible to show that DFB lasers will lase at one of two frequencies that occurs on either side of a stop band in the frequency. The most accurate analysis of a DFB laser requires the use of a spatially dependent rate equation analysis. This later approach is somewhat more complicated and is not carried out here.

The periodic structure of the DFB makes it more susceptible to some effects and less sensitive to other effects. Spatial hole burning is now of great interest because the photon and carrier distributions are determined by the choice of coupling coefficients. DFB lasers are also very sensitive to the phase at the cleaved facet relative to the grating. In the steady state, the threshold for lasing in a DFB can vary from device to device as a result of

sensitivity to phase shifts at the facets.[2] Differential quantum efficiency can be different for the light emitted from each of the facets, also due to phase shifts at facets.[2] On the other hand, DFB lasers are less sensitive to temperature shifts. As temperature changes, the gain spectrum will shift; the lasing mode will shift slightly due to a change in the index of refraction, but the mode will not jump as temperature changes as in the case of Fabry-Perot lasers because lasing can only occur at the edges of the stopband.

3.2 DFB Theory

3.2.1 Coupled wave theory

The analysis presented here is based on the coupled wave theory developed by Kogelnik and Shank in the early 70's. In this derivation, we only consider an index coupled DFB laser. The references [2, 9, 22, 25] cover the case of a gain coupled DFB laser, which is not considered here. The model starts with the scalar wave equation for the electric field along the length of the device, from $z=-L/2$ to $z=L/2$:

$$\frac{d^2 E}{dz^2} + k^2 E = 0 \quad (3.1)$$

where E is the complex amplitude of the field of angular frequency ω . It is assumed that the frequency, refractive index and gain constants are all independent of x and y , but there is a spatial modulation of the refractive index $n(z)$ of the form:

$$n(z) = n + \Delta n \cos(2\beta_0 z) \quad (3.2)$$

where $\beta_0 \equiv \frac{n\omega_0}{c} = \frac{2\pi n}{\lambda_B}$ and λ_B is the wavelength of the light in freespace and ω_0 is the Bragg frequency. The Bragg wavelength, λ_B , is related to the grating periodicity, Λ , by:

$$\lambda_B = \frac{2n\Lambda}{m}, \quad m=1, 2, \dots \quad (3.3)$$

In analyzing the structure, we make the assumption that the index variation is much less than the refractive index. These assumptions allow us to write the k constant from 3.1 in terms of β , β_0 , Δn , and α :

$$k^2 = \beta^2 + 2j\alpha\beta + 4\kappa\beta \cos(2\beta_0 z), \quad (3.4)$$

where $\beta = n\omega/c$. The coupling constant $\kappa = \frac{\pi\Delta n}{\lambda_0}$ is a measure of the strength of backward Bragg scattering and thus a measure of the feedback.

In the coupled mode theory analysis, we only consider the two modes that are in the vicinity of the Bragg frequency; other modes are not in phase and are not of significant amplitude. The two modes around the Bragg frequency describe the forward and backward propagating waves:

$$E(z) = R(z)e^{-j\beta_0 z} + S(z)e^{j\beta_0 z}, \quad (3.5)$$

where $R(z)$ and $S(z)$ are slowly varying according to the assumptions that we made, so that $\frac{\partial^2 R}{\partial z^2}$, $\frac{\partial^2 S}{\partial z^2}$ are negligible. Plugging 3.5 into the scalar wave equation 3.1 and rearranging, we obtain:

$$\begin{aligned} -\frac{dR}{dz} + (\alpha - j\delta)R(z) &= j\kappa S(z) \\ \frac{dS}{dz} + (\alpha - j\delta)S(z) &= j\kappa R(z) \end{aligned} \quad (3.6)$$

where $\delta \equiv (\beta^2 - \beta_0^2)/2\beta_0 \approx \beta - \beta_0 = n(\omega - \omega_0)/c$ is the normalized frequency parameter and is a measure of the detuning of the oscillation frequency ω away from the Bragg frequency ω_0 .

We would now like to solve equations (3.2) and (3.6) subject to the boundary condition that the wave amplitudes are zero at the edges, i.e $R(z=-L/2)=S(z=L/2)=0$, where L is the length of the structure. Taking into account the symmetry of the device, we get:

$$\begin{aligned} R(z) &= \sinh\gamma\left(z + \frac{1}{2}L\right) \\ S(z) &= \pm\sinh\gamma\left(z - \frac{1}{2}L\right), \end{aligned} \quad (3.7)$$

where the complex eigenvalue γ obeys the dispersion relation:

$$\gamma^2 = \kappa^2 + (\alpha - j\delta)^2. \quad (3.8)$$

The plus and the minus in the expression for $S(z)$ correspond to symmetric and anti-symmetric solutions. If we now plug these solutions into equation 3.6, and add the two resulting equations, we get an expression for the coupling constant in terms of γ :

$$\kappa = \pm j\gamma / (\sinh\gamma L). \quad (3.9)$$

We can also get an expression for the threshold gain and detuning parameter in terms of γ :

$$\alpha L - j\delta L = \pm j\kappa L \cosh\gamma L = \gamma L \coth\gamma L. \quad (3.10)$$

Equations 3.9 and 3.10 are transcendental equations which are difficult to solve exactly; however, we can plot both sides of the equation to get good approximations. Figure 3.1, taken from Kogelnik and Shank [22], shows the result of plotting both sides of the equation using the modal threshold gain, αL , and the mode detuning, δL , for the case of an index-coupled DFB laser. Only positive values are shown as the plot is symmetric for the mode detuning. The first three modes are shown. In the limit of $\kappa L = 0$, the modes

approach the Fabry-Perot modes. This limit corresponds to the case of no index coupling. As κL is increased, the modes move further away from the Fabry-Perot modes. In Appendix A, this effect is explained in an alternate way using perturbation theory. The dashed horizontal lines in Figure 3.1 indicate three different values of the coupling coefficient $\kappa L = \pi \Delta n L / \lambda_0$. The point on the vertical axis where these dashed lines cross the solid lines for each of the modes indicates the threshold gain for each mode. In each case, the mode at the edge of the stopband has the lowest threshold gain. This threshold modal gain is the gain required to overcome both the distributed feedback losses and the facet losses. We obtain a threshold material gain by plugging α into equation 2.5:

$$g_{th} = (\alpha + \alpha_i) / \Gamma. \quad (3.11)$$

Thus, we can approximate the frequency dependent loss of a DFB laser by using a mirror loss coefficient in the standard Fabry-Perot rate equation analysis. This mirror loss includes the losses from the facets as well as frequency dependent losses due to the grating coupling. This approach is only applicable for the mode at the lasing frequency; other frequencies would experience a different threshold gain (and hence would have a different mirror loss coefficient).

Figure 3.2 shows the wavelength of the different modes versus the coupling coefficient. This figure was calculated by LaserMatrix using the coupled mode theory. As the coupling coefficient is increased, the stopband width increases, and the separation of the modes immediately adjacent to the stopband decreases. The condition $\kappa L=0$ corresponds to a standard Fabry-Perot laser with no grating.

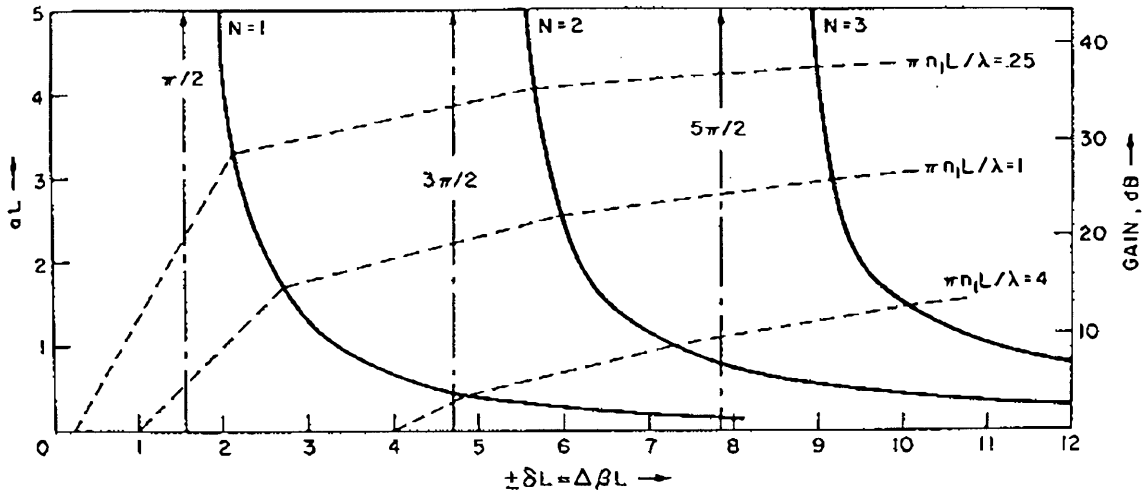


Figure 3.1: Modal threshold gain (αL) versus mode detuning (δL) for index coupled AR/AR coated DFB laser. From Kogelnik and Shank.[22]

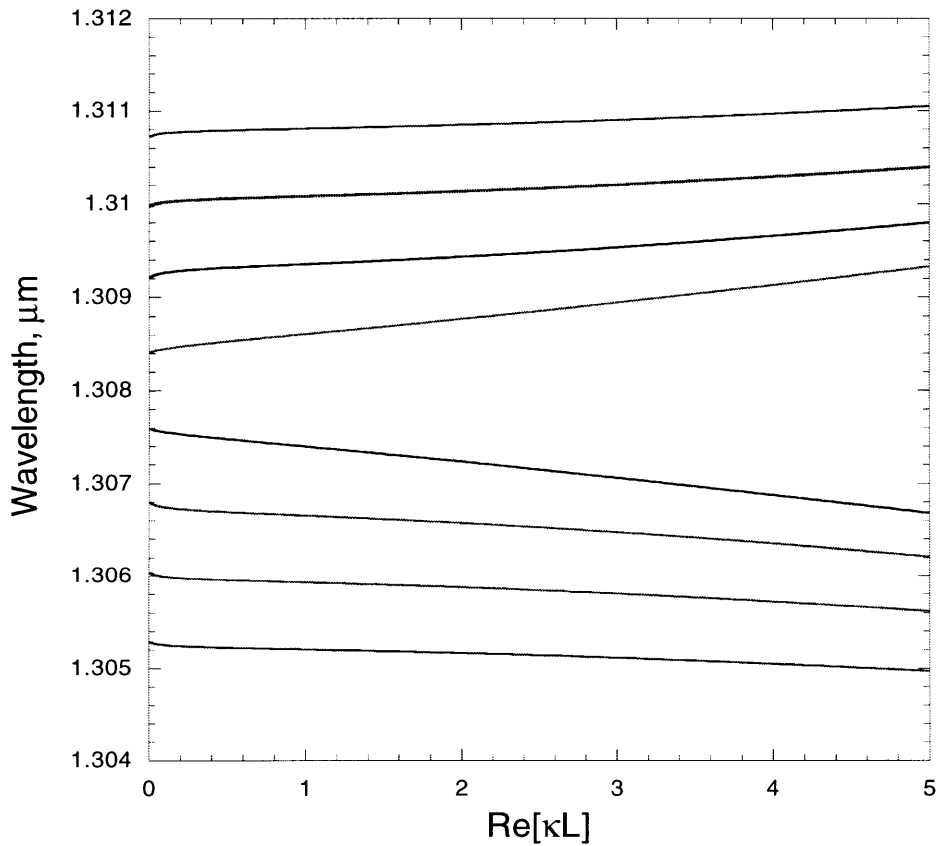


Figure 3.2: The plot of wavelength vs $\text{Re}[\kappa L]$ shows the widening of the stop band as κL is increased. The modes near the stop band are also pushed away as κL increases. Simulation performed using LaserMatrix (Royal Institute of Technology, Sweden).

3.2.2 Spatial hole burning in DFB lasers

We briefly analyzed spatial hole burning for a Fabry-Perot laser in Chapter 2. The shape of the photon density distribution does not change very much as the structure changes, although the magnitude of the photon density can be reduced by reducing the current or changing the facet reflectivities. For a DFB, on the other hand, the spatial distribution of the photon density distribution is determined by the facet reflectivities and the coupling constant, as described in the previous section. Thus, the location and extent of spatial hole burning are also determined by the coupling constant. This complicates the analysis of DFB lasers because the spatial hole burning changes the carrier density distribution, which leads to a change in the refractive index distribution, which changes the frequency-selective feedback losses, which in turn affects the mode selection. Spatial hole burning can thus lead to a shift in the selected mode, and may even change on which side of the stop band (explained in section 3.2.5) the lasing mode appears.

In addition to affecting the mode selection, spatial hole burning can lead to a decrease in the side mode suppression ratio for a DFB, and can ultimately lead to multimode operation if spatial hole burning is significant enough. Phillips et al.[30] report spatially resolved measurements of amplitude and phase of the carrier density response to an RF drive current for two lasers. They calculate the carrier lifetime in these lasers. One of their lasers clearly shows the effects of spatial hole burning leading to an decreased side mode suppression ratio and eventual dynamic multimode operation. The photon density is initially concentrated in the center of the device. As the bias current is raised, the carrier density in the center decreases and the the density at the edges increases. This shape of carrier density distribution causes another mode to reach threshold, as is confirmed by their measurements.

Spatial hole burning may lead to a sublinear or superlinear LI curve, depending upon the phase of the spatial hole burning. In the case of a sublinear LI curve, the spatial hole burning will add to the nonlinearity of the LI curve caused by gain compression. The extra nonlinearity will also increase harmonic and intermodulation distortions in the low frequency regime. In the case of a superlinear LI curve, the spatial hole burning may actually cancel with the gain compression and decrease the nonlinearity of the LI curve, and thus decrease the distortion. The phase of the spatial hole burning is dependent upon the facet reflectivities, the value of κL , and other factors.[8] In chapter 4, we report what we believe is the first measurement of a cancellation effect between spatial hole burning and gain compression leading to a decrease in the distortion. Okuda *et al.* [27] reported a similar type of cancellation mechanism between the spatial hole burning and the relaxation oscillation, which also leads to lower intermodulation distortion. This may indicate that having a small amount of spatial hole burning present can actually reduce distortion by cancelling other nonlinearities.

Spatial hole burning is typically calculated using a spatially dependent rate equation analysis where the laser structure is broken up into smaller segments, and the photon density is calculated for each segment. The models used in our simulation do not include the spatial dependence and cannot be used to accurately determine spatial hole burning. We can still get an idea of the effect of spatial hole burning using LaserMatrix, which does use a spatially dependent rate equation analysis. Figures 3.3 and 3.4 illustrate the effects of spatial hole burning for two different cases using LaserMatrix simulations. Figure 3.3 shows the case of an AR/AR coated DFB laser with a large coupling coefficient ($\kappa L=3.0$) at 5 times threshold current. For a large coupling coefficient, the photon density will be concentrated in the center of the device for an AR/AR coated device. The large photon density (a) leads to a depletion of carriers in the center region of the laser (b). The

decreased carrier density leads to a decreased photon gain (c) and an increased refractive index (d).

Figure 3.4 shows the same plot for an improved design laser. In this case, the coupling coefficients and facet reflectivities have been chosen in such a way to maximize light output and minimize the effect of spatial hole burning. The laser is AR (5%) coated on one facet and HR (85%) coated on the other facet. The coupling coefficient is chosen to be 0.8 (the reason for this choice will be explained in the next section). The photon density is concentrated on one facet of the laser, indicating that most of the light comes out from that side then from the other side. Here again, we see that the large photon density leads to a depleted carrier density, which leads to a decreased photon gain and increased refractive index.

Figure 3.3: (a) Photon density, (b) carrier density, (c) photon gain, (d) and refractive index in an AR/AR coated DFB laser with a large coupling coefficient ($\kappa L=3.0$) at 5 times threshold current. Simulations performed using LaserMatrix (Royal Institute of Technology, Sweden). Simulations clearly indicate the effect of spatial hole burning on the carrier density, leading to a decrease in the gain and an increase in the refractive index. All of the distributions are symmetric due to the symmetry of the structure.

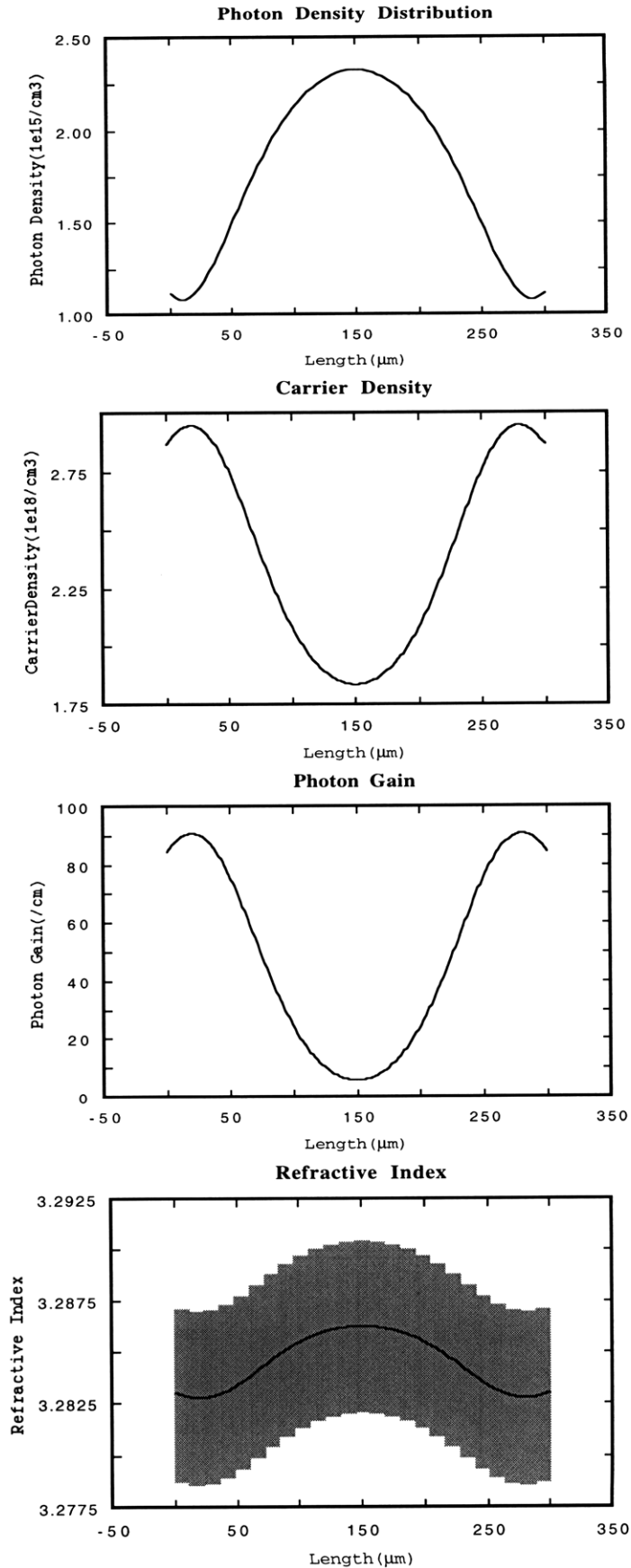
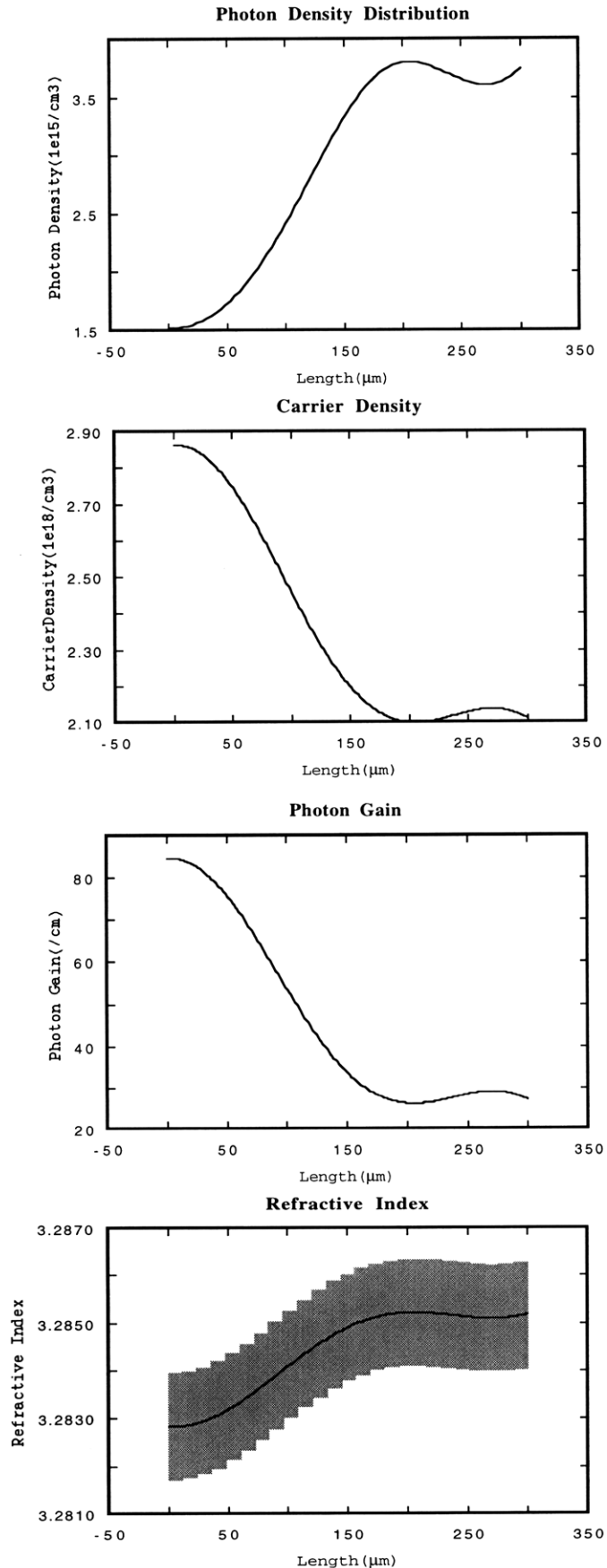


Figure 3.4: (a) Photon density, (b) carrier density, (c) photon gain, (d) and refractive index in HR/AR coated DFB laser with $\kappa L=0.8$ at 5 times threshold current. Simulations performed using LaserMatrix (Royal Institute of Technology, Sweden). Simulations clearly indicate the effect of spatial hole burning on the carrier density, leading to a decrease in the gain and an increase in the refractive index. Due to the asymmetry of the facet coatings, the distributions are all shifted. If, however, the length were doubled while the κ remains constant, the distributions would again resemble those in Figure Figure 3.3:. The distributions in these figures roughly correspond to what is expected for the Fujitsu laser.



3.2.3 Minimizing spatial hole burning effects in DFB lasers

As described in the previous section, in general spatial hole burning leads to undesirable effects in DFB lasers. By properly choosing the coupling coefficient, we can minimize the effect of spatial hole burning. We can use coupled mode analysis to determine what the spatial distribution of light in the distributed feedback structure will be. In analyzing the photon distribution, we would like to balance two different requirements for the laser: we would like to design our laser so that we are getting as much light out of it as possible; however, if the distribution of photons turns out to be too high at certain locations in the structure, we may end up reducing performance by inducing spatial hole burning. The spatial mode profile is determined by multiplying the complex conjugate pairs of the forward and backward going waves: $I(z) = RR^* + SS^*$, or

$$I(z) = \sinh^2\gamma\left(z + \frac{L}{2}\right) + \sinh^2\gamma\left(z - \frac{L}{2}\right) \quad (3.12)$$

To find the value of κL at which the intensity distribution is flat, we assume that when the intensity at the edges of the laser equals the intensity at the center of the laser we will get an even carrier distribution throughout the structure. For the case of a device that is coated on both facets with anti-reflection material, we solve $I(z=0) = I(z=L/2)$ and find a transcendental equation that yields the solution $\kappa L \approx 1.64$. For this value of κL , we can expect a flat carrier distribution. For κL values smaller than this, the distribution will be stronger near the edges of the device, while for larger values of κL , the distribution will be stronger in the center of the device. Choosing κL equal to approximately 1.64 will flatten the distribution out and will thus result in decreased spatial hole burning. Figures 3.3(a) and shows the photon density distribution for an AR/AR coated DFB device ($\kappa L=3.0$) modeled using LaserMatrix.

For the case of a device where one side is anti-reflection (AR) coated and the other side is high-reflection (HR) coated, the above discussion gets slightly modified. The HR coating is a mirror which will reflect most of the light incident upon it. Most of the photons will have to travel twice the length of the device to escape: once up the device and once back down the device after being reflected off of the HR surface. The effective length and effective κL are both therefore doubled, allowing us to use a device that is half as long or has a κL that is half the desired value to achieve the same result. In this case, to achieve a flat distribution, we would use a κL around 0.8. Figure 3.4(b) shows the photon density distribution for an AR/HR coated DFB device with $\kappa L=0.7$.

There is an interesting consequence of choosing a κL that flattens out the photon and carrier distribution. We noted in previous sections that it is difficult to incorporate spatial hole burning into the rate equations because spatial hole burning is dependent up on the photon distribution, which is usually not uniform in most Fabry-Perot and DFB structures. In the case of a DFB laser with uniform photon distribution near threshold as described above, however, the simple rate equation analysis used in Chapter 2 turns out to be applicable because the carrier and photon densities do not vary in the longitudinal direction. Hence, for this one case the rate equations give a relatively accurate picture of what is going on within the laser device.

To summarize, using coupled mode theory, we find that the spatial mode profile is dependent upon the product of the length of the structure and the coupling coefficient, κ . A flat carrier distribution is desired to minimize the spatial hole burning. The ideal κL for an AR/AR coated device is approximately 1.7, and for an AR/HR coated device the ideal κL is approximately 0.8.

3.2.4 Mode selection

The standard DFB laser with symmetric facet phases and facet reflectivities will yield a structure with two degenerate lasing modes. This degeneracy can be removed through the arbitrary phases that arise from cleaving the DFB laser. The degeneracy can also be removed by asymmetrically coating each facet with antireflecting material or high reflecting material. The degeneracy can also be removed by introducing other perturbations into the structure, such as $\lambda/4$ -shifted DFBs, chirped gratings, corrugation pitch-modulated structures, S-bent waveguides, etc. One highly successful approach is the $\lambda/4$ phase shifted DFB. By introducing a quarter wave shift into the center of the DFB laser, a new mode is introduced which lases exactly in the middle of the stop band at the Bragg wavelength.

There is also the possibility of mode selection due to spatial hole burning. Chen has found that for the case of large coupling ($kL > 1.64$) in a DFB laser, spatial hole burning will have a superlinear characteristic at low bias values slightly above threshold. Gain compression, on the other hand, always has a sublinear characteristic leading to roll over of the LI curve. This effect occurs at large biases far above threshold. At some intermediate bias level, the two effects will cancel out, leading to cancellation or reduction of nonlinearities. This effect will occur when the lasing mode is on the long wavelength side of the stop band. This can be understood by looking at Figure 3.5. This figure is similar to Figure 3.3(d), except that three horizontal lines have been drawn to represent three possible lasing modes at the long wavelength side of the stopband (top line) and at the short wavelength side of the stopband. The long wavelength mode does not see significant reflection and thus will not reach threshold first. The medium wavelength mode will fall into the stopband as the stopband shifts due to the spatial-hole-burning-induced refractive index shift. Following the discussion of section 3.2.5, the medium wavelength mode will

experience a very large reflection and will decay exponentially rather than propagating. The short wavelength mode will see significant reflection and will thus be able to reach threshold, but the loss will not be as severe as for the middle wavelength mode. Thus, the short wavelength mode will be selected. This is the case for an AR/AR coated DFB laser with large coupling coefficient.

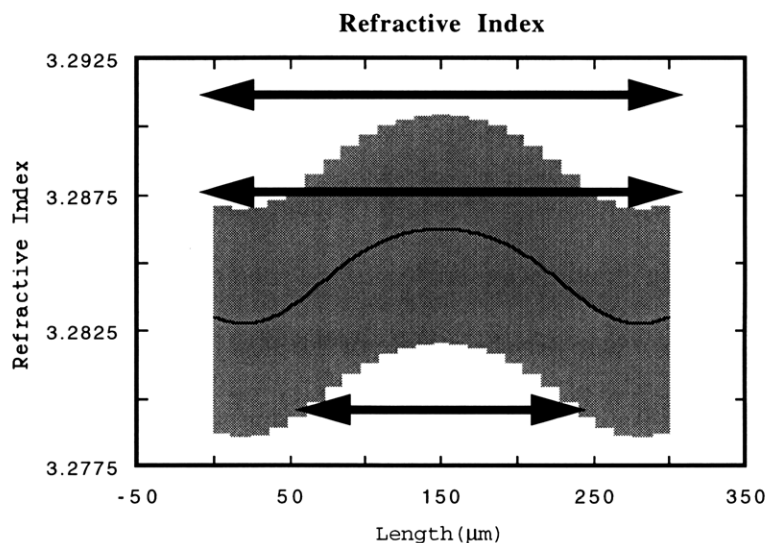


Figure 3.5: Refractive index shape due to spatial hole burning in AR/AR DFB laser.

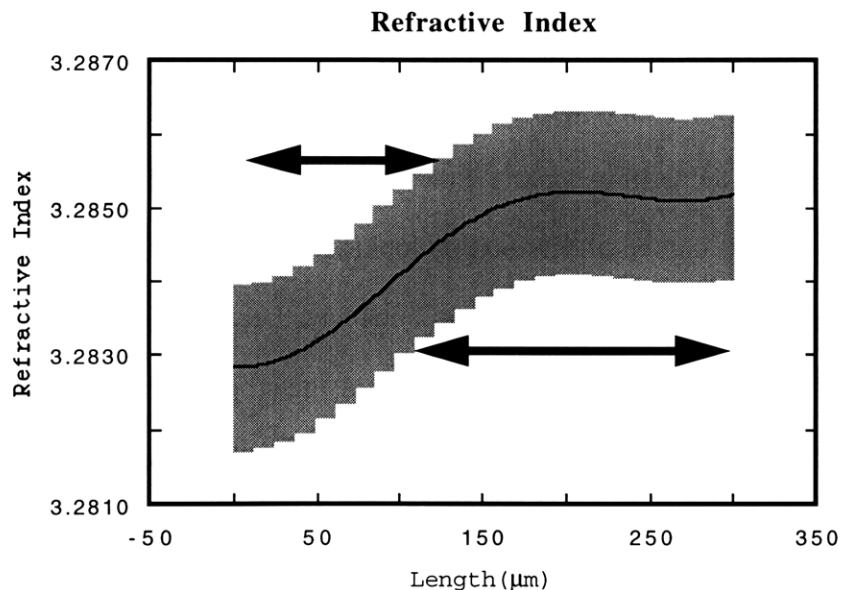


Figure 3.6: Refractive index due to spatial hole burning in AR/HR coated DFB laser.

The same type of analysis holds in the case of structures with high coupling coefficients and asymmetrically coated facets. For the case of an AR/HR coated device, the refractive index will have a profile as shown in Figure 3.6. The high reflective (HR) side is on the left and the antireflection (AR) coated side is on the right. The stopband will have a shape similar to the one seen in Figure 3.6. A mode propagating on the long wavelength side (above) of the stopband will see a strong reflection from the stopband on the right and the HR coated side on the left. A mode propagating on the short wavelength side (below) of the stopband will see a strong reflection from the stopband on the left, but very little reflection from the AR coated side on the right. Thus, the long wavelength mode will likely reach threshold first.

For small coupling ($\kappa L < 1.64$) as is the case in the Fujitsu DFB laser, the situation becomes more complicated. It is believed that for κL above 1.64, spatial hole burning is the dominant effect leading to mode selection, as described above. For κL below 1.64, this effect is less dominant. The effect of the refractive index change on the mode profile may be a factor in determining which mode reaches threshold first.[6]

3.2.5 Mode Spectrum

In section 2.1.3, we stated that the output spectrum of a Fabry-Perot laser below threshold will have multiple modes with a spacing given by equation 2.12. We would now like to determine what the output spectrum of a DFB laser will look like. This will give us greater understanding of the coupling mechanism in distributed structures, and will also aid us in extracting parameters from a DFB laser.

Figure 3.1 shows that there is no mode at the Bragg frequency ($\delta L=0$) in an AR/AR coated index coupled DFB laser. We can use coupled mode theory to understand why this is the case. As seen in Figure 3.7, there is a maximum in the reflection spectrum at the Bragg frequency for the case of an index coupled DFB, so most of the light is reflected out of the laser and very little light is transmitted. This reflection spectrum actually occurs at

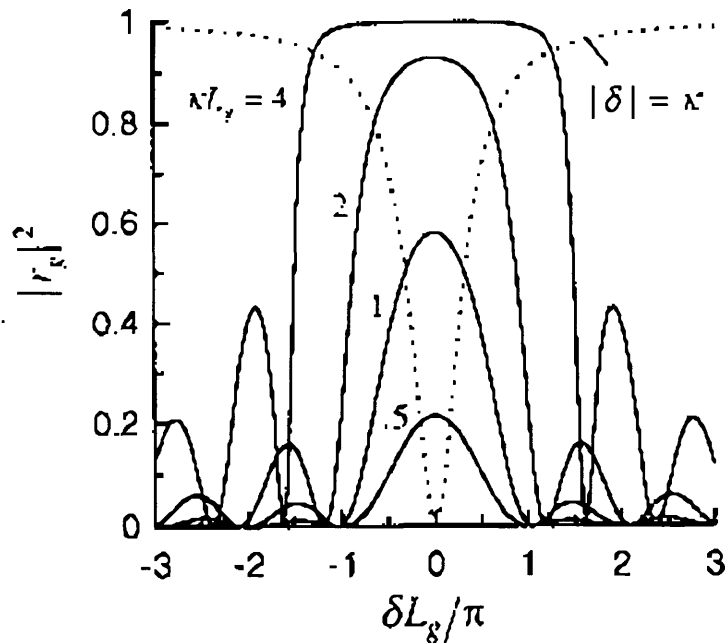


Figure 3.7: Reflection spectrum of index coated AR/AR coated DFB laser. Plot shows power reflection spectrum of grating for four different κL values versus modal detuning, δL .

multiples of the Bragg frequency, but only one such window falls under the gain spectrum for the laser (see Figure 3.8). There are no modes within a region around the Bragg frequency known as the stopband. This stopband has a width of 2κ in terms of ω/c in the case of an infinitely long DFB and in the low gain limit. Waves whose frequencies are within the stopband have a propagation eigenvalue γ which is purely real. Plugging a purely real γ into equation 3.7 leads to decaying exponential waves. [2] Thus, the structure cannot support propagation of waves within the stopband. Waves outside the stopband are travelling waves, and they show little interaction with the periodic structure.[25] Therefore, we expect that in the vicinity of the Bragg frequency at the edge of the stopband, there will be two modes. In practice, only one of these two modes will typically reach threshold, as was discussed in the previous section. Further away from the Bragg frequency, we expect to see modes that resemble the Fabry-Perot modes.

The frequency at which the structure lases is not exactly at the null in the reflection spectrum. At these nulls, all of the light propagates through the structure and very little of it couples backwards. Light at this frequency is subject to gain on only one trip through the structure. Thus at the null point in the reflection spectrum, there is no mode. The actual mode must be slightly away from the null, as very little light can be transmitted through the structure at this frequency.

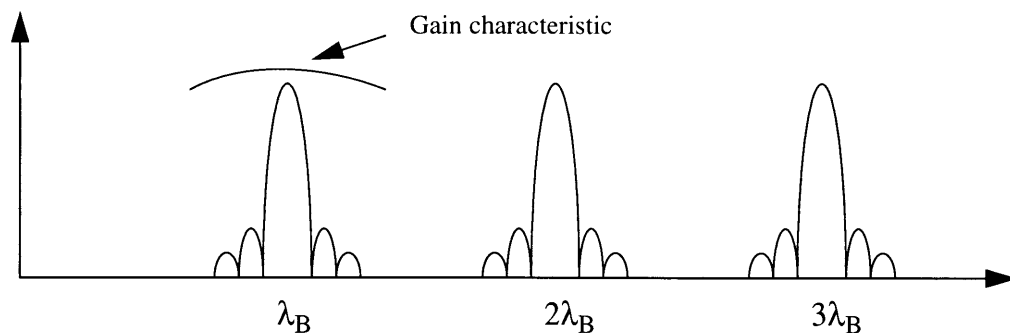


Figure 3.8: Multiple wavelength windows occur, but only one falls under the gain curve. Based on [25].

The above discussion assumes an infinitely long periodic structure. The arguments hold approximately for the case of a finitely long structure, although the results must be modified slightly. Nonetheless, they can be used to gain insight into what is occurring within the structure. Figure 3.10 shows measured optical spectra taken below, at, and above threshold for the Fujitsu DFB laser; we see general agreement with our predictions.

We noted in section 2.1.3 that the spacing of the Fabry-Perot modes is proportional to the length of the device. This means that if we measure this spacing between modes on an optical spectrum, we should be able to determine the length of the device. As shown in Figure 3.2, however, modes closer to the Bragg frequency are shifted further from the Fabry-Perot modes. Therefore, we must be careful to measure the spacing of the modes far from the Bragg frequency, otherwise the estimate will not be correct. This idea will be used in Section 3.4 when we are examining parameter extraction from optical spectra.

3.3 Fujitsu DFB Structure

The DFB structure used in this work (model number FLD 130F3ACH-AL/180) was a flat surface buried heterostructure (FBH) device optimized for second order distortion in analog CATV systems. The device is AR/HR coated with reflectivities of approximately 1% / 80%, and has active region dimensions: $L=300\ \mu\text{m}$, $d=0.13\ \mu\text{m}$, $w=1\ \mu\text{m}$. Figure 3.9 shows a schematic of the laser. The extracted coupling coefficient for the structure is $\kappa L = 0.75 \pm 0.05$ (see next section). Yonetani *et al.* [37] report a slope efficiency is 0.3 mW/mA. They also report that a mesa width of $7\ \mu\text{m}$ optimizes the second order intermodulation distortion, and they give composite second order (CSO) and composite triple beat (CTB) for several different conditions.

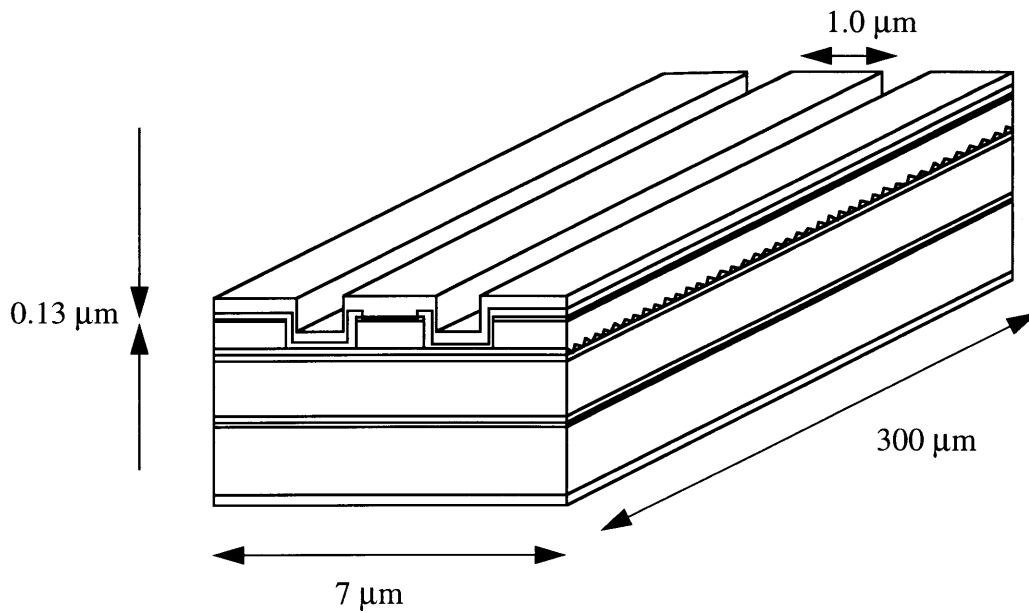


Figure 3.9: Schematic of Fujitsu DFB laser. Drawing courtesy Jianyao Chen.

3.4 Parameter extraction

We measured device characteristics of several DFB laser devices. These devices were prepackaged, and in many cases the specific device parameters were not available to us. We therefore had to extract the parameters from the spontaneous emission spectra that were gathered. In this section, we summarize the parameter extraction procedure.

Often when a company sells a prepackaged laser, they do not include exact device specifications or parameters for the laser, thus making it difficult to simulate the devices performance. Thus, it is sometimes necessary to extract the parameters from measurable characteristics, such as power output or optical spectrum measurements. Parameter extraction requires a very good understanding of DFB laser theory. Although there are programs available (e.g. Laparex from University of Tokyo EE Department) that can

extract various important DFB parameters from an optical spectrum, it is instructive to carry out some of the parameter extraction by hand. These parameters can be verified by comparing with the output of the various programs, and can then be simulated with other software tools that allow for device simulation (e.g. Laser Matrix, from the Royal Institute of Technology, Sweden).

3.4.1 Extraction procedure

We start with the spontaneous emission spectrum, similar to the one in Figure 3.1. From section 2.1.3, we know that by measuring $\Delta\lambda_{FP}$, the spacing of the Fabry-Perot modes far away from the center DFB band stop, we can get a very good estimate of the length of the device. We go as far away from the band stop as possible because perturbation theory tells us that the shift of the Fabry-Perot modes away from their positions for a Fabry-Perot laser will be smaller the farther we get away from the band stop. The length of the device is then given by $L = \frac{\lambda^2}{2n_g\Delta\lambda_{FP}}$ for a given group index of refraction. Even if the group index of refraction is unknown, it is possible to guess an index for a given material system that is within 10% of the actual refractive index.

Next, we would like to extract the coupling coefficient κ . Although in previous sections we explained how the coupling coefficient can be estimated from the width of the bandstop, we find that this estimation is not satisfactory for parameter extraction as the coupling coefficient is dependent upon the length of the device itself. The approximation that the width of the bandstop is equal to 2κ holds in the low gain, infinite length DFB laser case. We can still get an estimate of the coupling coefficient, however, using a look up table approach. Using LaserMatrix, a set of design curves were created for a range of coupling coefficients at a set current level and for a given set of facet reflectivities. For

each κL value, LaserMatrix generated the width of the bandstop versus the length of the device (see Figure 3.10). Now, given the length of the device as calculated above, and the width of the bandstop, $\Delta\lambda_{BS}$, we can read off the value of κL that corresponds to the design curve falling closest to the measured values.

More sophisticated parameter extraction algorithms are available that may yield more accurate results; however, each algorithm may start with a different set of given measurements and arrive at a different set of end results. [24, 32, 33]

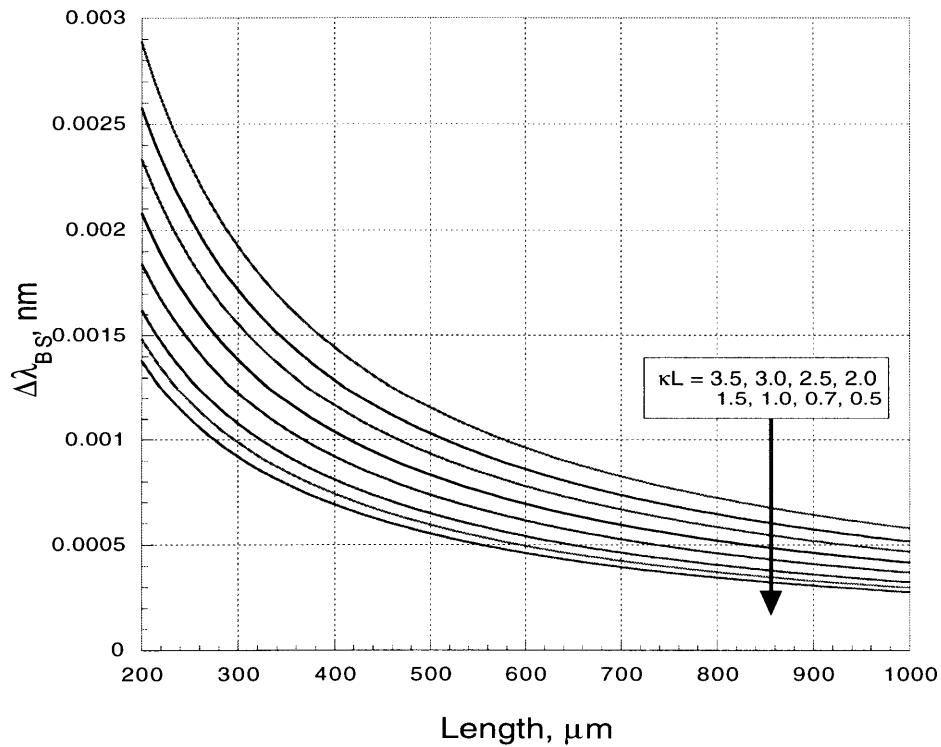


Figure 3.10: Width of bandstop versus length of device for different κL 's for AR/HR coated DFB laser similar to Fujitsu laser. Plot is for conditions: facet reflectivities 80% / 1%, $n_g=4.0$, $n_{eff}=3.285$, $I=(0.8)I_{th}$. Simulations performed using LaserMatrix.

3.4.2 Measurements for parameter extraction

The measurements were performed at Lincoln Labs in the high speed laser modulation lab. The first part of the measurement section involved utilizing an optical spectrum analyzer (OSA), an optical power meter, and an ILX laser diode controller (LDC 3900) connected to the packaged laser device to measure spectrum and power output from the laser device biased at DC. From the data obtained, it was possible to extract parameters.

The Fujitsu packaged laser diode contains as its central element a semiconductor laser device. The light output of the laser is focused by a spherical lens onto an optical fiber and then passes through an optical isolator to prevent optical feedback into the laser. The light exits the device through a fiber pigtail. A diode detector within the package measures the light output power of the laser.

The packaged laser devices were opened up and the temperature feedback circuitry was disconnected in order to allow external control of temperature and diode currents. The packaged laser diodes were connected to an ILX laser diode controller which supplied the current for the laser diode and the current for the TEC which maintained the lasers at a fixed temperature. In addition, the output of the detector diode and the thermistor were

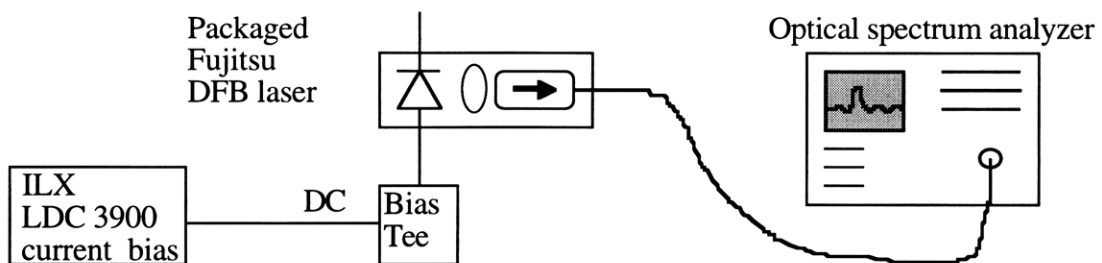


Figure 3.11: Experimental set up for measurement of optical spectra.

connected to the ILX laser diode controller so that the temperature and power output of the diode could be monitored through the ILX controller. The ILX bias current was connected to the Fujitsu laser via a Bias Tee (RF Circuits, model ZFBT-6GW) with a 6 GHz bandwidth. The optical spectrum analysis was performed on an Ando OSA scope, model 6320C. The data was captured onto a Power Mac using a LabVIEW program created at Lincoln Labs and at MIT.

The $\Delta\lambda_{BS}$ was measured to be 1.02 nm, and the $\Delta\lambda_{FP}$ was measured to be 0.71 nm. These measurements were taken from Figure 3.12 at $I=10.0$ mA, which corresponds to 80% of the threshold bias current. The extracted parameters were found to be $L=298\mu\text{m}$, and $\kappa L\approx 0.73$, assuming an index of refraction of $n_g=4$, which is a standard value for InGaAsP devices. These parameters along with other extracted parameters in the simulations presented in chapter 2.

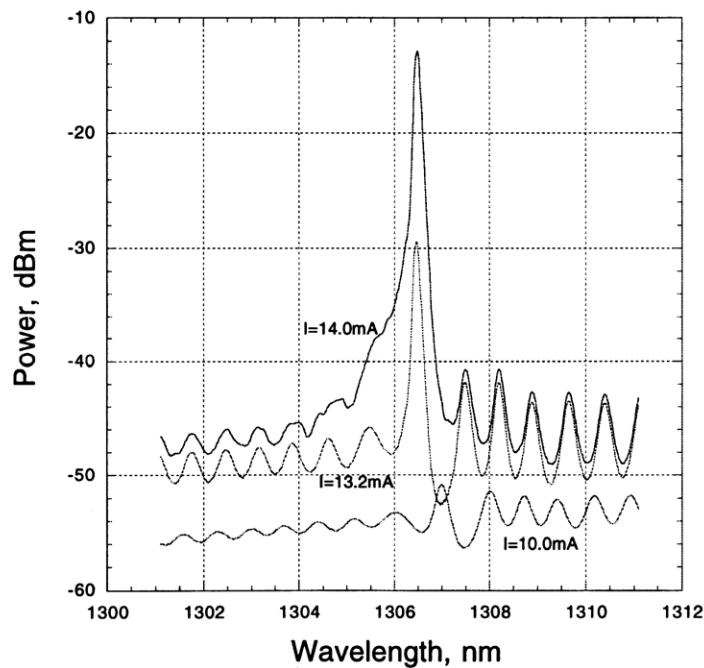


Figure 3.12: Optical spectrum for Fujitsu DFB laser, measured at three values: below threshold (10.0 mA), at threshold (13.2 mA), and above threshold (14.0 mA).

3.5 Conclusion

In this chapter, we presented the coupled mode theory for understanding a DFB structure. Based on coupled mode theory, we arrived at the conclusion that a κL value of 1.64 for an AR/AR coated DFB laser or a κL value of 0.8 for an AR/HR coated DFB laser would provide the most uniform photon density distribution and hence minimize the effect of spatial hole burning. We discussed the importance of spatial hole burning for DFB lasers and found that it can lead to a decreased dynamic side mode suppression ratio and increased nonlinearities leading to increased distortion. Under certain circumstances, however, we also found that it could aid in mode selection and actually decrease the intermodulation distortion by cancelling with the gain compression or with the relaxation oscillation effect. Under such conditions, it is still desirable to achieve a uniform distribution near threshold, although far above threshold the uniformity will decrease and spatial hole burning will increase. Finally, we explained a simple algorithm for extracting the length and coupling coefficient from the spontaneous emission spectrum, and we presented the extracted parameters. These parameters were used in simulations presented in chapter 2.

Chapter 4

HIGH SPEED MEASUREMENTS

In Chapter 2, we discussed the steady state, modulation, distortion, and noise characteristics for Fabry-Perot lasers. Many of these results were applicable to DFB lasers as well. We extracted several key parameters from RIN measurements and LI curves, and we presented simulations of distortion. In Chapter 3, we gave a brief overview of the coupled wave theory necessary to understand DFB laser devices. We also described the measurements that were carried out for the extraction of device parameters from the spontaneous emission spectrum. These parameters were also used in the simulations of Chapter 2.

In this chapter, we discuss measurements of laser dynamic characteristics. We describe the setup, procedure, and results of the high speed measurements. We are interested in determining the effects of spatial hole burning and the cancellation of gain compression. Our measurements indicate that there may be a cancellation effect between spatial hole burning and gain compression, and that spatial hole burning may be contributing to the selection of the lasing mode.

4.1 Equipment and setup

The measurements were performed for a 1.3 μm high-linearity packaged Fujitsu DFB laser (model FLD130F3ACH-AL), which is made for CATV signal distribution.[37] The laser is designed to minimize second order intermodulation distortion.

The high speed measurements were performed at Lincoln Labs on a test rack with a frequency range up to 1.28 GHz. The test rack contained two HP 8662A signal synthesizers, with a bandwidth of 1.28 GHz. The outputs of the two synthesizers were passed through isolation amplifiers which prevented signals from flowing backwards into the synthesizers. The signals were then mixed in a hybrid π mixer; the output of the mixer was fed into an attenuator whose attenuation settings were controlled by a HP 11713A Switch driver. This switch driver also contained the switches for the Device Under Test (DUT) switch, the Isolation Amplifier switch, and the Low Noise Amplifier (LNA) switch. The output of the attenuator could be switched either to the link or to a bypass via the DUT button (DUT "ON" corresponded to link connected). The signal would thus

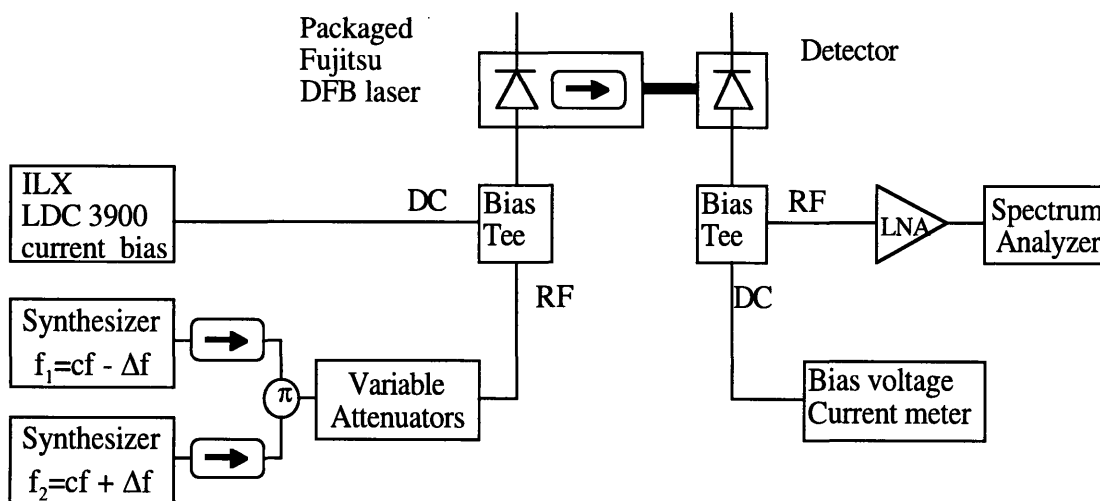


Figure 4.1: Test system block diagram.

flow either through the bypass pathway or through the link; after traversing either of these elements, the signal would flow into a Low Noise Amplifier (controlled by the switch driver) and then into the HP 8568B Spectrum analyzer which has a frequency range of 100 Hz to 1.5 GHz.

The laser diode was biased by an ILX Laser Diode Controller (LDC) model 3900. The bias current and RF signal were fed into a 6 GHz Bias-Tee (RF Circuits, model ZFBT-6GW). The output of the Bias-Tee was connected to the packaged Fujitsu DFB. The ILX LDC was also used to control the temperature of the packaged device via an internal peliter thermoelectric cooler. The output of the laser was focused through a lens into an optical isolator which prevented backreflections, and the output was coupled to a fiber. The fiber was spliced (0.02dB insertion loss) into another fiber leading to a detector. The total fiber length was less than two meters. The detector was a free space Epitax detector, mounted on a board with transmission line feeds.

4.2 High speed measurement procedure

4.2.1 Procedure

The exact procedure followed is given in Appendix A. In this section, I will only outline the basic measurement steps involved. There are two separate programs, both written by the author in LabVIEW. One program is used to measure the dynamic range versus the frequency (FrequencyScan.vi) and the other measures the dynamic range versus the current bias (CurrentScan.vi). In both cases, the programs have an outer loop which scans over a range of either frequencies or current biases. Both programs then call an inner

loop, AttenuationScan.vi, which measures the intermodulation products and fundamentals at a given frequency and current by scanning over a range of attenuations. By changing the attenuation, we are effectively changing the amplitude modulation of the signal, or equivalently the input power in the modulated signal. By scanning over a range of input powers, we can measure the size of the modulation signal as well as the size of the intermodulation products, and thus determine the spurious free dynamic range. The SFDR is calculated by subtracting the power in the noise floor from the power of the fundamental at the point where the intermodulation distortion crossed the noise floor. In making these calculations, we take the power in the fundamental, averaged between f_1 and f_2 , and the power in the intermod product, averaged between $2f_2-f_1$ and $2f_1-f_2$. Average power (in dB) of two signals, A and B (also in dB), is calculated according to:

$$\bar{P} = 10\log\left(\frac{1}{2}\left(10^{\left(\frac{A}{10}\right)} + 10^{\left(\frac{B}{10}\right)}\right)\right). \quad (4.1)$$

The dynamic range is measured in a 1 MHz bandwidth and is then converted to the standard units of dB Hz^{2/3}.

The program run time is approximately 45 minutes to one hour, depending upon the number of points desired. The program allowed the user to also measure second order intermodulation if desired.

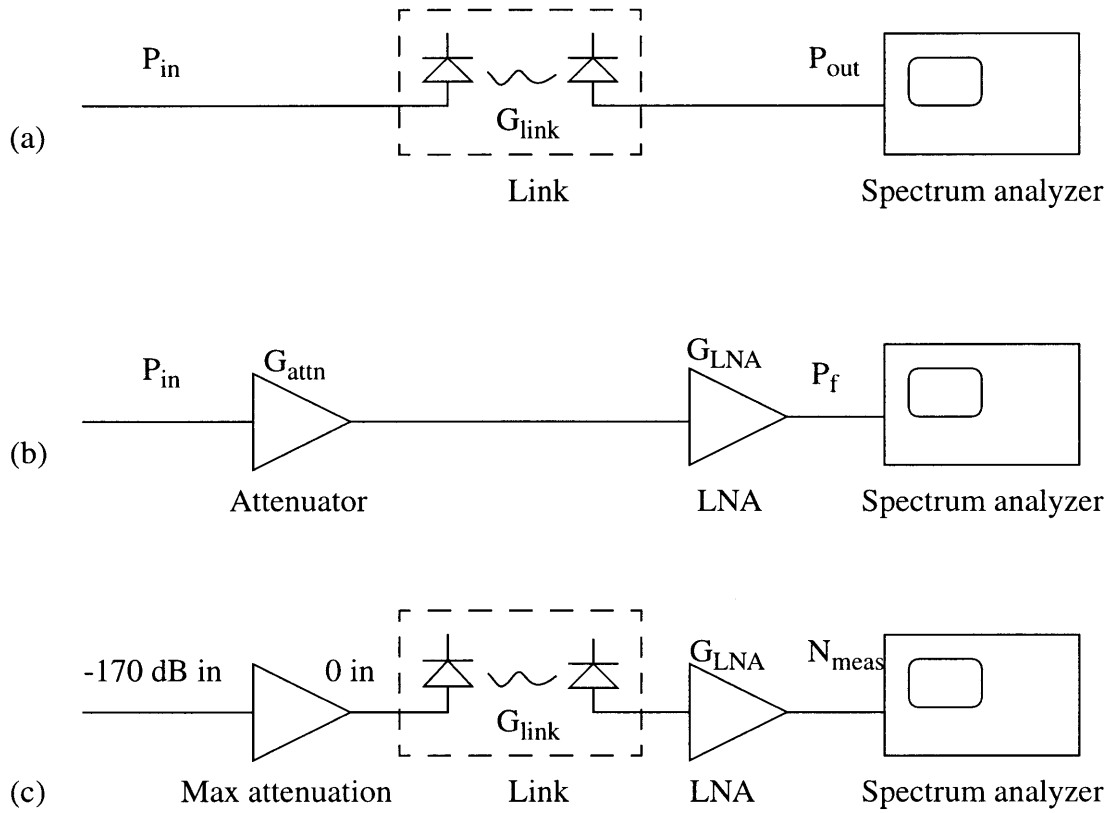


Figure 4.2: Measurement block diagrams for the three noise calibration steps.

4.2.2 Noise calibration

Before the actual dynamic range measurements are made, there is a routine that calculates the link gain, the gain of the low noise amplifier, the noise floor in the measurement bandwidth, the excess noise, and the noise figure of the link at each frequency or current bias setting. The basic steps in the measurement (shown in Figure 4.2) are as follows:

- a. Measure the power of the fundamental at the input, P_{in} . Measure the power of the fundamental at the link output, P_{out} . The link gain is $G_{link} = P_{in} - P_{out}$.
- b. Measure the output power of the fundamental, P_f , with the attenuators and low noise amplifier (LNA) on. The LNA gain is $G_{LNA} = P_f - P_{in} + G_{Attn}$.
- c. Measure the noise in the link with no input power, N_{meas} . The measured noise (N_{meas}) is obtained using the noise marker on the spectrum analyzer, which automatically takes into account the resolution bandwidth and a 1.7 dB correction factor.[Ref]

Other noise calibration figures can now be determined. The excess noise is given by:

$$N_{ex} = N_{meas} - G_{LNA} + N_T \quad (4.2)$$

The thermal noise (N_T) at room temperature sets the measurement noise floor at a 1 Hz measurement bandwidth: $N_T = 10\log(k_B T)$, where k_B is Boltzmann's constant, 1.38×10^{-23} J/K. For room temperature, $T=300$ K, the thermal noise is $N_T=174$ dBm. The noise figure is calculated by the formula

$$F = (N_{meas} - G_{LNA} + N_T) - G_{link} = N_{ex} - G_{link} \quad (4.3)$$

The noise floor in the measured bandwidth, B , is calculated according to:

$$N_B = N_{meas} - G_{LNA} + 10 \log(B) \quad (4.4)$$

This last figure, N_B , is the value that is used in calculating the SFDR.

4.2.3 Equipment Calibration

Calibration of the equipment had to be done on a regular basis. Calibration of the program was also necessary. The spectrum analyzer has an internal calibration routine that was run usually at the start of each day.

Some of the measurements were performed at frequencies slightly off from a round number to avoid possible resonances in the test rack that appeared to be occurring. For example, it was noticed that at multiples of 100MHz, there was some type of small resonance occurring within the test rack, so 102 MHz was chosen instead.

We measured the spurious free dynamic range of the electronics in the test rack and found it to be 132 dB Hz^{2/3}. Although a laser dynamic range higher than 127 dB Hz^{2/3} has not yet been reported, this system dynamic range indicates that further improvement of lasers would also require wider dynamic range test equipment. This also has the implication that if lasers were produced with dynamic ranges exceeding 132 dB Hz^{2/3}, the link performance would be limited by electronics at either end rather than by the laser.

4.2.4 Comparison of hand measurements with program measurements.

The program measurements were compared with hand measurements. Figure 4.3 shows a comparison of SFDR done by hand and SFDR done by the program. The measurements agree very nicely.

The program measurements were also compared with measurements done by another program written for use at Lincoln Labs. The measurements done by the LabVIEW computer program were 2 to 4 dB Hz^{2/3} above the measurements made by the other program. However, the other program did not actually measure the crossing of the third order inter-

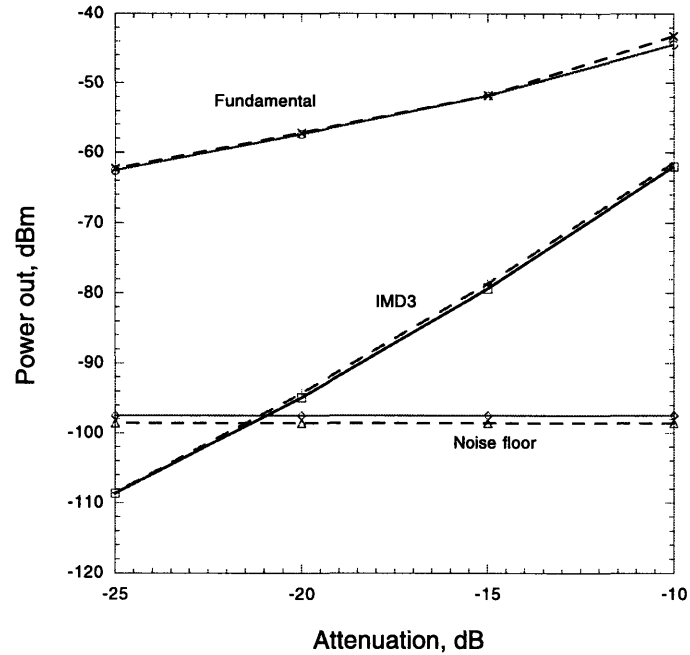


Figure 4.3: Comparison of program measurements (solid lines) and hand measurements (dashed lines).

mod with the noise floor - it measured the IMD3 above the crossing and extrapolated down, assuming a slope of 3. We discovered that this assumption was not always correct. Based on the discussion in section 2.5, we know that a slope of 3 is consistent with the case where there is no gain compression or other nonlinearities present. When these nonlinearities are present, the actual slope will vary slightly from 3. For the IMD3 shown in Figure 4.3, we measured a slope of 3.11.

4.3 Experimental data

Two types of measurements were performed: dynamic range versus frequency and dynamic range versus current bias. Both sets of measurements were performed on the same test rack described in previous sections. The data was taken by two different versions of the same LabVIEW code. The underlying measurement procedure for the dynamic range was the same, only the top layer differed in whether it scanned over frequency or current.

4.3.1 Dynamic range versus current bias

Figures 4.4 and 4.5 show the results of measuring the SFDR, noise figure and IMD3 at 24°C, 100 MHz modulation frequency. The input signals are both 0 dBm, or 1mW. The threshold at 24°C is 13.2 mA. The measurement intervals were 3mA, and they were limited only by the time available to take a complete set of data. The SFDR peaks near 35mA, while the noise figure dips to a minimum at approximately 24mA. The noise floor in the measurement bandwidth has a similar shape to the noise figure. The intermodulation distortion, which is shown for two different attenuation settings, show a minimum in the same area as the peak in the SFDR. Increasing attenuation corresponds to decreasing modulation depth. The peak in the SFDR thus occurs when the attenuation is 5 dB. These two figures indicate that the peak in the SFDR does not occur due to the minimum in the noise floor, but rather due to the minimum in the attenuation.

The measurements of dynamic range versus current for three different temperatures are shown in Figure 4.6(a)-(d). The center frequency is constant in each plot. Figure 4.7 shows the same data, but this time the temperature is constant in each plot. The data is

taken for different temperatures and shows an interesting effect. For a given center frequency, there is an optimal bias point that changes with temperature. This temperature dependence is non-trivial as it also depends upon the center frequency. The optimal bias point at 450MHz, and 24°C is 35mA, but at 15°C the optimal point shifts to 33mA as seen in Figure 4.5.

If the distortion were constant versus bias, there would still be a peak in the SFDR vs. bias due to a minimum in the noise. As shown in Figure 4.4, the SFDR do not coincide, while the SFDR does coincide with the IMD3 measured with 5 dB attenuation. In this case we conclude that the peak in the SFDR is caused by the distortion.

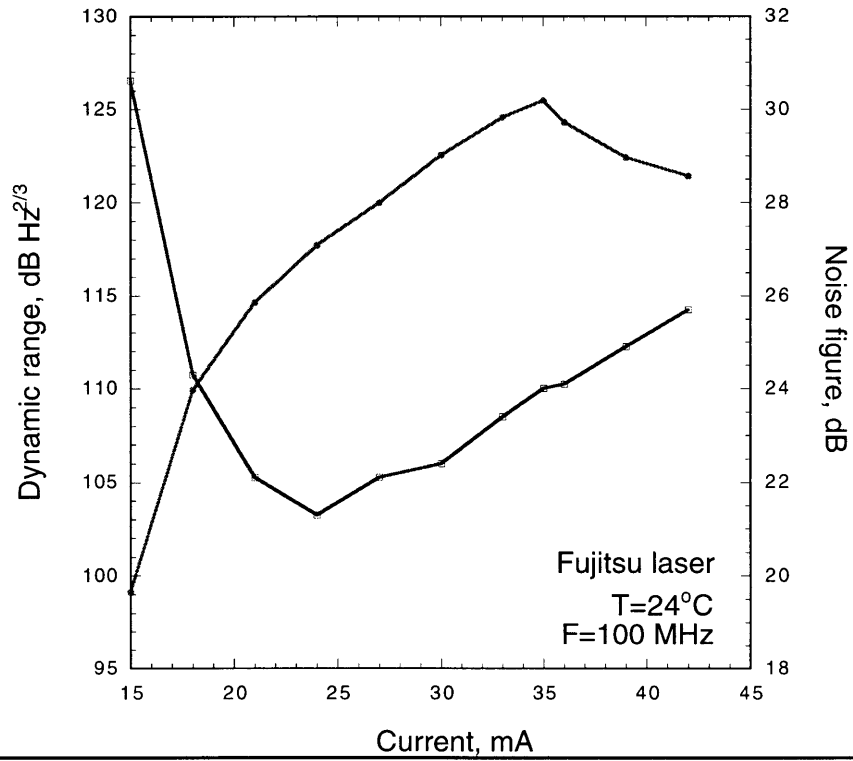


Figure 4.4: SFDR and noise figure versus current, Fujitsu laser, T=24°C, 100MHz.

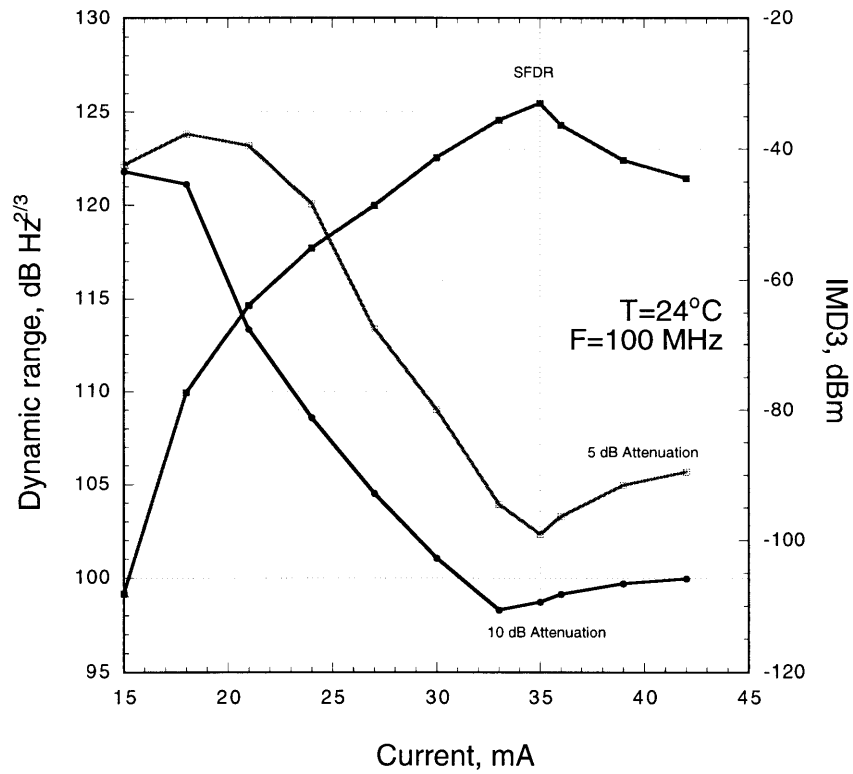


Figure 4.5: SFDR and intermods at two different attenuations, conditions as above.

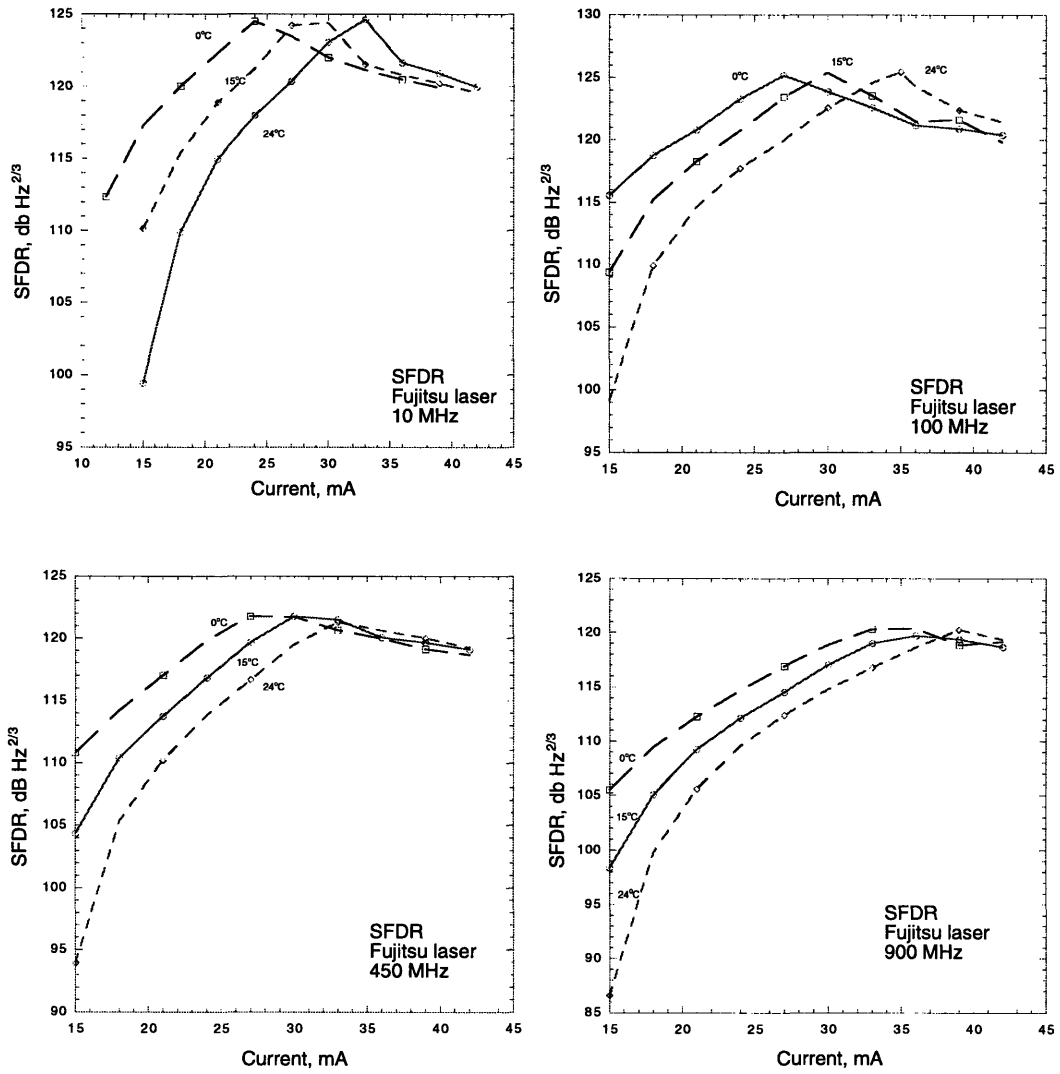


Figure 4.6: SFDR versus current, at three different temperatures, at (a) 10 MHz, (b) 100 MHz, (c) 450 MHz, and (d) 900 MHz.

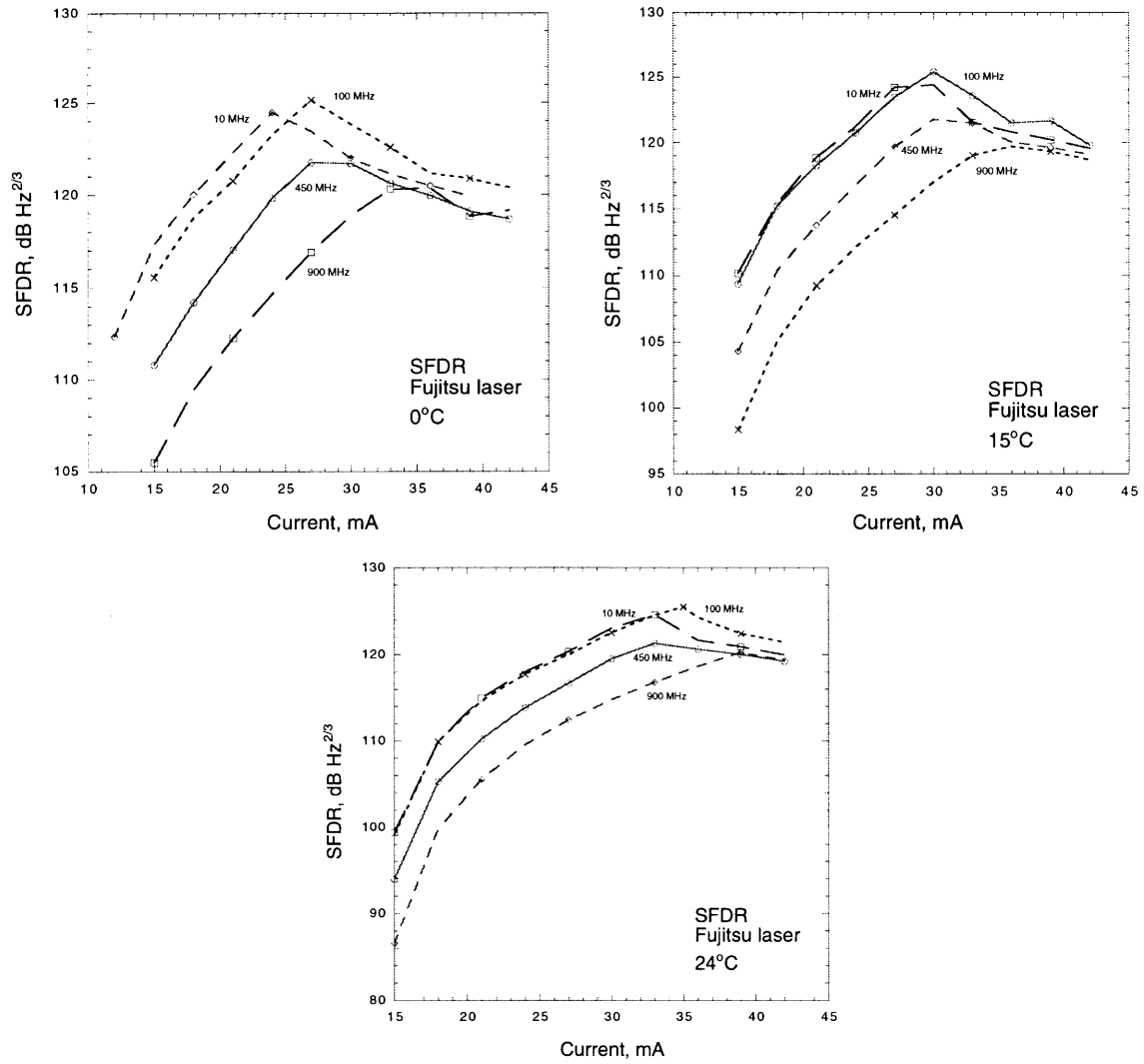


Figure 4.7: SFDR versus current, at four different frequencies, at (a) 0°C, (b) 15°C, and (c) 24°C.

4.3.2 Dynamic range versus frequency

Figure 4.2 shows the SFDR and noise figure for the Fujitsu laser versus frequency. The measurements were done at a current bias of 35mA, temperature $T=24^{\circ}\text{C}$, and at 100MHz frequency steps. The SFDR reaches its maximum value of 125.5 dB $\text{Hz}^{2/3}$ at a frequency of 100 MHz. The dynamic range versus frequency measurements shows a dip around 500MHz and 700-800MHz, which is believed to have been caused by electrical resonances in the system that we were unable to calibrate out. These resonances, however, should affect all the measurements in the same way, independent of temperature.

Figures 4.8 shows dynamic range versus frequency for three different temperatures. Figure 4.9 shows the noise figure versus frequency for the same three temperature measurements. Figure 4.10 shows the power in the fundamental signal versus frequency, and Figure 4.11 shows the third order intermodulation distortion versus frequency. The measurements are taken at a current bias of 35mA, with a channel spacing of 2MHz, and at a measurement bandwidth of 1MHz. These figures show many interesting effects. We see that the power in the fundamental is falling, whereas we expect that the power in the fundamental should stay constant or rise slightly, as shown in Figure 2.6. The power in the fundamental is relatively well behaved as temperature is changed, but this is not true for the noise figure, IMD3, or SFDR. At low frequencies, the high temperature measurement has a higher dynamic range than the lower temperature measurements, but the higher temperature measurement falls off faster. At higher frequencies, the lower temperature measurements have higher dynamic range than the high temperature measurements. In the mid range frequencies, the dynamic range, noise figure, and IMD3 cross over each other as temperatures are changing. The cause of this effect is not yet understood. In addition, we saw in the previous section that at a given frequency and temperature, there is an opti-

mal current bias point due to the cancellation of gain compression and spatial hole burning. As the temperature is lowered, this bias point shifts to lower currents.

These figures lead to two other interesting points. First of all, it appears that for high frequencies, larger dynamic ranges are achieved at lower temperatures. Secondly, there are certain frequencies or range of frequencies for which the laser is less affected by temperature variations at a given bias current. Between 300 and 700 MHz, the SFDR and the IMD3 for this laser are relatively temperature insensitive. Most DFB lasers that are sold today are packaged with a thermoelectric cooler and electronic circuitry to maintain a constant laser temperature. If, however, it became possible to design a laser that is temperature-insensitive in the desired frequency range, it may be possible to eliminate the thermoelectric cooler and reduce the cost of the DFB laser. Further investigation is necessary to confirm that these results are correct, and to understand what may be causing such a temperature switch and temperature-insensitive frequency regime.

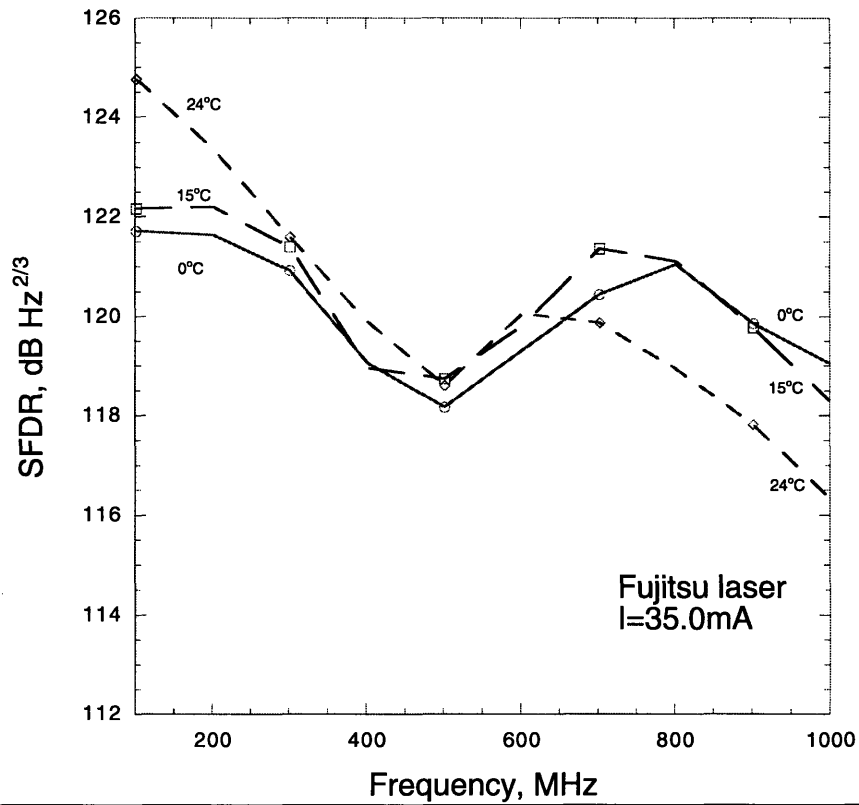


Figure 4.8: SFDR versus Frequency, for three different temperatures.

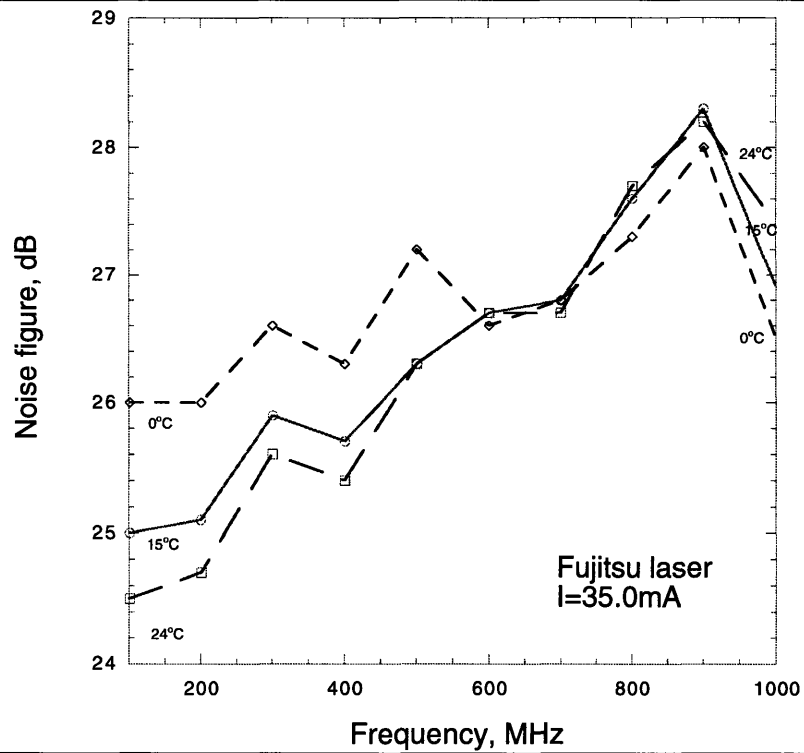


Figure 4.9: Noise figure versus frequency, for three different temperatures.

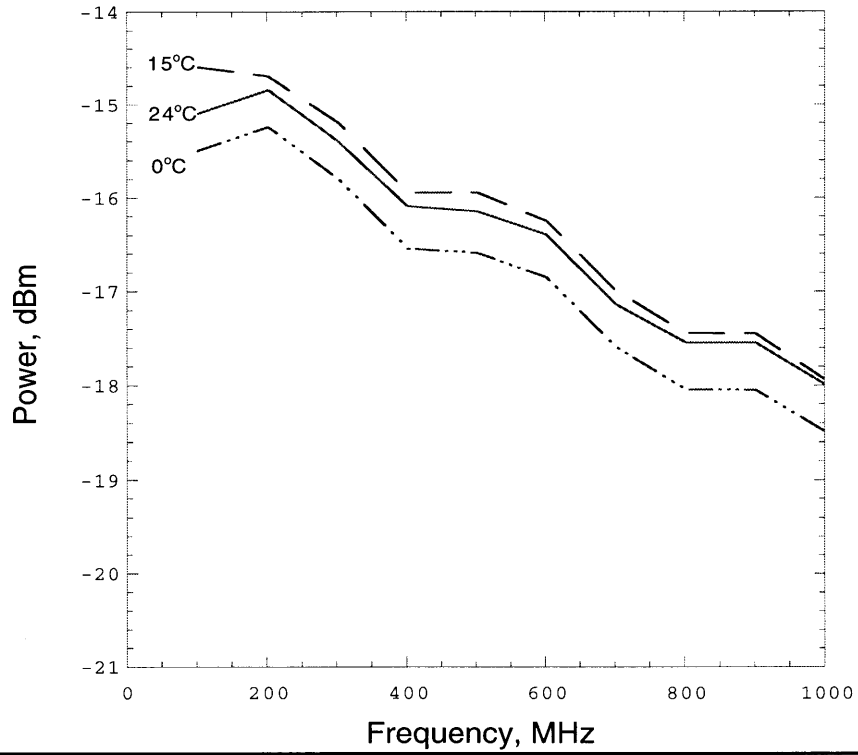


Figure 4.10: Fundamental versus frequency, for three different temperatures.

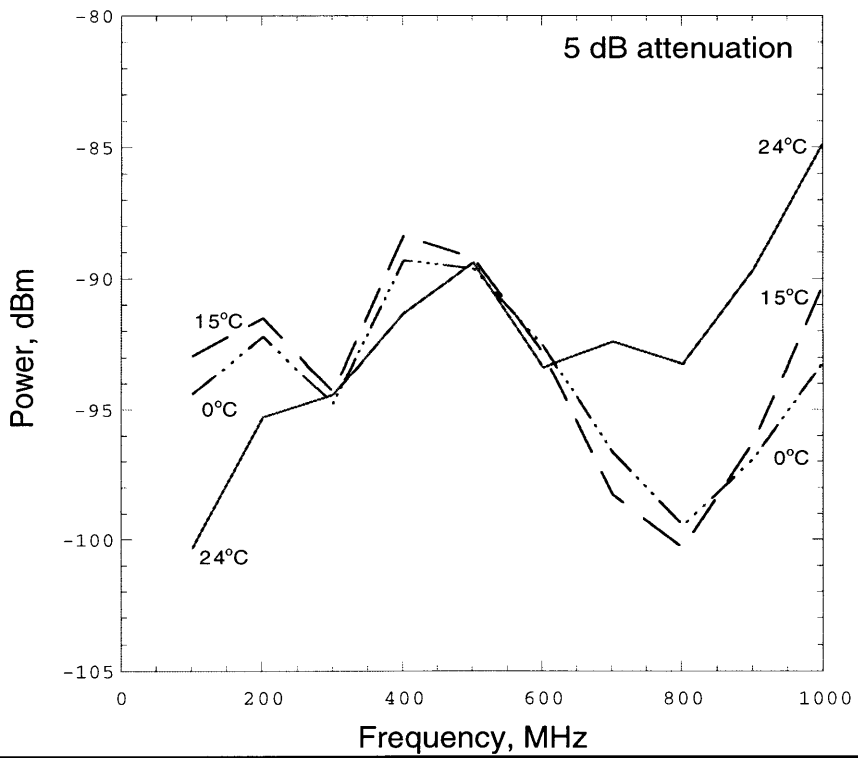


Figure 4.11: IMD3 at 5 dB attn. versus frequency, for three different temperatures.

4.4 Discussion and summary

4.4.1 Spatial hole burning related cancellation effects

In the present analysis, we find a reduction in the third order intermodulation distortion due to cancellation of spatial hole burning and gain compression. This leads to a peak in the SFDR. Figure 4.4 indicates that the peak in the SFDR is not related to the minimum in the noise floor. It had been suggested previously that the peak SFDR is obtained due to the minimum in the noise, but this is clearly not the case. Figure 4.5 indicates instead that the peak in the SFDR is instead obtained due to the minimum in the IMD3. At 35mA, the peak occurs where the third order intermodulation distortion crosses the noise floor, which occurs close to 5dB attenuation. In Figures 4.13-4.14, we plot the bias current at which SFDR is maximized minus the threshold current versus the temperature. The bias current minus threshold current corresponds to the optical power. At higher frequencies, we see that the maximum occurs at approximately a constant optical power, independent of temperature. This leads us to believe that the minimum in the intermodulation distortion is related to the spatial hole burning effect, which is dependent upon the optical power. We speculate that at that particular optical power, the spatial hole burning cancels the gain compression. In Chapter 2, we stated that the spatial hole burning effect is larger at bias currents directly above the threshold and decreases at higher output powers. The gain compression effect on the other hand is negligible right above threshold, but it continues to increase as the output power increases.

At lower frequencies, we see that the point of the maximum SFDR increases as the temperature increases, which leads us to believe that there are thermal effects that lead to an increase of the bias at which the cancellation between spatial hole burning and gain

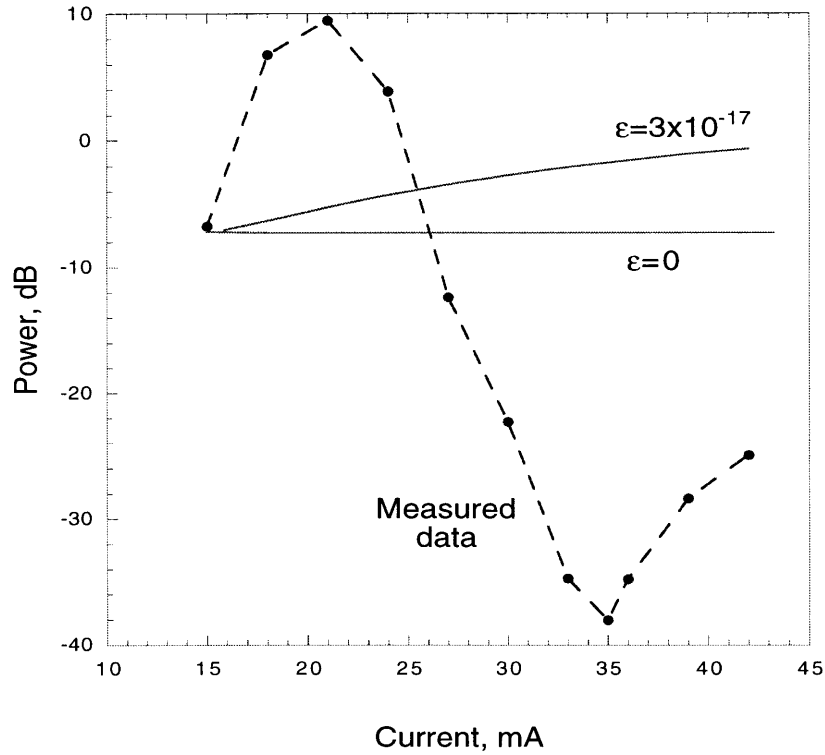


Figure 4.12: Measured (dashed) and calculated (solid) distortion relative to carrier, rescaled by modulation depth.

compression occurs. The associated thermal time constants appear to fall in between 100 MHz and 450 MHz.

Another type cancellation effect has been discussed previously in the literature. Okuda, et al. [26] report an internal distortion cancellation mechanism due to the cancellation of relaxation oscillation and longitudinal spatial hole burning. The relaxation oscillation response becomes important at frequencies close to the relaxation resonance frequency, but at low frequencies, such as 100 MHz, it is not an important effect. In our measurements, we find that for high frequencies, the maximum SFDR (and minimum distortion) occur at a constant optical output power. This leads us to conclude that the cause of the distortion minimum is a cancellation between gain compression and spatial hole burning, both of which are dependent upon the optical output power and hence upon the bias current above threshold. If this observation is correct, spatial hole burning may turn

out to be desirable to a certain extent as it can cancel the gain compression and improve the third order intermodulation distortion; however, more investigation is needed to support this conclusion.

Figure 4.12 shows measured and calculated distortion relative to carrier versus current bias. The measured data was taken at 100 MHz, 24°C, with a 1dBm constant input amplitude modulation. The data has been rescaled by dividing by the modulation depth cubed. As was discussed in section 2.5, the horizontal line for the case with no gain compression indicates that there is no nonlinearity other than the relaxation oscillation response, which is at a significantly higher frequency. The other calculated line ($\epsilon=3 \times 10^{-17}$) is rising and indicates that there is a nonlinearity caused by the gain compression. Since we assumed a small signal modulation in performing these simulations, they are not expected to be correct near threshold. At bias close to threshold, the laser may be forced below threshold if the modulation amplitude is large enough.

For the Fujitsu laser, the input resistance into the laser was unknown, so it was not possible to determine the exact current modulation amplitude. Nonetheless, the measured data was rescaled by a term of the form $(i/(I_{bias} - I_{th}))^3$, where $I_{th}=13.2$ mA was the threshold current for the laser at 24°C, I_{bias} was the horizontal axis, and i was adjusted arbitrarily. After rescaling, the data still has a peak and a minimum value. The peak in the distortion is most likely related to subthreshold effects. Regardless of the arbitrary scaling factor, the minimum value in the distortion indicates that there is a real effect present in the device, not an artifact of the modulation depth decreasing. This effect is most likely the result of a cancellation between the gain compression and the spatial hole burning. Because the data is taken far below the relaxation oscillation frequency, it is unlikely that the cancellation is occurring between the spatial hole burning and the relaxation oscillation as was described for a different device at higher frequencies by Okuda *et al.* [26]

4.4.2 Spatial hole burning related mode selection

In section 3.2.4, we discussed the possibility of spatial hole burning related mode selection. It is believed that for κL above 1.64, spatial hole burning is the dominant effect leading to mode selection, as described above. For κL below 1.64, this effect is less dominant. The Fujitsu DFB device is AR/HR coated; Figure 3.12 clearly indicates that the device lases at the short wavelength side. The reason for this is not understood yet. The effect of the refractive index change on the mode profile may be a factor in determining which mode reaches threshold first [6], but in this case we believe that the mode selection occurs due to the facet phase.

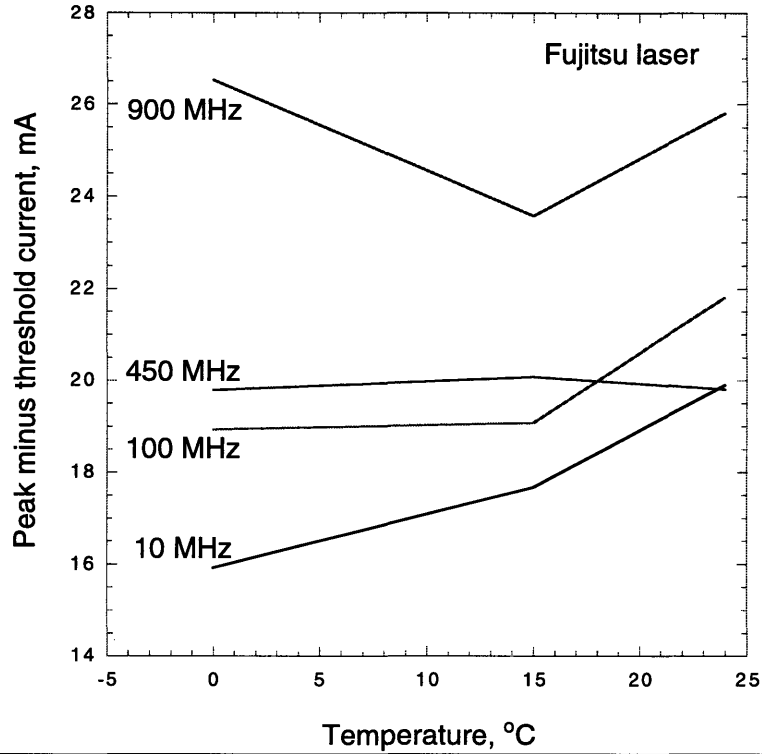


Figure 4.13: Plot of current that maximizes SFDR minus the threshold current vs temperature for four different frequencies.

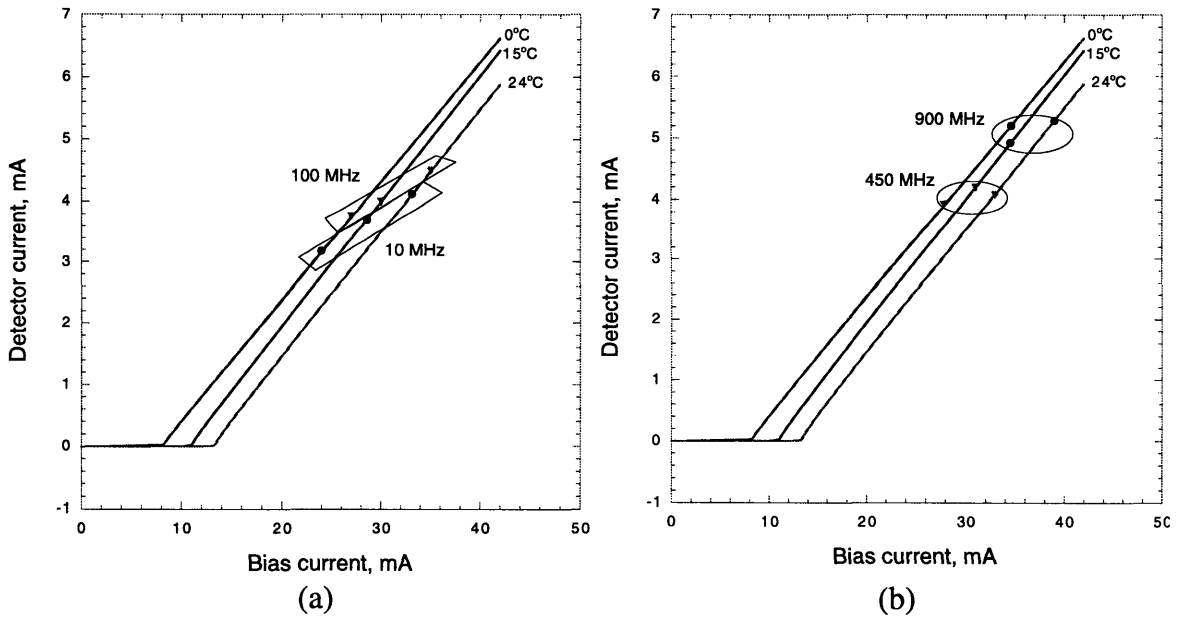


Figure 4.14: Current at which SFDR is maximized, plotted on LI curves. (a) At lower temperatures, heating effects are present. (b) At higher frequencies, these points are roughly constant as temperature is changed.

4.4.3 Temperature related effects

Steady state

In section 2.1.4, we found a characteristic temperature of 47°K for the Fujitsu DFB laser. This value, which is on the low side for InGaAsP / InP lasers, indicates that the threshold current for the laser is more sensitive to temperature changes, possibly due to Auger recombination and leakage currents. This may be because the DFB structure has an unstrained bulk active region.

Dynamic range

Figures 4.13 and 4.14 show that the optimal current bias for SFDR minus the threshold current versus the temperature has a frequency dependence. The bias current minus threshold current corresponds to the optical power. This leads us to believe that the minimum in the intermodulation distortion is related to the spatial hole burning effect. Such a conclusion is based on a limited set of data, however, and further investigation is required to support this conclusion. In addition, the temperature related effects seem to be stronger at lower frequencies than at higher frequencies.

Chapter 5

CONCLUSION

5.1 Summary of work

This work was motivated by the desire to explore linearity in DFB lasers for analog applications. In order to accomplish this task, our strategy was to measure steady state characteristics for a Fujitsu laser that has been shown to have low distortion, prepare simulations for dynamic characteristics based on a rate equation analysis and measure distortion and dynamic range for the laser. As is expected of research, our work has led to some answers and has raised even more questions to explore in the future. We now summarize our results.

We presented a summary of our extraction of structure parameters in Chapter 2, as well as a short algorithm for parameter extraction of DFB parameters in Chapter 3. These parameters were extracted from an AR/HR coated Fujitsu DFB laser which is optimized for second order intermodulation distortion in analog (primarily CATV) applications. This laser has a bulk active region, and is designed with a coupling coefficient $\kappa L=0.7$ in order to minimize the effects of spatial hole burning. Because of the asymmetric design of

the facet coatings, most of the light comes out of the AR coated side, while the HR coated side effectively acts to double the length that each photon has to travel before escaping.

Based on the extracted parameters, we simulated the device using a non-spatially dependent rate equation analysis with gain compression. We simulated steady state and dynamic characteristics of the device. We also presented simulations of distortion to indicate what we would expect if the only nonlinearities present were gain compression and the intrinsic nonlinearity of the laser.

In order to take our data, we developed data acquisition software for measuring SFDR versus either frequency or bias current. The program measures the power in the fundamental, in the intermodulation products, and in the noise floor in order to determine the SFDR. With this software, the user has a great deal of flexibility in terms of what attenuation, frequency, bias current ranges over which to scan, as well as many of the other program variables. The program allows for control over a test rack that includes an ILX controller, two frequency synthesizers, an attenuation switch box, and a spectrum analyzer. The software was written in LabVIEW, and an outline of the software is provided in Appendix B.

From our data, we observed that there is a bias current at which the SFDR actually peaks. We stipulated that the reason for this is that there is a cancellation between gain compression and spatial hole burning that occurs, leading to a local minimum in the third order intermodulation distortion. The minimum was not caused by gain compression acting alone or by the relaxation oscillation nonlinearity of the laser, as seen from comparisons with the simulations performed in Chapter 2. We concluded that this cancellation occurs because the spatial hole burning is believed to lead to a superlinear LI curve at low currents above threshold in this particular case. The gain compression, on the other hand, always leads to a sublinear LI curve, starting at higher currents. There is a point in

between the low and high current regimes where the two effects just cancel each other out, leading to a minimum in the distortion. **This indicates that having a certain amount of spatial hole burning present may actually improve the SFDR.** Furthermore, by adjusting the relative amounts of gain compression and spatial hole burning, it may be possible to shift the point where the peak occurs so that it coincides with the minimum in the noise floor, leading to an even greater improvement in the SFDR. As was reported by Cutrer et al, even a 4 dB increase in the SFDR could potentially double the number of calls that can be handled by a laser transmitter while ensuring a certain call blocking probability.[12]

Finally, we also measured temperature dependencies in the SFDR at different frequencies and we found that at low frequencies the output power that corresponds to the maximum SFDR is temperature dependent, whereas at higher frequencies the output power that corresponds to the maximum SFDR is temperature independent. We stipulated that the cause of these effects may be related to thermal lifetimes on the order of 300 MHz. At the higher frequencies, the fact that the maximum SFDR occurred at the bias output power regardless of temperature lent support to our stipulation that the peak in the SFDR and hence the minimum in the intermodulation distortion are related to spatial hole burning, which is dependent upon the output power.

5.2 Maximizing Dynamic Range (SFDR)

As discussed in section 2.3.3, there are three quantities that determine the SFDR: the power in the fundamental, the noise floor, and the power in the intermodulation distortion term. Increasing the fundamental by 1 dB will have the effect of increasing the SFDR also by 1 dB. Thus, achieving high output powers and high slope efficiencies is critical to ensuring a large SFDR.

Decreasing the IMD3 by 1 dB will cause the SFDR to increase by only 1/3 dB, because of the slope of the IMD3. In the chapter 2, we simulated distortion and we explored how the distortion changes as bias and frequency are changed. In chapter 4, we then reported our observations of a peak SFDR in the Fujitsu laser caused by a minimum in the third order intermodulation distortion. This minimum is believed to be caused by a cancellation effect between the gain compression and the spatial hole burning. Exploiting

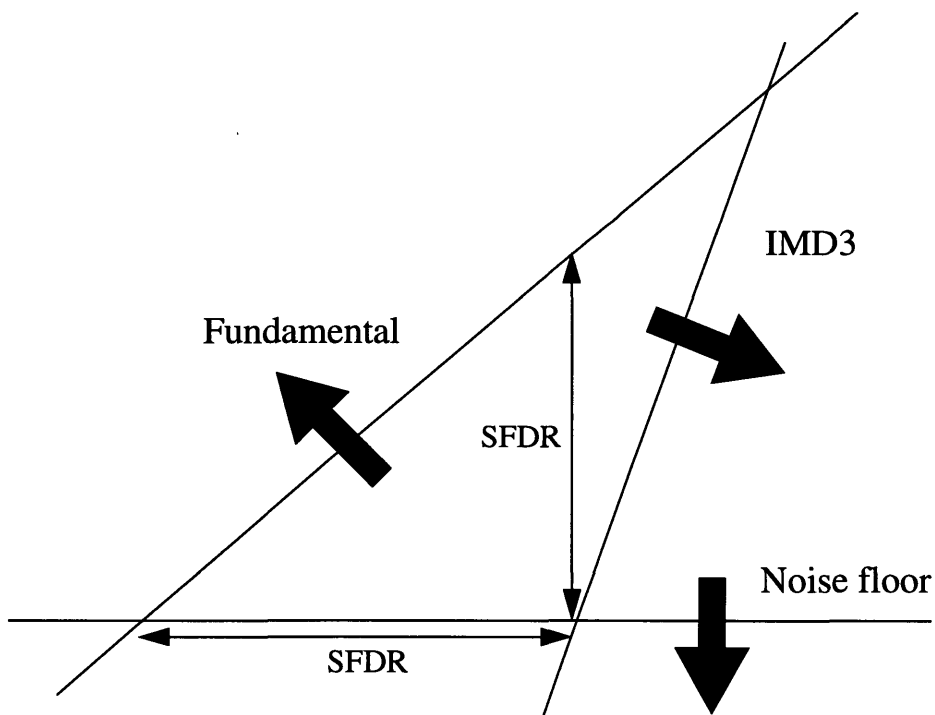


Figure 5.1: Three possible ways to improve SFDR.

this effect by properly biasing and temperature controlling the laser device provides a way to increase the SFDR.

There is also another point at which we could improve the SFDR. We showed in Chapter 4 that the peak in the SFDR does not occur at the same bias current as the minimum in the noise. If, however, we were able to adjust the spatial hole burning and gain compression effects in such a way as to shift the peak SFDR to lower bias currents, we may be able to line up the two effects and take advantage of a minimum distortion and minimum noise floor. The noise floor is determined by the application bandwidth, the measured noise and the amplifier gain in the system, as seen in equation 2.33. The application bandwidth is determined by system requirements, and the amplifier gain is determined by the system itself. The measured noise falls off above the threshold, and then starts to rise again once it reaches the shot noise limit. The minimum occurs at the intersection of these two effects. Decreasing the noise floor by 1 dB will have the effect of increasing the SFDR by 2/3 dB because of the slope of the IMD3. Thus, taking advantage of this effect could yield an important improvement in the SFDR. As mentioned before, Cutrer *et al.* reported that even a 4 dB increase in the SFDR could potentially double the number of calls that can be handled by a laser transmitter while ensuring a certain call blocking probability.[12]

5.3 Temperature insensitivity

Our measurements of dynamic range versus frequency for three different temperatures showed that between 300 and 700 MHz the third order intermodulation distortion and spurious free dynamic range of the Fujitsu DFB laser are relatively insensitive to temperature changes from 0 to 24 °C. While further investigations are necessary to confirm these results and understand the cause of this temperature insensitivity, these results already indicate that over this range of frequencies the Fujitsu DFB laser can be used without a thermoelectric cooler while still obtaining a temperature insensitive high-dynamic range. **By packaging the device without a thermoelectric cooler, a substantial cost savings could be realized.**

5.4 Future work

As the demand for communications continues to grow, the need for high linearity lasers with high dynamic ranges will increase. Proposals have already been made for lasers with dynamic ranges far exceeding those of today's devices. In the course of our measurements, we have found that our test equipment has a spurious free maximum dynamic range of $132 \text{ dB Hz}^{2/3}$, which is not far above the maximum SFDR that we measured for the Fujitsu laser ($125.4 \text{ dB Hz}^{2/3}$). Nonetheless, there is still room to improve lasers before we begin to be limited by electronics. To further explore high linearity DFB lasers for analog applications, the following avenues of investigation are suggested:

- Adjust the gain compression to cancel out the spatial hole burning at lower bias currents. This could allow the maximum in the dynamic range to coincide with the mini-

mum in the noise figure, thus increasing the SFDR.

- Incorporate a simple lumped element model of spatial hole burning for the case of a DFB laser with nearly uniform photon distribution. As was discussed in section 3.2.3, for the case of a nearly uniform photon distribution, the rate equation analysis presented in Chapter 2 is highly accurate, at least near threshold. Therefore, it may be possible to determine a relationship determining the extent of spatial hole burning in terms of the photon distribution, and incorporate this effect as a single lumped element into the rate equations. Such a lump element model for the spatial hole burning would greatly simplify analysis for DFB lasers.
- Analyze the frequency dependence of the lasers out to higher frequencies. Our measurements showed that around 1 GHz, low temperatures lead to higher dynamic ranges. Further investigation is necessary to verify that this remains true out to higher frequencies.
- Examine the result that the temperature dependence changes while going from low frequencies to high frequencies (see Figure 4.8). We found that there was a range of frequencies over which the SFDR of the Fujitsu laser was temperature insensitive. Further investigation is necessary to determine the cause of this effect and to verify that this effect occurs over a wider range of temperatures. If this effect is understood, it may be possible to design lasers with a temperature insensitive range for the desired range of operating frequencies, thus making extra cooling elements unnecessary and reducing packaging costs.

- 1b. Measure power of fundamentals at link output (Pout):
- | | |
|----------------------------|---------|
| Device Under Test (DUT) | ON |
| Low Noise Amplifier (LNA) | OFF |
| Attenuators | Minimum |
| Synthesizers set as above. | |

$$\text{Link gain} = \text{Pout} - \text{Pin}$$

2. Characterize Low Noise Amplifier (LNA) gain:
- | | |
|----------------------------|------|
| Device Under Test (DUT) | OFF |
| Low Noise Amplifier (LNA) | ON |
| Attenuators | 50dB |
| Synthesizers set as above. | |

Measure output power at input frequency (Pf1).

$$\text{LNA gain} = \text{Pf1} - \text{Pin} + 50\text{dB}.$$

3. Characterize link noise figure (NF):
- | | |
|---------------------------|----------|
| Device Under Test (DUT) | ON |
| Low Noise Amplifier (LNA) | ON |
| Attenuators | 70dB |
| Synthesizers | Both OFF |
| Noise marker | ON (KSM) |

Measure output noise power at input frequency (MN).

$$N_{\text{ex}} = \text{MN} - \text{LNA gain} + 174 \text{ dB}$$

$$F = \text{Excess noise} - \text{link gain}$$

$$N_{\text{B}} = N_{\text{meas}} - \text{LNA gain} + 10 \log (\text{MBW})$$

Measured BW is the bandwidth at which the system is operating. The 174dB term arises because of thermal noise at room temperature (T=298.15K):

$$173.38 = 10 \log (k_{\text{B}}T)$$

where k_{B} is Boltzmann's constant, $8.43\text{e}+14$.

Shut video averaging off (KSH) and noise marker off (KSL) when done.

A.2 Measurement routine

The main measurement routine is run by a LabVIEW program called **Frequency-Scan.vi**. This program has a loop which runs from a minimum frequency to a maximum frequency in steps defined by the user. During this loop, **FrequencyScan.vi** makes a call to a sub-vi **AttenuationScan.vi**, which scans the intermodulation products and fundamentals with attenuations ranging from a minimum to a maximum attenuation in steps also defined by the user. By

1. Determine frequency to use.

Number of steps to take in loop = Integer [$(F_{\max} - F_{\min})/F_{\text{step}}$] + 1

$$F_i = i * F_{\text{step}} + F_{\min}$$

2. Call **AttenuationScan.vi**:

- a. Make the following settings to the synthesizer.

Resolution Bandwidth	300 Hz
Video Bandwidth	100 Hz
Frequency Span	500 Hz
Device Under Test (DUT)	ON

- b. Scan over attenuation, from Attn_{\min} to Attn_{\max} in steps of $\text{Attn}_{\text{step}}$. At each attenuation, first run calibration routine **calibrate.vi** (see A.1). Next run **intermod.vi**. It does the following things:

- Set top and bottom synthesizers to appropriate input power levels and frequencies.

- Measure power at the following frequencies with settings:

Frequencies	Video Avg.	Ref. Level
F1, F2	0	0 dBm
F1+F2, F2-F1 (*)	5	-50 dBm
2F2-F1, 2F1-F2	5	-50 dBm

(*) Second order intermods are only measured if IMD2 button is switched on.

- Determine average power of fundamentals (FUND), second order intermods (IMD2) and third order intermods (IMD3). Average power, \bar{P} , of *A* and *B* (all in dB) is computed using the formula:

$$\bar{P} = 10\log\left(\frac{1}{2}\left(10^{\left(\frac{A}{10}\right)} + 10^{\left(\frac{B}{10}\right)}\right)\right).$$

- Shut video averaging off.
- c. Calculate dynamic range at desired measurement bandwidth.
 - d. Attenuation on test rack reset to minimum, DUT OFF.
 - e. Plot and save attenuation scan data (usually off).
3. Plot and save data.
- Save all data sets:
- F1, F2
 - F1+F2, F2-F1
 - F1+F2ISR, F2-F1ISR
 - 2F1-F2, 2F2-F1
 - 2F1-F2ISR, 2F2-F1ISR
 - AVEIMD2, AVEFUND,
 - AVEIMD3, NOISEFLOOR
- Save Dynamic Range vs. Frequency (FRvsDR) plot.
- Save Spurious Free Dynamic Range (SFDR) plot.

References

- [1] G.P. Agrawal. *Fiber-optic Communication Systems*. Wiley, New York, 1992.
- [2] G.P. Agrawal and N. K. Dutta. *Long-Wavelength Semiconductor Lasers*. Van Nostrand Reinhold, New York. 1986.
- [3] I. Andonovic and D. Uttamchandani. *Principles of Modern Optical Systems*. Artech House, Norwood, MA. 1989.
- [4] N.W. Ashcroft and N.D. Mermin. *Solid State Physics*. Saunders College Publishing, New York, 1976.
- [5] N. Ayrandijan. "Simple Computation of Spurious-Free Dynamic Range," RF Design, p. 65, January 1987.
- [6] J. Chen. "Linearity and Third Order Intermodulation Distortion in DFB Semiconductor Lasers." To be published.
- [7] J. Chen, R. Dalal, R. Ram, R. Helkey. "Dynamic range of DFB semiconductor lasers." Submission to Conference on Lasers and Electro-Optics (CLEO), 1998.
- [8] J. Chen, R. Ram, R. Helkey. "Spatial Hole Burning Effect on the linearity and Intermodulation Distortion of DFB Lasers." Unpublished. 1997.
- [9] L. A. Coldren, and S. W. Corzine. *Diode Lasers and Photonic Integrated Circuits*. John Wiley and Sons Inc. New York, 1995.
- [10] C. Cox III. Presentation and personal communication.
- [11] C. Cox III. "Optical Transmitters," Chapter 57 in *The Electronics Handbook*, Jerry C. Whitaker, Editor-in-Chief. Technical Press, Inc. Oregon. 1996.

- [12] D. Cutrer, J. B. Georges, T. H. Le, K. Y. Lau. "Dynamic Range Requirements for Optical Transmitters in Fiber-Fed Microcellular Networks," IEEE Photonics Technology Letters, Vol. 7, No. 5, May 1995.
- [13] R. Dalal, R.J. Ram, R. Helkey, H. Roussel, K.D. Choquette. "Analog transmission using vertical-cavity lasers." Submission to Conference on Lasers and Electro-Optics (CLEO), 1998.
- [14] T.E. Darcie, R.S. Tucker, G.J. Sullivan. "Intermodulation and Harmonic Distortion in InGaAsP lasers," Electronics Letters, Vol. 21, No. 16, August 1, 1985.
- [15] J.C. Fan, C.L. Lu, L.G. Kazovsky. "Dynamic Range Requirements for Microcellular Personal Communications Systems Using Analog Fiber-Optic Links," IEEE Transactions on Microwave Theory and Techniques, Vol. 45, No. 8. August 1997. pp. 1390-1397.
- [16] H. Haisch, U. Cebulla, E. Zielinski, J. Bouayad-Amine, M. Klenk, G. Laube, H.P. Mayer, R. Weinmann, P. Speier. "Low-Chirp Highly Linear 1.55 μm Strained-Layer MQW DFB Lasers for Optical Analog TV Distribution Systems," IEEE Journal of Quantum Electronics, Vol. 29, No. 6, June 1993.
- [17] H. Haus. *Waves and Fields in Optoelectronics*. Prentice Hall, Inc. Englewood Cliffs, New Jersey. 1984.
- [18] J. Helms. "Intermodulation and Harmonic Distortions of Laser Diodes and Optical Feedback," IEEE Journal of Lightwave Technology, Vol. 9, No. 11, Nov. 1991.
- [19] J. Helms. "Intermodulation Distortions of Broad-band Modulated Laser Diodes," IEEE Journal of Lightwave Technology, Vol. 10, No. 12, December 1992.
- [20] A.L. Holmes Jr. "1.55 Micron In-Plane Lasers Using Wafer Fused Cladding

- Layers.” Ph.D. Dissertation, University of California, Santa Barbara, June 1997.
- [21] P. Iannone, and T.E. Darcie. “Multichannel Intermodulation Distortion in High-Speed GaInAsP Lasers,” *Electronics Letters*, Vol. 23, No. 25, December 3, 1987.
- [22] H. Kogelnik and C.V. Shank. “Coupled-Wave Theory of Distributed Feedback Lasers,” *Journal of Applied Physics*, Vol. 43, No. 5, May 1972. pp. 2327-2335.
- [23] K.Y. Lau and A. Yariv. “Intermodulation Distortion in a Directly Modulated Semiconductor Injection Laser,” *Applied Physics Letters*, Vol. 45, No. 10, November 15, 1984.
- [24] J. Minch, S.L. Chuang, C.S. Chang, W. Fang, Y.K. Chen, T. Tanbun-Ek. “Theory and Experiment on the Amplified Spontaneous Emission from Distributed-Feedback Lasers,” *IEEE Journal of Quantum Electronics*, Vol. 33, No. 5, May 1997. pp. 815-823.
- [25] G. Morthier and P. Vankwikelberge. *Handbook of Distributed Feedback Lasers*. Artech House Inc. Boston, MA, 1997.
- [26] T. Okuda, Y. Muroya, H. Yamada, T. Torikai, T. Uji. “Internal distortion cancellation mechanism in DFB lasers owing to relaxation oscillation and longitudinal spatial hole burning,” *Electronics Letters*, Vol. 31, No. 23. Nov. 9, 1995.
- [27] T. Okuda, H. Yamada, T. Torikai, T. Uji. “DFB Laser Intermodulation Distortion Analysis Taking Longitudinal Electrical Field Distribution into Account,” *IEEE Photonics Technology Letters*, Vol. 6, No. 1, January 1994. pp. 27-30.
- [28] R. Olshansky, V. Lanzisera, P.M. Hill. “Subcarrier Multiplexed Lightwave Systems for Broad Band Distribution,” *Journal of Lightwave Technology*, Vol. 7, No. 9, September 1989.

- [29] J. Pawlan. "A tutorial on intermodulation distortion and non-linearity in RF systems." RF Design, February 1996.
- [30] M.R. Phillips, T.E. Darcie, E.J. Flynn. "Experimental Measure of Dynamic Spatial Hole Burning in DFB Lasers," IEEE Photonics Technology Letters, Vol. 4, No. 11, November 1992.
- [31] H. Roussel, R. Helkey, G. Betts, C. Cox III. "Effect of Optical Feedback on High-Dynamic Range Fabry-Perot Laser Optical Links," IEEE Photonics Technology Letters, Vol. 9, No. 1, January, 1997.
- [32] H.M. Salgado, J.M. Ferreira, J.J. O'Reilly. "Extraction of Semiconductor Intrinsic Laser Parameters by Intermodulation Distortion Analysis," IEEE Photonics Technology Letters, Vol. 9, No. 10, October 1997. pp. 1331-1333.
- [33] R. Schatz, E. Berglind, L. Gillner. "Parameter Extraction from DFB Lasers by Means of a Simple Expression for the Spontaneous Emission Spectra," IEEE Photonics Technology Letters, Vol. 6, No. 10, October 1994. pp. 1182-1184.
- [34] A. Siegman. *Lasers*. University Science Books, 1986.
- [35] H. Watanabe, T. Aoyagi, A. Takemoto, T. Takiguchi, E. Omura. "1.3- μ m Strained MQW-DFB Lasers with Extremely Low Intermodulation Distortion for High-Speed Analog Transmission," IEEE Journal of Quantum Elec., Vol. 32, No. 6, June 1996.
- [36] H. Watanabe, T. Aoyagi, K. Shibata, T. Takiguchi, S. Kakimoto, H. Higuchi. "1.3- μ m Uncooled DFB Lasers with Low Distortion for CATV Application," IEEE Journal of Selected Topics in Quantum Electronics, Vol. 3, No. 2, April 1997.
- [37] H. Yonetani, K. Kamite, I. Ushijima. "DFB Laser Diode and Module for Analog Application," Fujitsu Scientific Technical Journal. Japan.